1.55 µm integrated modelocked semiconductor lasers

1.55 μm Integrated Modelocked Semiconductor Lasers

PROEFSCHRIFT

ter verkrijging van de graad van doctor aan de
Technische Universiteit Eindhoven, op gezag van de
Rector Magnificus, prof.dr.ir. C.J. van Duijn, voor een
commissie aangewezen door het College voor
Promoties in het openbaar te verdedigen
op maandag 2 april 2007 om 16.00 uur

door

Yohan Barbarin

geboren te Clermont-Ferrand, Frankrijk

Dit proefschrift is goedgekeurd door de promotoren:

prof.dr.ir. M.K. Smit
en
prof.dr. D. Lenstra

Copromotor:
dr. E.A.J.M. Bente

This research was supported by the Towards Freeband Communication Impulse program of the Dutch Ministry of Economic Affairs (STW), the NRC Photonics program and the COST 288 frame work.

Printed in The Netherlands.
Cover from a painting of M^{lle} Pauline Calmette

CIP-DATA LIBRARY TECHNISCHE UNIVERSITEIT EINDHOVEN

Barbarin, Yohan

1.55 μm integrated modelocked semiconductor lasers / by Yohan Barbarin. – Eindhoven : Technische Universiteit Eindhoven, 2007.
Proefschrift. – ISBN 978-90-386-2013-8
NUR 959
Trefw.: halfgeleiderlasers / geintegreerde optica / 3-5 verbindingen / optische telecommunicatie.
Subject headings: laser mode locking / integrated optics / III-V semiconductors / optical fibre communication.

à mes parents et grands-parents;

Contents

Chapter 1
Introduction

1.1 Introduction

A modelocked laser (MLL) is a much used laser source to obtain a periodic train of short light pulses. Different types of modelocked lasers with specific performance levels exist for various applications. Historically, passive modelocking was first observed in Nd doped glass lasers [1] that were passively Q-switched using saturable dye absorbers. Pulses down to approximately 1 ps were reported. Optically pumped organic dye lasers have a larger gain bandwidth which allows for pulses in the femtosecond range to be produced as well as wavelength tunability [2]. However, dye lasers have the disadvantage that they require expensive pump laser sources and the dye can degrade with time. Dye laser have been replaced over time by solid state lasers. Solid state lasers, based on ion-doped crystals, in particular Ti:Al_2O_3 [3] or glasses, are at the present time mainly used when femtosecond pulses and/or very high pulse energies (up to Joules) are required. Ultra-wide spectra generated from such a laser provide directly a frequency comb [4], which is of high interest for frequency standards [5] and metrology applications. The repetition rate of many of the solid state lasers is typically limited to a couple of hundreds of MHz which is an issue for some applications. Diode pumped fiber lasers can be modelocked [6] to generate short pulses at telecom wavelengths. Multi-GHz repetition rates up to 40 GHz can be obtained with harmonic modelocking [7], however it requires an RF source for the modulation. The pulse durations achieved are limited down to 150 fs by the higher order nonlinearities in the doped fiber used. Semiconductor lasers can also be modelocked through different techniques. Semiconductor MLLs have the advantage that they can be directly electrically pumped, that they are very compact and can be cost effective when fabricated in high volumes. Picoseconds pulses with few tens of milliwatt output power are typically obtained from electrically pump edge emitting

lasers [8]. Very short pulses with high power can also be achieved in optically pumped Vertical External Cavity Surface-Emitting Lasers (VESCELs) [9].

Semiconductor MLL are of interest for a large number of applications which are not restricted to optical telecommunication. For instance, the fastest sampling oscilloscopes currently employ MLLs for optical sampling measurements [10] and in the near future expectations are high for the use of MLLs in high speed analogue to digital conversion [11]. In microelectronics systems, the integration density in circuits is continuously becoming higher and the copper links between the components and sections are becoming so thin that their resistance and associated power loss becomes a problem. The use of MLL pulse sources to interconnect CMOS devices and/or to distribute clock signals in high speed microprocessors [12,13] is investigated by microelectronics companies. A well known medical application of MLLs is the use of Ti-sapphire femtosecond modelocked lasers for surgery in for instance corneal refractive surgery [14]. New medical applications emerging are in optical coherence tomography and multiphoton imaging where semiconductor MLLs can be used in the telecom wavelength range and up to GHz level repetition rates [15,16]. Closer to optical telecommunication, in radio over fiber applications, optical transmitters can make use of MLLs [17].

The motivation for the development of the modelocked lasers in this thesis is their use as optical pulse sources in an All Optical Clock Recovery (AOCR) scheme [18] in Optical Time Division Multiplexing (OTDM) systems [19]. This work was part of the project "Key components for 160 to 640 Gb/s optical time domain multiplexing networking" from the *Freeband Impulse program*. The lasers presented in this thesis can also be used in some of the applications mentioned above. To introduce the reader to modelocked lasers of the type developed in this thesis, the mechanism of passive modelocking is presented in Section 1.2. This is followed by an overview of the contents of the thesis in Section 1.3.

1.2 Passive modelocking mechanism

A modelocked laser, as the name suggests, is a laser with its longitudinal modes locked in phase. Assuming this and calculating the output power of such a laser by normalizing the electrical field (see Equation 1.1), the train of pulses of Figure 1.2.1 is obtained. In Equation 1.1, C_m are the intensities of the phase locked modes. The pulse width is inversely proportional to the optical bandwidth spectrum. The repetition rate depends on the spacing in frequency of the longitudinal modes of the laser cavity. Looking at the laser in a time-dependent view, in e.g. a Fabry-Perot (FP) cavity, there is a single pulse traveling up and down the cavity. The repetition rate of the output of the laser is the inverse of the roundtrip time of the pulse in the laser. The roundtrip-time depends on the group index (Ng) and the physical length of the cavity (L). Thus for a FP cavity the roundtrip-time is $2 \cdot L \cdot Ng/c$. In a ring laser cavity the pulses travel round the ring and the repetition rate is then $L \cdot Ng/c$.

$$I(t) = |E(t)|^2 = \left| \sum_{m=-N}^{m=+N} C_m \cdot e^{i(\omega_0 + \omega_m)\cdot t + \phi_m(t)} \right|^2 \quad \textbf{1.1}$$

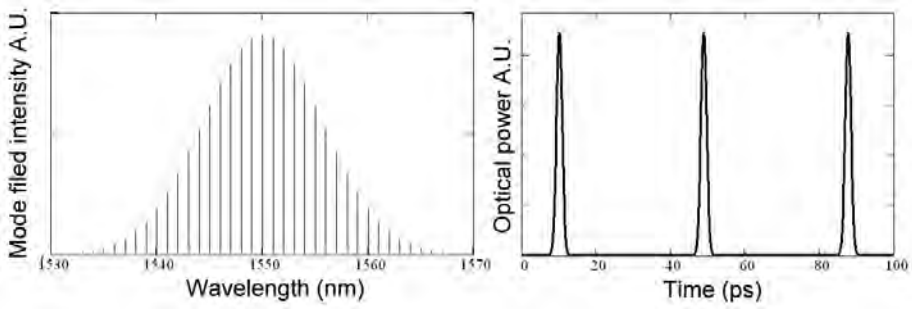

Figure 1.2.1 Mode field intensity profile output power of a modelocked laser.

The modelocking mechanism can be achieved in different ways. The so-called active modelocking technique involves the modulation of the cavity losses at the free spectral range of the cavity or at a harmonic. This modulation is applied to a modulation device in the cavity using an RF source. All the longitudinal modes operating in the cavity are then modulated in intensity at the frequency of the mode-spacing and a constant phase relation will be established between them. In this way optical pulses are created. A passively modelocked laser has its longitudinal modes locked in phase without any RF source. The modes are locked in phase through an internal nonlinear process that couples the longitudinal modes. Shorter pulses can be achieved with passively modelocked lasers than with actively modelocked lasers. An efficient manner to passively modelock a laser is by introducing a Saturable Absorber (SA) in the cavity. In this thesis passive modelocking is studied using a saturable absorber that has a recovery time that is typically longer than the pulse duration achieved. This is called slow saturable absorber modelocking. This has been first discovered in dye lasers in 1966 [1] under Q-switching operation. The first passively modelocked dye laser in continuous operation was reported by French and Taylor in 1986 [20]. The theory of Haus for slow saturable absorber modelocking [21] explains the formation of short pulse as the result of an interaction between the gain saturation and the SA losses as experienced by a pulse traveling in the cavity. As a result of this interaction there is net gain in the cavity for the pulse for only a short period of time. This is illustrated in Figure 1.2.2. A positive net gain window is created when the saturation energy of the SA is several times lower than that of the amplifier and the relaxation time of the SA is faster than the gain recovery of the amplifier. In the semiconductor devices discussed in this thesis, a SA typically has a recovery time in the range of 5 to 30 ps. For the amplifier to fully recover its gain, it takes a time in the

order of one ns. SAs with faster recovery do exist [22,23], however these cannot be used in planar monolithically integrated devices.

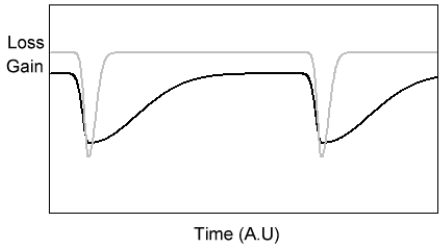

Figure 1.2.2 Gain and losses function of time in passively modelocked laser cavity using a slow saturable absorber.

When a pulse passes through a short SA or an amplifier, the shape of the pulse changes. The SA absorbs the leading edge of a pulse until it gets saturated, then the tail of the pulse is much less absorbed. This phenomenon shortens the pulse by making the leading edge steeper. The amplifier is also saturated during the amplification of a pulse. The leading edge is fully amplified but this is not the case for the tail of the pulse. This phenomenon shortens the pulse as well by reducing the tail end of the pulse. In fact, a wide pulse can then be completely reshaped and narrowed down after a number of roundtrips as shown by a simulation result presented in Figure 1.2.3. Here, a 15 ps wide pulse has been introduced in a MLL cavity and it has been shortened down to 1.8 ps. Also the maximum of the pulse has clearly moved roundtrip after roundtrip. This phenomenon, allows one to tune the repetition rate of a MLL through control of the pulse energy [24]. The optical bandwidth of the roundtrip gain and the nonlinear effects in a MLL limit the minimum pulse width that can be achieved in the laser.

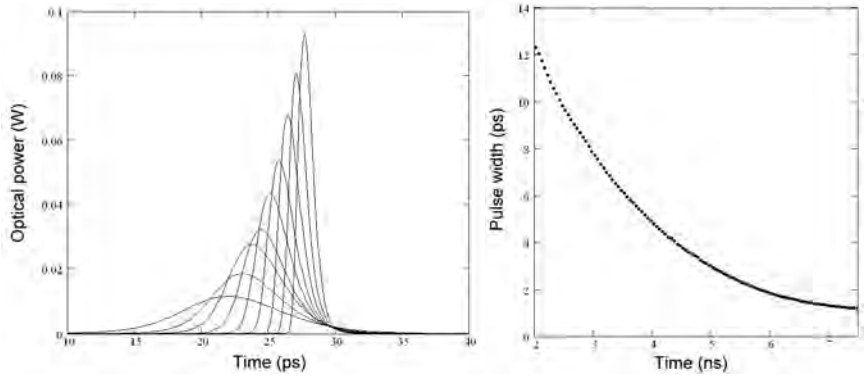

Figure 1.2.3 Pulse reshaping and narrowing in a typical semiconductor modelocked laser cavity. A 15 ps pulse has been initially injected into the cavity.

A transform-limited pulse is a pulse which is as short as its spectral content allows. For instance, for a pulse with a hyperbolic secant square shape, the product of the Full Width at Half Maximum (FWHM) pulse times its optical bandwidth ($\Delta f \cdot \Delta t$) is equal to 0.315 when the pulse is transform limited. When a transform-limited pulse propagates through a medium such as an optical fiber, amplifier or a SA, its time-bandwidth product increases due to dispersion and nonlinearities in the medium. The pulse, when it exits the medium, is not transform-limited anymore: the pulse is chirped (see Figure 1.2.4). The chirp of an optical pulse can be understood as the time dependence of its instantaneous frequency. For instance an up-chirp (down-chirp) means that the instantaneous frequency of the pulse raises (decreases) within the pulse duration. Vice versa, an unchirped pulse has a nearly constant instantaneous frequency. A linearly chirped pulse can be compressed to a transform limited shape by passing the pulse through appropriate dispersive elements of opposite sign [25].

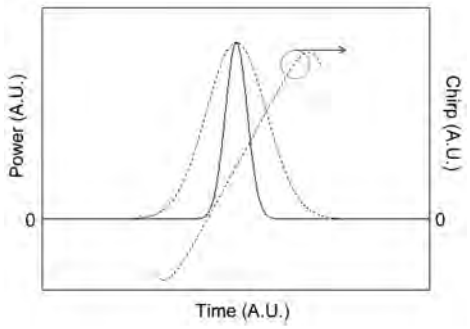

Figure 1.2.4 Transform limited pulse compared with a chirped pulse for the same optical bandwidth.

1.3 Overview of the thesis

The objective of the presented work was to realize compact InP/InGaAsP modelocked lasers, operating in the 1.55 μm wavelength range, in the active-passive integration technology. These devices should be used as optical pulse sources in an AOCR application [18] in OTDM systems [19]. The active-passive integration technology allows for the fabrication and integration of different types of components and thus many different devices on a single chip. The two principal categories of components are those using passive waveguides and those using Semiconductor Optical Amplifiers (SOAs). The integration technique used is a so-called "butt-joint coupling" technique in which the index guiding structure for the passive and active components, is at the same height on the chip. The quality of the transition between the active and the passive waveguide structure, the butt-joint, is essential for modelocked lasers as will be explained in Chapter 5. In this project, the modelocking mechanism used is passive modelocking using a slow Saturable Absorber (SA). The SA is a short SOA section that is reversely biased. In this project, work was largely concentrated on ring laser type cavities. Indeed, much of the published research effort has been focused on monolithic modelocked lasers in Fabry-Pérot (FP) type configurations. A ring configuration has however significant advantages. Firstly, the repetition rate of the laser can be controlled accurately by photolithography as opposed to a device with cleaved facet mirrors. Secondly, a ring laser typically operates as a Colliding Pulse Modelocked (CPM) [26] laser where two counter-propagating pulses collide in the saturable absorber. This improves the modelocking performance, in particular the stability. Furthermore, when active-passive technology is used the laser can be directly integrated with other devices such as an all-optical switch or a pulse compressor [27]. The rise in speed of the optical telecommunication networks creates a drive to increase the repetition rate of modelocked lasers to values like 40 GHz or more. The repetition rate of a modelocked laser is inversely proportional to its cavity length, thus to its foot print. In the case of ring lasers, sharp bends in the waveguides are necessary which in turn required high index contrast waveguides. The active-passive technology presented in this thesis integrates high contrast passive waveguides and 40 GHz laser cavities can be realized.

From the first realization of integrated Ring Mode Locked Lasers (RMLLs) using active-passive integration and a demonstration of a device at 27 GHz [28][Section 5.6], many issues came up. First, the understanding of the modelocking mechanism and other dynamics using a bulk In/InGaAsP material needed to be better understood. To address this issue, a simulation tool of RMLL was developed. It is a bi-directional time domain model which is presented in Chapter 2. Simulation results showed that symmetrical cavities show a much wider operating range for stable modelocking. The transitions from a modelocked state of the laser to another operating regime have been explored with the model. The simulation tool used parameters describing the gain properties of the material. These have been accurately measured using a new type of high resolution spectrum analyser [29]. The method and the results on the characterization of the optical amplifiers are presented in Chapter 3.

Another important issue which came out from the first RMLL realization was the necessity to reduce all the reflections inside the modelocked laser cavity and in particular the reflections of the butt-joint at the active-passive interfaces. Special efforts have thus been made to characterize the optical losses and reflections at the butt-joint [30] and to minimize them. The fabrication technology of the active-passive wafer that has been developed during this project in the COBRA institute is presented in Chapter 3. The active-passive butt-joint reflection has been reduced to a sufficiently low value of less than -50 dB [31]. A reflectivity of -50 dB is a minimum value required for good laser operation [32].

As mentioned previously, the aim of the project was to realize RMLLs with a 40 GHz repetition rate or higher. To validate techniques required to achieve high repetition rate RMLL designs, the realization of more compact devices through the use of deep etching has been investigated in Chapter 4. Results are presented on, at that time, the world's most compact AWG using a double-etch technique [33], and the world's first InAs/InP quantum dot (QD) lasers employing narrow deeply etched ridge active waveguides in the 1.55 μm wavelength region [34]. The performance of the QD lasers appears not to be affected by sidewall recombination effects. Shallowly and deeply etched FP lasers show the same performance. Results obtained from a compact QD ring laser with a free spectral range close to 40 GHz are presented. Before realizing a final RMLL design on an active-passive wafer, a series of all-active devices has been designed, fabricated and characterized. The same layerstack with a bulk gain layer was used as in the active parts of the active-passive material. These all-active chips provided material for the gain measurements presented in Chapter 3 and allowed to look further into short pulse laser characterization techniques and to test designs for reducing reflections from other intra-cavity components. The results of the all-active MLLs are presented in Chapter 5. Firstly, 20 GHz and 40 GHz linear all active Fabry-Pérot MLL (FPMLL) lasers have been successfully fabricated. Modelocking has been achieved with these lasers in the CPM and Self Colliding Pulse Modelocked (SCPM) configurations. Pulse lengths down to 1.6 ps (at 20 GHz) have been observed. A 40 GHz repetition rate was demonstrated in a CPM laser with a Saturable Absorber (SA) positioned in the center of the FP cavity [8]. All-active 15 GHz RMLLs have also been successfully fabricated. These lasers show a relatively good timing stability due to the ring configuration. Measured output pulses are highly chirped and an FWHM bandwidth of up to 4.5 nm was obtained. These results have been published in [35]. Such lasers with high bandwidth pulses and compatible with active-passive integration are of great interest for Optical Code Division Multiple Access (O-CDMA) applications, where information is coded in the spectrum [36]. Finally, first results from MLLs realized on an active-passive wafer are presented in Section 5.5. Passive modelocking has been demonstrated in these integrated Extended Cavity FPMLLs with minimized intra-cavity reflections. Pulses of 2.1 ps duration and with a small pedestal have been observed. The pulses are close to transform-limited. The longer timescale dynamics of the EC-FPMLLs are reduced compared to the all-active FPMLLs, which is understood to be due to the short amplifier section.

The use of a MLL for the AOCR application and a special RMLL design for AOCR are presented in Chapter 6. To begin with, initial test experiments for AOCR and clock frequency division using a 20 GHz Fabry-Pérot MLL are presented. Many characteristics of the AOCR could be quantified. Then, the design of a 40 GHz MLL laser in a ring configuration for an active-passive wafer is presented. The design utilizes all the minimizations of small intra-cavity reflections. Finally, for AOCR application a novel way to couple the optical input signal into the MLL via a separate waveguide has been designed for the 40 GHz RMLL. The timing jitter of the clock recovered from this laser is expected to be sufficiently low to comply with the telecom requirements at 40 GHz [19]. This expectation is based on the accumulated results presented in this thesis and as summarized in the last chapter.

The material contained in the following papers and conference proceedings has been used in the different chapters of this thesis:

Chapter 3:

- Applied Optics, Vol. 45, Issue 35, pp. 9007-9012, (2006)
- IEEE PTL, Vol. 17, Issue 11, pp. 2265-2267, (2005)
- IEEE LEOS Benelux 2005 Mons, Belgium, pp. 249-252 (2005)

Chapter 4:

- IEEE PTL Vol. 16, issue 11, pp. 2478-2480, (2004)
- IEEE PTL Vol. 18, issue 24, pp. 2644-2646, (2006)

Chapter 5:

- IEEE PTL, Vol.17, Issue 11, pp. 2277-2279. (2005)
- ECOC'05, Glasgow, Scotland, Vol. 3, pp. 673-674, (2005).
- Optics Express, Vol. 14, Issue 21, pp. 9716-9727, (2006)

1.4 List of references

1 A.J.D. Maria, D.A. Stretser, H. Heynau, " Self mode-locking of lasers with saturable absorbers" Applied Physics Letters, Vol. 8, Issue 7, pp. 174-176, (1966)

2 R.L. Fork, B.I. Greene and C.V. Shank "Generation of optical pulses shorter than 0.1 psec by colliding pulse mode locking" Applied Physics Letters, Vol. 38, Issue 9, pp. 671-672, (1981)

3 P.F. Moulton, "Spectroscopic and laser characteristics of Ti:Al2O3," Journal Optical Society of America B, Vol. 3, Issue 1, pp. 125-133, (1986)

4 L. Matos, D. Kleppner, O. Kuzucu, T. R. Schibli, J. Kim, E. P. Ippen, and F. X. Kaertner, "Direct frequency comb generation from an octave-spanning, prismless Ti:sapphire laser," Optics Letters, Vol. 29, Issue 14, pp. 1683-1685, (2004)

5 R. Holzwarth,; M. Zimmermann, T. Udem, T.W. Hansch, "Optical clockworks and the measurement of laser frequencies with a mode-locked frequency comb" IEEE Journal of Quantum Electronics, Vol.37, Issue 12, pp.1493-1501, (2001)

6 I.N. Duling III, "All-fiber ring soliton laser mode locked with a nonlinear mirror," Optics Letters, Vol. 16, Issue 8, pp. 539-541,(1991)

7 B. Bakhshi, P.A. Andrekson, "40 GHz actively modelocked polarisation maintaining erbium fibre ring laser" Electronics Letters , Vol. 36, Issue 5, pp.411-413, (2000)

8 Y. Barbarin, E.A.J.M. Bente, M.J.R. Heck, Y.S. Oei, R. Nötzel and M.K. Smit "Passively Modelocked 20 and 40GHz Bulk InGaAsP Lasers" in Proceeding ECOC'05, Glasgow, Scotland, (2005).

9 U. Keller and A. C. Tropper, "Passively modelocked surface-emitting semiconductor lasers" Physics Reports, Vol. 429, Issue 2, pp. 67-120, (2006)

10 M. Shirane, Y. Hashimoto, H. Yamada and H. Yokoyama, "A Compact Optical Sampling Measurement system Using Mode-Locked Laser-Diode Modules" IEEE Photonic Technology Letters, Vol. 12, Issue 11,pp. 1537-1539, (2000)

11 Y. Han, B. Jalali, "Photonic time-stretched analog-to-digital converter: fundamental concepts and practical considerations" Journal of Lightwave Technology, Vol. 21, Issue 12, pp. 3085-3103. (2003)

12 G.A. Keeler, B.F. Nelson, D. Agarval, C. Debaes, N.C. Helman, A. Bhatnagar, D.A.B. Miller, "The benefits of ultrashort optical pulses in optically interconnected systems", IEEE Journal of Selected Topics in Quantum Electronics, Vol. 9, Issue 2, pp. 477-485. (2003).

13 Kobrinsky, M.; Block, B.; Zheng, J-F.; Barnett, B; Mohammed, E.; Reshotko, M.; Robertson, F.; List, S.; Young, I.; Cadien, K. "On-Chip Optical Interconnects." Intel Technology Journal, Vol. 8, Issue 2, ISSN 1535-864X (May 2004).

14 T. Juhasz, F.H. Loesel, R.M. Kurtz, C. Horvath, J.F. Bille, G. Mourou, "Corneal refractive surgery with femtosecond lasers" IEEE Journal of Selected Topics in Quantum Electronics, Vol. 5, Issue 4, pp. 902-910, (1999)

15 J. Bewersdorf, S.W. Hell, "Picosecond Pulsed Two-Photon Imaging With Repetition Rates of 200 and 400 MHz", Journal of microscopy, Vol. 191, Issue 1, pp. 28-38, (1998)

16 W. Drexler "Ultrahigh-resolution optical coherence tomography" Journal of Biomedical Optics, Vol. 9, Issue 1, pp. 47-74 (2004)

17 A.J.C Vieira, P.R. Herczfeld, A. Rosen, M. Ermold, E.E. Funk, W.D. Jemison, K.I Williams, "A mode-locked microchip laser optical transmitter for fiber radio" IEEE transactions on Microwave Theory and Techniques, Vol. 49, Issue 10-2, pp. 1882-1887, (2001)

18 S. Arahira, Y. Ogawa, "Retiming and reshaping function of all-optical clock extraction at 160 Gb/s in monolithic mode-locked laser diode" IEEE Journal of Quantum Electronics, Vol. 41, Issue 7, pp. 937- 944, (2005)

19 E. J. M. Verdurmen, "Optical Time domain add-drop multiplexing employing fiber nonlinearities" PhD Thesis, Eindhoven University of technology, ISBN-13: 978-90-386-1923-1, (2006)

20 P.M.W. French, J.R. Taylor "Passive Mode Locking of an Energy Transfer Continuous-Wave Dye Laser" IEEE Journal of Quantum Electronics, Vol. 22, Issue 8, pp. 1162-1164, (1986)

21 H.A. Haus, "Theory of mode locking with a slow saturable absorber," IEEE Journal of Quantum Electronics, Vol. 11, Issue 9, pp. 736-746, (1975)

22 H.A. Haus "Theory of mode locking with a fast saturable absorber", Journal of Applied Physics, Vol. 46, Issue 7, pp. 3049-3058, (1975)

23 U. Keller, K.J. Weingarten, F.X. Kärtner, D. Kopf, B. Braun, I.D. Jung, R. Fluck, C. Hönninger, N. Matuschek and J. Aus der Au "Semiconductor Saturable Absorber Mirrors (SESAM's) for Femtosecond to Nanosecond Pulse Generation in Solid-State Lasers" IEEE Journal Of Selected Topics In Quantum Electronics, Vol. 2, Issue 3, pp. 435-453, (1996)

24 S. Arahira, Y. Ogawa, "Repetition-frequency tuning of monolithic passively mode-locked semiconductor lasers with integrated extended cavities" IEEE Journal of Quantum Electronics, Vol. 33, Issue 2, pp. 255-257, (1997)

25 H.G. Winful, "Pulse compression in optical fiber filters", Applied Physics Letters, Vol. 46, Issue 6, pp. 527-529 (1985)

26 S Bischoff, J Mørk, T Franck, S D Brorson, M Hofmann, K Fröjdh, L Prip and M P Sørensen "Monolithic colliding pulse mode-locked semiconductor lasers" Quantum Semiclassical Optics, Journal of the European Optical Society B, Vol.9, Issue 5, pp. 655-674 (1997)

27 M.J.R. Heck, E.A.J.M Bente, Y. Barbarin, D. Lenstra and M.K. Smit "Simulation and Design of Integrated Femtosecond Passively Mode-locked Semiconductor Ring Lasers

Including Integrated Passive Pulse Shaping Components" IEEE Journal of Selected Topics in Quantum Electronics, Vol. 12, Issue 2, pp 265-276, (2006)

28 Y. Barbarin, E.A.J.M Bente, M.J.R. Heck, J.H. den Besten, G. Guidi, Y.S. Oei, J.J.M. Binsma, M.K. Smit, " Realization and Modeling of a 27-GHz Integrated Passively Mode-Locked Ring Laser", IEEE Photonic Technology Letters, Vol. 17, Issue 11, pp. 2277-2279, (2005)

29 Y. Barbarin, E.A.J.M Bente, L. Mussard, G. Servanton, Y.S. Oei, R. Nötzel and M.K. Smit "Gain Measurements of Fabry-Pérot InP/InGaAsP Lasers using an Ultra High Resolution Spectrometer" Applied Optics, Vol. 45, Issue 35, pp. 9007-9012 (2006)

30 Y. Barbarin, E.A.J.M. Bente, C. Marquet, E.J.S Leclère, J.J.M. Binsma and M.K. Smit. "Measurement of Reflectivity of Butt-Joint Active-Passive Interfaces in Integrated Extended Cavity Lasers" IEEE Photonics Technology Letters, Vol. 17, Issue 11, pp. 2265-2267, (2005)

31 Y. Barbarin, E.A.J.M Bente, T. de Vries, J.H. den Besten, P.J. van Veldhoven, M.J.H. Sander-Jochem, E.J. Smalbrugge, F.W.M.v. Otten, E.J. Geluk, M.J.R. Heck, X.J.M. Leijtens, J.G.M. van der Tol, F. Karouta, Y.S. Oei, R. Nötzel and M.K. Smit "Butt-Joint Interfaces in InP/InGaAsP waveguides with Very Low Reflectivity and Low Loss" IEEE LEOS Benelux 2005 Mons, Belgium

32 R.W. Tkach and A.R. Chraplyvy, "Regimes of feedback effects in 1.5 um distributed feedback lasers", Journal of Lightwave Technology, Vol 4, pp. 1655-1661, (1986)

33 Y. Barbarin, X.J.M. Leijtens, E.A.J.M. Bente, C.M. Louzao, J. Kooiman, M.K. Smit. "Extremely small AWG demultiplexer fabricated on InP by using a double-etch process" IEEE Photonics Technology Letters, Vol. 16, Issue 11, pp. 2478-2480, (2004)

34 Y. Barbarin, S. Anantathanasarn, E.A.J.M. Bente, Y.S. Oei, M.K. Smit and R. Nötzel "1.55 μm Range InAs/InP Quantum Dot Fabry-Pérot and Ring Lasers using Narrow Deeply Etched Ridge Waveguides" IEEE Photonics Technology Letters, Vol. 18, Issue 24, pp. 2644-2646, (2006)

35 Y. Barbarin, E.A.J.M Bente, M.J.R. Heck, Y.S. Oei, R. Nötzel and M.K. Smit "Characterization of a 15 GHz Integrated Bulk InGaAsP Passively Modelocked Ring Laser at 1.53μm" Optics Express, Vol. 14, Issue 21, pp. 9716-9727, (2006)

36 C. Ji, R. G. Broeke, Y. Du, Jing Cao, N. Chubun, P. Bjeletich, F. Olsson, S. Lourdudoss, R. Welty, C. Reinhardt, P. L. Stephan, and S. J. B. Yoo "Monolithically integrated InP-based photonic chip development for O-CDMA systems" IEEE Journal of Selected Topics in Quantum Electronics, Vol. 11, Issue 1, pp. 66-77 (2005).

Chapter 2
Modelocked laser theory and simulations

2.1 Overview of modelocked laser theory

In this thesis 1.55 μm semiconductor modelocked lasers are investigated and developed. This requires the development of a simulation tool of such lasers in order to get to a comprehensive understanding of the mechanism of passive modelocking and to be able to design devices. The model that has been developed and which is presented in this chapter is a bi-directional time domain model for Ring ModeLocked Lasers (RMLLs). The modelocking mechanism studied and used in this thesis is a passive modelocking using a slow Saturable Absorber (SA). The SA is a short Semiconductor Optical Amplifier (SOA) section that is reversely biased. The model developed here is applied to the bulk 1.55 μm InGaAsP active medium, which is used in the active-passive integration scheme presented in Section 3.2 and in [1]. The model may also be used, with the appropriate parameters, with quantum well gain media. The passive components are passive waveguides and passive couplers and the active components are SOAs which are either: an amplifier, a SA, or an isolation section between amplifier and SA.

The first reported work on the modeling of modelocking using a slow SA is from Haus [2] in the middle of the seventies of the previous century. Then the research in this field had continued with the development of semiconductor modelocked lasers in the nineties. As identified and discussed by Avrutin et al. [3] in 2000, there are two main types of time-domain modelocking theories. There are the lumped-element models [4], [5] and the fully distributed time-domain models [6]. Another approach that is well developed is a traveling wave model [7,8,9]. Recently Heck et al. [10] presented a model with a lumped-element approach where the propagation of the pulse through the SOA and the SA were calculated using a distributed time-domain model. The SOA rate equations used in his model are based on a model from Tang and Shore [11] which includes Carrier Heating (CH) effects, two photon absorption (TPA) and Ultrafast Nonlinear Refraction (UNR). These non-

linear effects are included in the model presented in this chapter. The model developed here is fully in the time domain except for the bandwidth limitation in the laser. It is bi-directional to describe realistic laser systems which usually operate with pulses traveling in both directions. For the description of the SOA, the model of Tang and Shore has been extended with bidirectional fields, separate radiative and non-radiative carrier recombination processes [12] and a logarithm gain-carrier relation. This gain relation has been validated for the bulk material used in the RMLL described in [13] and Section 3.4. The effect of the limited optical bandwidth of the SOA is not included in the rate equations of the SOA, but in a separate element in the model. This element is a bi-directional digital low-pass filter which stabilizes the system by limiting the bandwidth each roundtrip, in accordance with the spectral gain profile of the amplifier.

In the following section, the model for RMLL is described in details. Finally in Section 2.3, the model is used for the simulation of symmetric and asymmetric 20 GHz modelocked ring lasers. Taking into account the results of the simulations and the experimental results from different modelocked lasers that are presented in Chapter 5, a new RMLL design has been produced. This new design is presented in Chapter 6.

2.2 Modeling of integrated semiconductor lasers

2.2.1 Description of the model

In this section a bi-directional time domain model of a modelocked ring laser is presented that is based on a set of rate equations for a SOA. This system of differential equations relates the density of photons and charge carriers in the device to the injection current. Five different components are used in the extended cavity RMLL: passive waveguides, amplifiers, absorbers, isolation sections and a coupler. In this model, the ring laser is divided into segments that we assume equal in optical length (Figure 2.2.2). There are five types of segment required for the different components. Uniform photon and carrier densities (for active components) are assumed in the segments. The time for the light to travel through one segment is 25 fs which is the discretization time (Tseg). Each 25 fs the evolution of the photon densities (Clock Wise and Counter Clock Wise) and carrier densities is calculated for all segments. Then the photon densities are transferred to the neighboring segments and the carrier density values are kept in the same active segments for the next step.

The SOA rate equations of the model presented here include nonlinear effects in the same formalism as Tang and Shore in [11]. The nonlinear effects are Carrier Heating (CH), two photons absorption (TPA) and Ultrafast Nonlinear Refraction (UNR). The rate equations have been extended to take into account bidirectional fields (CW and CCW). Also, the model presented here makes the distinction between radiative and non-radiative carrier recombination processes [12]. Finally, in the rate equations of the SOA a logarithmic gain model is used that has been validated experimentally in [13] and the Section 3.4 of this thesis. The gain-carrier relation used is given in Equation 2.1, where aN is the linear gain coefficient, N_0 the material transparency carrier density and N the carrier density. The relation is illustrated in Figure 2.2.1. The average carrier density in the amplifier inside the laser above threshold is around two times N_0. A linear gain-carrier relation is commonly used in lasers since the typically the variation in carrier density in the amplifier in time is over a limited range. However it can be seen that the slope of the curve becomes smaller at higher values of N and that the linear gain coefficient would need to be corrected [4]. Using the logarithmic relation, no correction is needed. Furthermore, this relation is more flexible for the simulation of various type of RMLL with different amplifier length and thus different averaged carrier densities.

$$g_m = aN \cdot N_0 \cdot \ln\left(\frac{N}{N_0}\right) \qquad \textbf{2.1}$$

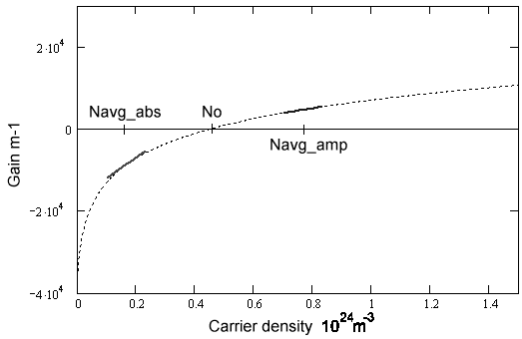

Figure 2.2.1 Plot of the logarithmic gain carrier density relation. The averaged carrier densities in the amplifier and the SA in a modelocked ring laser are indicated.

Each SOA segment is described by the following rate equations:

$$\frac{\partial S_1}{\partial t} = S_1 \cdot \frac{C_{S0} \cdot \ln\left(\frac{N}{N_0}\right) - C_{S1} \cdot (S_1 + S_2)^2}{1 + C_2 \cdot (S_1 + S_2)} - C_{S3} \cdot S_1^2 - Loss_1 \cdot S_1 - Loss_2 \cdot N \cdot S_1 + C_{S4} \cdot N^2 \qquad \textbf{2.2}$$

$$\frac{\partial S_2}{\partial t} = S_2 \cdot \frac{C_{S0} \cdot \ln\left(\frac{N}{N_0}\right) - C_{S1} \cdot (S_1 + S_2)^2}{1 + C_2 \cdot (S_1 + S_2)} - C_{S3} \cdot S_2^2 - Loss_1 \cdot S_2 - Loss_2 \cdot N \cdot S_2 + C_{S4} \cdot N^2 \qquad \textbf{2.3}$$

$$\frac{\partial N}{\partial t} = -(S_1 + S_2) \cdot \frac{C_{N0} \cdot \ln\left(\frac{N}{N_0}\right) - C_{N1} \cdot (S_1 + S_2)^2}{1 + C_2 \cdot (S_1 + S_2)} + C_{N3} \cdot (S_1 + S_2)^2 - A \cdot N - B \cdot N^2 - C \cdot N^3 + Wp \qquad \textbf{2.4}$$

$$\frac{\partial \varphi_1}{\partial z} = \frac{C_{\varphi 0} \cdot \ln\left(\frac{N}{N_0}\right) \cdot (S_1 + S_2) + C_{\varphi 1} \cdot (S_1 + S_2)^2}{1 + C_2 \cdot (S_1 + S_2)} - C_{\varphi 3} \cdot \ln\left(\frac{N}{N_0}\right) - C_{\varphi 4} \cdot (S_1 + S_2) \qquad \textbf{2.5}$$

$$\frac{\partial \varphi_2}{\partial z} = \frac{C_{\varphi 0} \cdot \ln\left(\frac{N}{N_0}\right) \cdot (S_1 + S_2) + C_{\varphi 1} \cdot (S_1 + S_2)^2}{1 + C_2 \cdot (S_1 + S_2)} - C_{\varphi 3} \cdot \ln\left(\frac{N}{N_0}\right) - C_{\varphi 4} \cdot (S_1 + S_2) \qquad \textbf{2.6}$$

Here S_1 and S_2 are the Clock Wise and Counter Clock Wise photon densities, φ_1 and φ_2 are the CW and CCW phases. In the two photon density equations for CW (2.2) and CCW propagation (2.3): C_{S0} is the linear gain contribution; C_{S1} is the nonlinear gain compression factor due to two-photon absorption; C_2 is the nonlinear gain compression factor due to spectral hole burning and carrier heating; C_{S3} is the two-photon absorption coefficient; $Loss_1$ is the scattering loss and the free carrier loss in the cladding; $Loss_2$ is the free carrier absorption within the active layer [14]; C_{S4} is the bimolecular recombination contribution. In the carrier density equation: C_{N0}, C_{N1},

C_{N3} and C_2 are the same contributions as C_{S0}, C_{S1}, C_2 and C_{N3}; A is the inverse of the carrier lifetime; B is the bimolecular recombination rate; C is the Auger recombination coefficient and Wp is the pump rate. In the two phase equations: $C_{\varphi 0}$, $C_{\varphi 1}$, $C_{\varphi 3}$ and C_2 are the same contributions as C_{s0}, C_{s1}, C_2 and C_{s3}, $C_{\varphi 4}$ is the ultrafast nonlinear refraction coefficient.

In detail:

$$C_{S0} = aN \cdot \Gamma \cdot Vg \cdot N_0 \qquad C_{N0} = aN \cdot Vg \cdot N_0 \qquad C_{\varphi 0} = \frac{1}{2} \cdot \alpha T \cdot \varepsilon_1 \cdot aN \cdot \hbar \cdot \omega \cdot Vg \cdot Surf \cdot N_0$$

$$C_{S1} = \varepsilon_2 \cdot \hbar^2 \cdot \omega^2 \cdot Vg^3 \cdot \frac{Surf^2}{\Gamma^2} \qquad C_{N1} = \varepsilon_2 \cdot \hbar^2 \cdot \omega^2 \cdot Vg^3 \cdot \frac{Surf^2}{\Gamma^3} \qquad C_{\varphi 1} = \frac{1}{2} \cdot \alpha T \cdot \varepsilon_2 \cdot \hbar^2 \cdot \omega^2 \cdot Vg^2$$

$$C_2 = \varepsilon_1 \cdot \hbar \cdot \omega \cdot Vg \cdot \frac{Surf}{\Gamma}$$

$$C_{S3} = \Gamma_2 \cdot \beta_2 \cdot \hbar \cdot \omega \cdot Vg^2 \qquad C_{N3} = \frac{\Gamma_2}{\Gamma} \cdot \beta_2 \cdot \hbar \cdot \omega \cdot Vg^2 \qquad C_{\varphi 3} = \frac{1}{2} \cdot \alpha N \cdot aN \cdot \Gamma \cdot Vg \cdot N_0$$

$$Loss_1 = \frac{(Loss_{scat} + Loss_{clad}) \cdot L_{seg}}{T_{seg}} \qquad Loss_2 \frac{Loss_{freecar} \cdot L_{seg}}{T_{seg}}$$

$$C_{S4} = B \cdot \Gamma \cdot \beta$$

$$C_{\varphi 4} = \Gamma_2^{'} \cdot \frac{\omega}{c} \cdot n_2 \cdot \hbar \cdot \omega \cdot Vg$$

Where Γ the linear confinement factor, Vg the group velocity, ε_2 the nonlinear gain compression factor to TPA, ω the pulsation, ε_1 the nonlinear gain compression factor, $Surf$ the surface of the active region, Γ_2 the confinement factor for TPA, Γ_2' the confinement factor for UNR, c the speed of light, T_{seg} the time segment, L_{seg} the physical length of one segment, β the spontaneous emission coupling factor, αN the carrier density linewidth enhancement factor and αT is the temperature linewidth enhancement factor. β_2 is the coefficient for two-photon absorption and n_2 is the nonlinear gain refractive index. All the parameters used are listed in Table 2.2.1.

The Saturable Absorber (SA) is a short SOA that is reversely biased [15]. It is described with the same rate equations as the amplifier without carrier injection. In the SA in an operating MLL the carrier density varies in time between low background values and the transparency carrier density value. In Figure 2.2.1, it can be seen that within this range, the slope of the gain-carrier relation curve varies by a significant amount. The logarithmic gain-carrier relation has its limit when the carrier density in the SA is very low. The absorption then becomes unrealistically high. This is prevented by introducing a minimum carrier density background value in the SA. It has been reported that the carrier lifetime of a saturable absorber depends of the reverse bias voltage applied [16], but such a relation has not been implemented in the model. The carrier lifetime is the only parameter that is tuned. The model presented here is bidirectional, thus two pulses can meet in the SA. For a very short SA (less than a few wavelengths), coherent effects need to be taken into account. However for MLLs with ridge waveguides, the coherent effects are small in the SA [17] and therefore have not been implemented in the model.

Table 2.2.1: Parameters used in the model

Symbol	Description	value
aN	Linear gain coefficient	$4.05 \cdot 10^{-20}$ m²
$N0$	Transparency carrier density	$0.4 \cdot 10^{24}$ m^{-3}
Γ	Linear confinement factor	0.259
Γ_2	Confinement factor for TPA	0.5
Γ_2'	Confinement factor for UNR	0.4
Vg	Group velocity	$80 \cdot 10^6$ m/s
ε_1	Nonlinear gain compression factor	0.2 W^{-1}
ε_2	Nonlinear gain compression factor to TPA	200 W^{-2}m^{-1}
ω	Pulsation / wavelength	1.55 μm
$Surf$	Surface of the active region	0.12 x 2.0 μm²
n_2	Nonlinear gain refractive index	$-3.5 \cdot 10^{-16}$m²/W
T_{seg}	Time segment	25 fs
β	Spontaneous emission coupling factor	10^{-5}
β_2	Coefficient for TPA	37cm/GW
A	One over the carrier life time	$1.67 \cdot 10^{-9}$ s^{-1}
B	Bimolecular recombination rate	$2.602 \cdot 10^{-16}$ m^{3}s^{-1}
C	Auger recombination coefficient	$5.269 \cdot 10^{-41}$ m^{6}s^{-1}
αT	Temperature linewidth enhancement factor	2.0
αN	Carrier density linewidth enhancement factor	4.0
$Loss1$	Scattering loss and free carrier loss in the cladding	2000 m^{-1}
$Loss2$	Free carrier absorption within the active layer	$5.0 \cdot 10^{-22}$ m²

The isolation sections between an amplifier and a SA are considered as non-reversely biased SA with carrier lifetime of 200 ps. In passive waveguides, only the passives losses are taken into account. Intensities of pulses are not sufficiently high to introduce non linear effects in the passive waveguides [18]. Finally, the effect of the limited optical bandwidth of the SOA has not been included in the rate equations of

the SOA listed above. The limitation of the optical bandwidth is done separately at each roundtrip using a bi-directional digital low-pass filter [19]. Section 2.2.2 describes in details the digital filter used.

In this thesis, a RMLL cavity where the two counter propagating pulses experience the same optical path, but in opposite direction, is called a symmetric cavity. If not, the cavity is asymmetric. Besides, a modelocked laser which has two counter propagating pulses meeting in a SA, is in a Colliding Pulse Modelocked (CPM) [20] configuration. This is automatically the case for a RMLL (in case there are no provisions to make it unidirectional). Shorter pulses are generally obtained with such a configuration [20]. Figure 2.2.2 presents a diagram of a possible RMLL symmetric configuration. At the top of the figure, a coupler element couples the light in and out of the ring. This is done coherently for both directions in the model. At the bottom of the figure, in the middle of an amplifier is a SA isolated by two isolation sections. The white segments are passive waveguides. The bandwidth limitation obtained by filtering is done for each direction just before the light is coupled out of the ring. The model presented here has been developed for RMLL cavities, but it can be easily modified to a Fabry-Pérot cavity with two end-mirrors. The implementation of the model in program is briefly presented in 2.2.3.

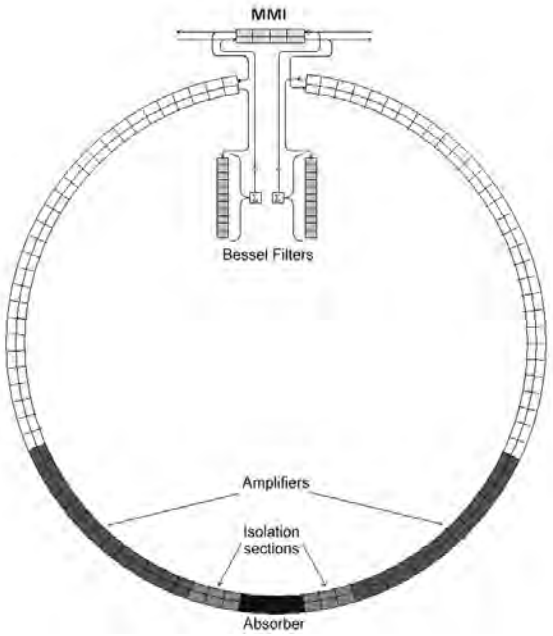

Figure 2.2.2 Diagram of the symmetric ring modelocked laser segmented for the simulation. The connections between the coupler, the ring and the Bessel filters are shown.

2.2.2 Bandwidth limitation using a digital Bessel filter

In order to keep the model fully in the time domain, a digital filter has been introduced to simulate the bandwidth of the SOA. A low-pass digital Bessel filter [19] has been chosen for this. Its parameters have been set so that the transmission curve is close to the measured gain curve (Section 3.4) as can be seen from Figure 2.2.3.a). Important is also that such a digital Bessel filter has a very low distortion of the phase. The filter is a digital difference equation (Equation 2.7). The difference equation computes the output electrical field strength and phase at the time *n*, based on present and past input electrical field and past output electrical field.

$$y[n] = \sum_{k=0}^{order} b_k \cdot x[n-k] + \sum_{l=1}^{order} -a_l \cdot y[n-k] \qquad \textbf{2.7}$$

In Equation 2.7, x[n] is the present input signal (complex field amplitude), x[n - k] is the array with the past input signal, y[n - k] is the array with the past output signal (complex field amplitude), a is a vector of filter feedback coefficients, and b is a vector of filter feedforward coefficients. These coefficients determine the properties of the filter. One possible signal flow graph for the filter is given in Figure 2.2.3.b). The storage of past samples is represented by boxes labeled "z^{-1}". This diagram is used because it can be directly converted to the frequency domain by replacing all time-domain signals by their respective Z-transforms [21]. The idea contained within the Z-transform was previously known as the "generating function method".

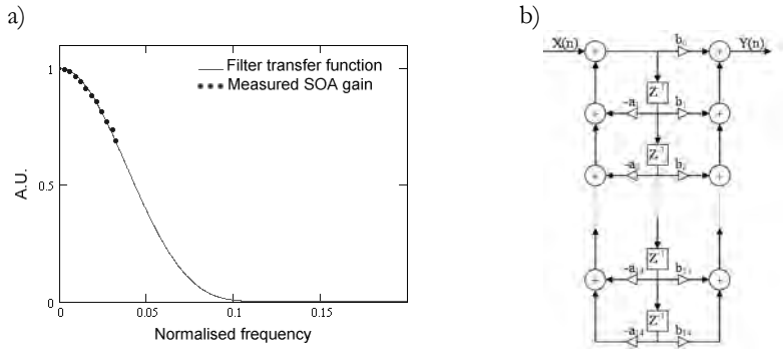

Figure 2.2.3 a) The transfer function of the digital filter used, plotted with the measured bulk SOA gain as a function of the normalized frequency ($\Omega = \omega \cdot T_{seg} / 2\pi$). b) Signal flow graph of a digital filter. "z^{-1}" represents a Z-Transform. "*a*" and "*b*" are the feedback and feedforward coefficients of the filter.

The MathCad® software package has been used to calculate the feedback and feedforward coefficients of the Bessel filter. The bandwidth of the SOA has been

measured to be 21.6 THz (0.086 in a normalized frequency) [13]. The order of the filter that is required has been tested. The 14th order turned out to be sufficiently robust for our application. In the calculations the a and b coefficients need to be used with an accuracy that is two orders of magnitude greater than the order of the filter. This type of digital filter conserves the causality of the signal but it has a delay. The delay is one over the normalized frequency cut, which in our case corresponds to approximately 22 segments of 25 fs. This delay can be compensated in the passive region of the ring where only the passive losses are playing a role. The use of a digital filter is much simple than using a Fourier Transform (FT), spectral filtering and back FT as in [10].

2.2.3 Implementation of the model in a program

The model has been implemented in a C program using LabWindows® CVI. A screenshot of the interface created is given in Figure 2.2.4. The program requires at least two input files. The first one contains all the parameters listed in Table 2.2.1, with in addition the parameters defining the design of the RMLL and the coefficients of the digital Bessel filter. The second input file contains tables with CW and CCW input light intensities and phases for a time series. A third input file can be used containing the initial carrier densities of the active elements.

As mentioned above, every 25 fs the photon densities (CW and CCW) and carrier densities are calculated for all segments. Then the photon densities are transferred to the next segments and the carrier density values are saved in active segments for the next step. The integration of the rate equation is done using the Runge-Kutta method with a fixed step size [22]. At each roundtrip, the output intensities and phases are plotted on the interface and saved at the end of a text file. The carrier densities of the amplifier, isolation sections and SA are saved for each roundtrip in a different file and plotted on the interface in two graphs. The simulation of a 20GHz RMLL with 1000 active elements and for a 1000 roundtrips takes ~50 minutes using a laptop under Windows XP with a 1.6 GHz Intel Pentium M 730 processor.

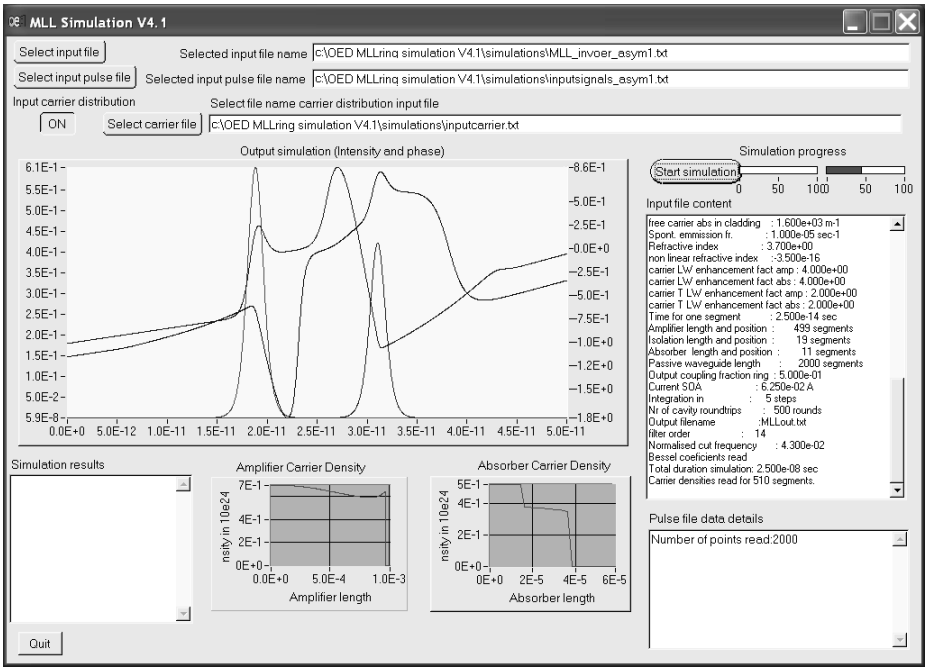

Figure 2.2.4 Interface of the simulation program realized in C with LabWindows CVI.

2.3 Simulation of symmetric and asymmetric 20 GHz RMLL

2.3.1 Introduction

The model previously introduced has been used to study a symmetric and an asymmetric 20 GHz RMLL design. The results are presented in the two following sections. The RMLLs can be realized with the COBRA technology [23]. The choice of the design parameters studied has been guided by the results obtained experimentally from an 18 GHz integrated extended cavity Fabry-Pérot MLL (EC-FPMLL) presented in Section 5.5. Indeed the dimensions of the RMLL amplifier and SA studied are similar to the experimental design of the EC-FPMLL. Simulation results show that a symmetrical cavity is better for stable modelocking. Transitions from the modelocked state of the laser to other operating regimes can be explained by the model. The simulation results of the asymmetric RMLL show that a modelocking regime is more difficult to achieve. The competition between the CW and the CCW modes in the asymmetric case makes the laser more unstable in most situations. However, it can clearly be seen that depending on the amount of absorption in the SA in the cavity, the laser can operate with two counter-propagating pulses with significantly different peak intensities.

2.3.2 Simulation of a symmetric RMLL

The design of a 20 GHz symmetric RMLL is plotted in Figure 2.3.2. The cavity is segmented for the simulation in different sections as shown previously in Figure 2.3.1. The total length of the ring laser is 4 mm (2000 segments). The two amplifiers are 472 μm long (236 segments). The choice of the length of the SA is based on the length of the SAs in successfully modelocked FPMLL devices presented in Section 5.5: absorber lengths of 10 and 12.5 μm. In a ring cavity, there are two counter-propagating pulses which meet in the SA. It can be seen as two FPMLL lasers joined at the SAs; the resulting SA is then two times as long. For the simulation, the SA was set at 22 μm long (11 segments). It is isolated from the amplifiers by two 16 μm long (8 segments) isolation sections. The light is coupled in and out from the ring with a coupler with 50% out-coupling ratio.

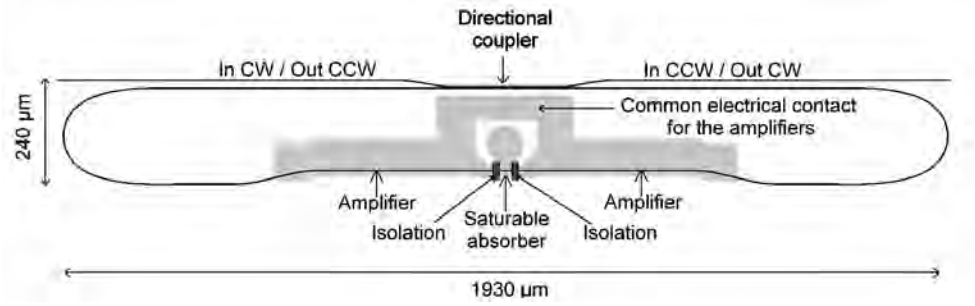

Figure 2.3.2 Design of a symmetric 20 GHz modelocked ring laser on an active-passive wafer. The active region is 1000 µm long and centered is a 22 µm long SA. The isolation sections are 16 µm long.

The model includes spontaneous emission, which allows simulating the self-starting of the laser. As an example, a simulated output power during start-up of the laser is plotted in Figure 2.3.3 (without light injected) for settings that lead to a stable modelocked state. Below 0.3 ns, the amplifiers amplify the small amount of spontaneous emission and the carrier concentration increase to large values. Three aspects can be identified in the start-up of the modelocked laser. The laser starts with relaxation oscillation behavior which ends after five or so oscillations. The second aspect is that the modelocking action of the absorber can be seen right from the start and after only 2 to 3 ns the laser produces pulses and only a small amount of CW background light. Then the pulse length decreases further in time as shown in Figure 2.3.3 (right axis). After that the third aspect can be seen. The short pulse length makes that the self-phase modulation becomes important. The short pulse may break-up a couple of times before its phase profile becomes stable. The laser then settles to a stable modelocked state.

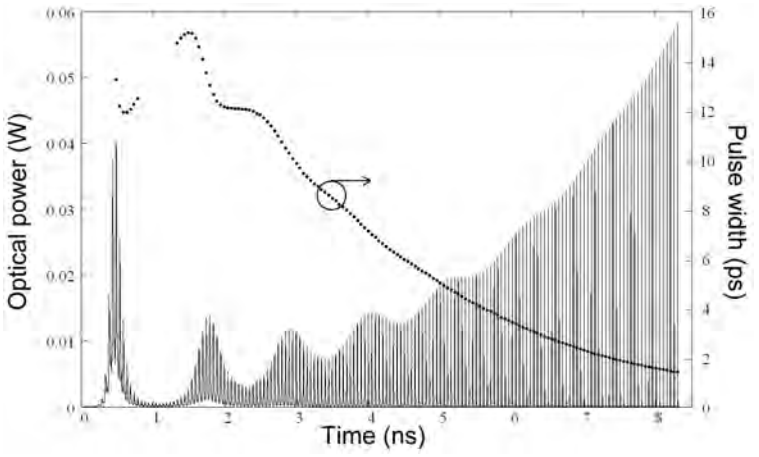

Figure 2.3.3 Simulated output power and calculated pulse width of the laser as a function of time. The laser is self-starting. I = 65 mA τ_{SA} = 11 ps.

Simulations of the symmetric RMLL have been performed for different amplifier current and SA carrier lifetime values to establish the stability region for modelocking. To save computer time, two 2 ps pulses with a null phase have been injected into the cavity to start the simulation. The laser threshold is 57.5 mA. The different regimes of the laser are plotted in Figure 2.3.4. The laser is properly modelocked for amplifier current values between 62 mA and 75 mA and SA carrier lifetime values between 9 and 15 ps. The results obtained for parameters in the modelocked regime on the boundary of the stability region are stable over 5 ns. At high current injection (> 75 mA) and for any SA carrier lifetime, the laser is in a Q-switching regime. For short SA carrier lifetime (<7 ps) and a current in the amplifier which is not too high, the laser produces short pulses, modulated in intensity. This regime is a two-dimensional quasi-periodic dynamic (taurus) [24]. There are two regions where the laser is unstable. In the first region instable around 65 mA amplifier current and 15 ps SA carrier lifetime, a second pulse in the roundtrip time attempts to be present. In the second region unstable around 72.5 mA amplifier current and 9 ps SA carrier lifetime, the laser switches irregularly between a self-pulsating regime to more stable state. Each regime is studied in more detail in the following paragraphs.

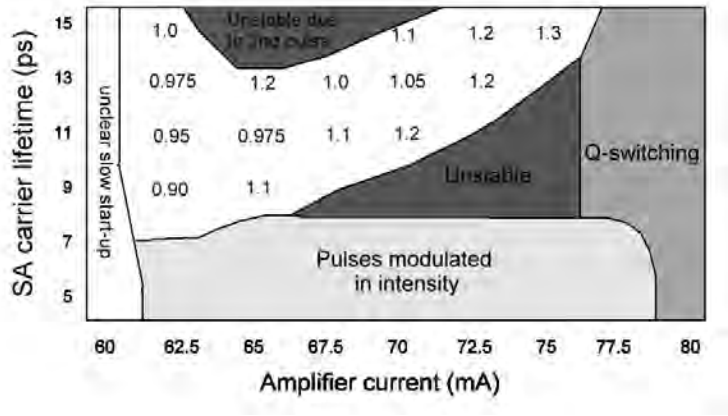

Figure 2.3.4 Different regimes of the symmetric 20GHz RMLL function of amplifier current and SA carrier lifetime. The pulse width is mentioned in picoseconds if the laser is modelocked.

In the stable modelocking region, as can be seen in Figure 2.3.4, the pulse width increases with the current, except next to the unstable region. At lower current, the pulse is less intense; it saturates less the SA which vice-versa narrows down the pulse more efficiently. In the same way the pulse width decreases with the carrier lifetime of the SA, except close to the unstable regimes. The most stable modelocked regime (over 20 ns simulated) has been found for 65 mA amplifier current and 11 ps SA carrier lifetime. The simulated output power as a function of time is plotted in Figure 2.3.5. The measured pulse width is constant after 8 ns and the amplitude modulation is small (<10%). The pulse obtained is plotted in Figure 2.3.6 with the corresponding calculated optical spectrum. The pulse is 0.95 ps wide with a 70 mW peak power and it is slightly down-chirped (65 GHz). Unidirectional simulations of Heck et al. predicted up-chirped pulses with higher chirp values. The change of sign is attributed to the CPM configuration. Using a Fourier Transform (FT), the optical spectrum has been calculated with 100 pulses. The calculated spectrum is 2.6 nm at FWHM; the pulse is almost transform-limited. The chirp of the pulses stays limited due to the integrated extended cavity.

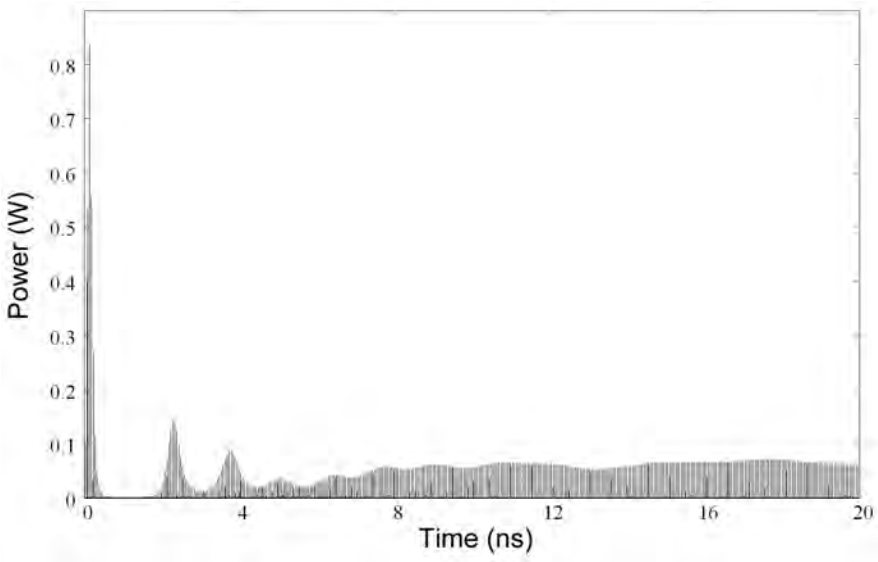

Figure 2.3.5 Simulated output power of the 20 GHz symmetric RMLL function of time. Two low power 2 ps pulses with a phase null were injected in both direction of the cavity to speed up the start of the laser. I = 65 mA τ_{SA} = 11 ps.

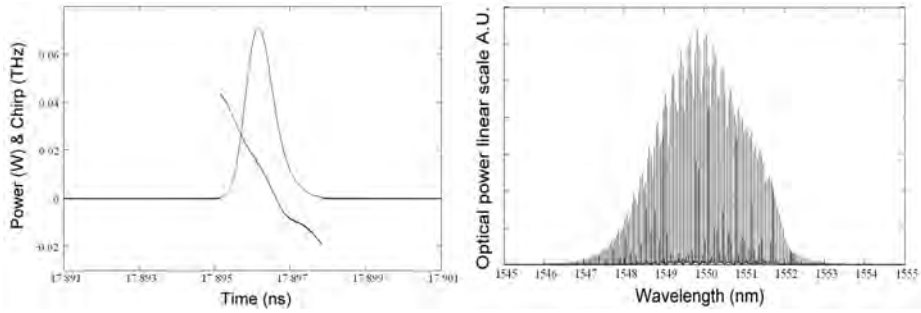

Figure 2.3.6 Simulated output pulse shape and chirp with the corresponding calculated optical spectrum. Width = 0.95 ps , Peak power = 70 mW ; Chirp = 65 GHz (~linear); Bandwidth = 2.6 nm; for I = 65mA & τ_{SA} = 11ps.

The two dimensional quasi-periodic regime at a short SA recovery time (<7 ps) is illustrated by the simulated output power of the laser in Figure 2.3.7. This regime is stable after 5 ns. The peak intensities of the pulses vary from 120 mW to 60 mW every 1.3 ns (770 MHz). In the same way, the pulse width varies from 0.75 ps to 1.05 ps. The narrowest and the widest pulses are plotted in Figure 2.3.8. In both cases the chirp is small (< 60 GHz) and there is a down-chirp. The evolution of the pulse width in time is shown in Figure 2.3.9. In this regime the SA recovers faster and the

absorption is higher. The amplitude modulation can be reduced by increasing the gain in the cavity. Indeed, simulations with a higher injection current in the amplifier show that the modulation decreases and pulses narrow down. But, if the current is increased further, pulses start to break-up. No proper modelocking without amplitude modulation has been simulated for this design at such a short SA recovery time.

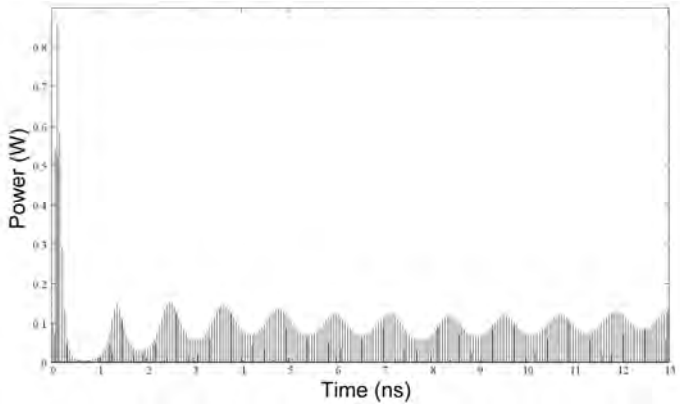

Figure 2.3.7 Simulated output power of the 20 GHz symmetric RMLL as a function of time with a relatively short SA lifetime. Two low power 2 ps pulses with a phase null were injected in both direction of the cavity to speed up the start of the laser. I = 62.5mA, τ_{SA} = 5ps.

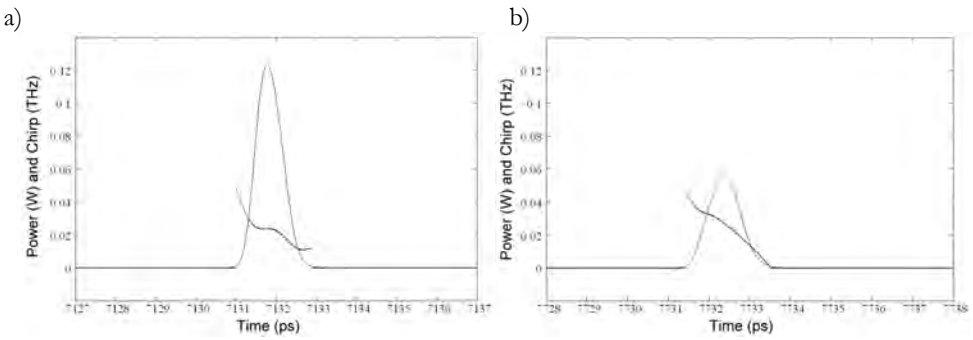

Figure 2.3.8 Simulated output pulses for the two extreme cases, I = 62.5mA τ_{SA} = 5ps:
a) Peak power = 122mW, width = 0.75 ps, down chirp = 30GHz (nonlinear)
b) Peak power = 58 mW, width = 1.05 ps, down chirp = 50GHz (~linear)

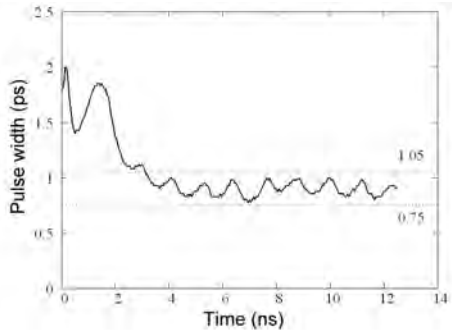

Figure 2.3.9 Simulated pulse width function of time for I = 62.5mA τ_{SA} = 5ps.

Longer timescale Q-switching like variations in output power are observed in combination with short pulse output with repetitive pulse break-up. These phenomena that occur in the modelocked laser at high injection current (over 76 mA in this design) can be understood by analyzing the simulated time series in detail. The short pulses tend to become more intense and more narrow. This makes that the short pulses start to break up. In some cases there is a continuous cycle of the short pulse breaking up, then a new similar short pulse emerges which in turn breaks up again, and this continues. An example of such behavior is shown in Figure 2.3.10 over a 10 ns span. The pattern repeats itself every 2.55 ns (450 MHz). The envelope of the time series is not a single frequency oscillation [24], thus this regime is a quasi periodic dynamic state with high dimension (> 3). The evolution of the pulse break up and subsequent emerging of another pulse from the tail of the initial pulse during the 2.55 ns period is shown in Figure 2.3.11. After 35 roundtrips there are two pulses that follow each other. The new pulse takes over from the initial one at a different relative position in the cavity and the phenomenon repeats itself.

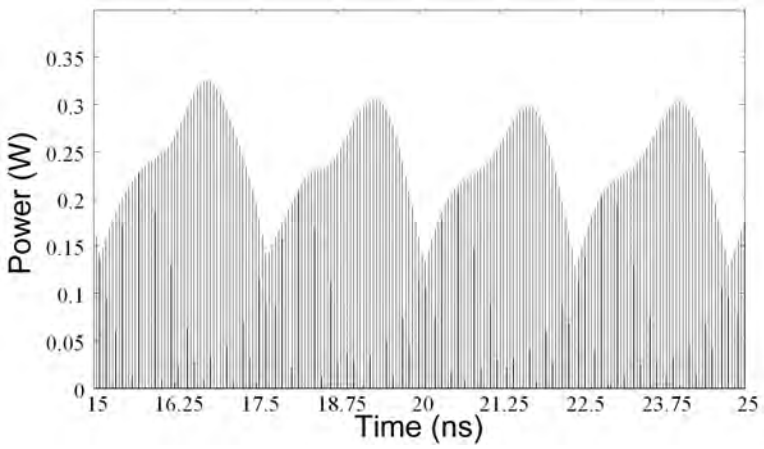

Figure 2.3.10 Simulated output power of the 20 GHz symmetric RMLL as a function of time at higher current values. Two low power 2ps pulses with a phase null were injected in both direction of the cavity to speed up the start of the laser. I = 80mA τ_{SA} = 7ps.

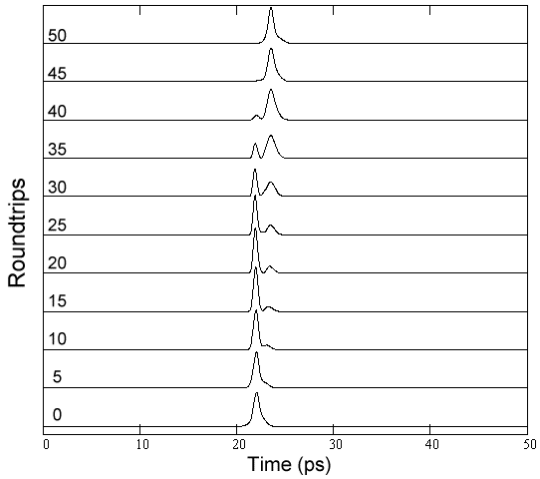

Figure 2.3.11 Pulse break-up evolution. The pulse shape in shown for a series of roundtrips. I = 80mA τ_{SA} = 7ps.

The unstable region at the top of Figure 2.3.4 where the SA carrier lifetime is 15 ps and the current lies between 64 and 68 mA, can be explained. At such SA carrier lifetime, the absorption is not always sufficiently high to prevent a second pulses to build up. A 2nd gain appears after the first pulse due to the relatively slow absorber recovery with respect to the roundtrip-time. This makes the regime unstable (see

Figure 2.3.12). For the same carrier lifetime, at around 62 mA in the amplifier, the gain is not sufficient to supply a second pulse, thus it is stable. At 65 mA there is sufficient gain to have a small second pulse in the tail of the first pulse which makes the laser unstable. Above 70 mA, the two counter propagating pulses in the cavity are more intense and deplete the gain in the amplifier more deeply. Therefore no other pulses can build up.

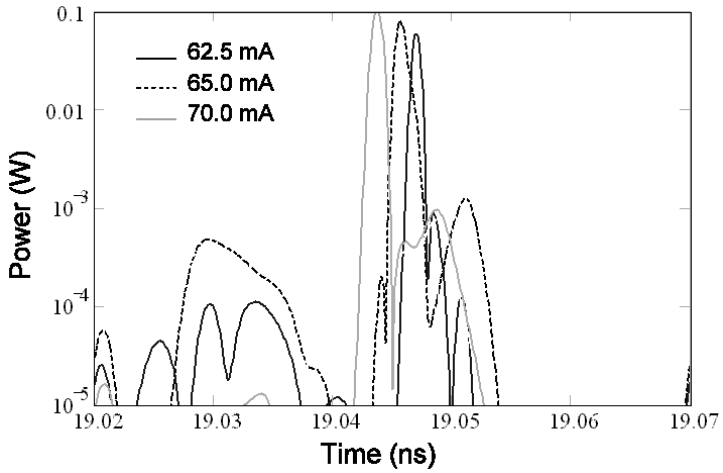

Figure 2.3.12 Simulated output power of the 20 GHz symmetric RMLL in dB scale as function of time for one selected roundtrip, τ_{SA} = 15ps. Depicted are the results for 3 different amplifier currents.

2.3.3 Simulation of an asymmetric RMLL

The next laser design studied, is asymmetric for the two counter-propagating pulses, is plotted in Figure 2.3.13. When two counter-propagating pulses are in the cavity, they meet in the SA and in the passive waveguide at the right-hand side of the coupler. The CCW pulse enters the SOA which has just been depleted by the CW pulse. Such a design is intended to investigate the possibility of having an integrated RMLL operating in a unidirectional regime since there is a roundtrip gain difference expected for the pulses in the two directions. It is of interest to achieve unidirectional operation without the use of an optical isolator which is not available for integration at the moment. The SA is positioned at the side of the amplifier. A 16 μm long (8 segments) section isolates the SA from the amplifier. The length of the SA is the same as the symmetric device studied in Section 2.3.2: 22 μm (11 segments).The simulation results show that depending on the driving conditions of the RMLL, the laser can have two counter-propagating pulses with different intensities or operates in a near-unidirectional regime.

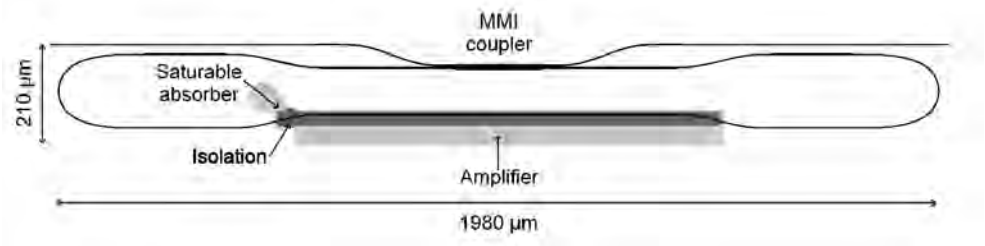

Figure 2.3.13 Design of an asymmetric 20 GHz modelocked ring laser on an active-passive wafer. The active region is 1000 µm long, at the side is a 22 µm long SA. The single isolation section is 16 µm long.

As mentioned in Section 2.3.2, it is possible to simulate the self-starting of the laser. The result of the two simulated output powers of the laser as a function of time is plotted in Figure 2.3.14. Here the time axis has been shifted for one of the output signals such that when two pulses in the two plotted output channels coincide, the two pulses traveling inside the laser cavity overlap in the SA. In this example, the RMLL supports two counter-propagating pulses in the cavity. The long time scale modulation of the CW and CCW output powers is similar to the one in the symmetric case that has been presented in Figure 2.3.3. However in the asymmetric case the building up of the pulses is different. First, it can be seen that the CW output power is more powerful than the CCW one. Then, the CW pulse builds-up in the same way as the pulses in the symmetric design, but not the CCW pulse. The initial "coarse" CCW pulse is not synchronized in the SA with the CW pulse. As the CW pulse is more powerful, it suppresses the CCW pulse, but a second CCW pulse builds-up that overlaps with the CW pulse in the SA. At the end, the laser has two counter-propagating pulses with different intensities.

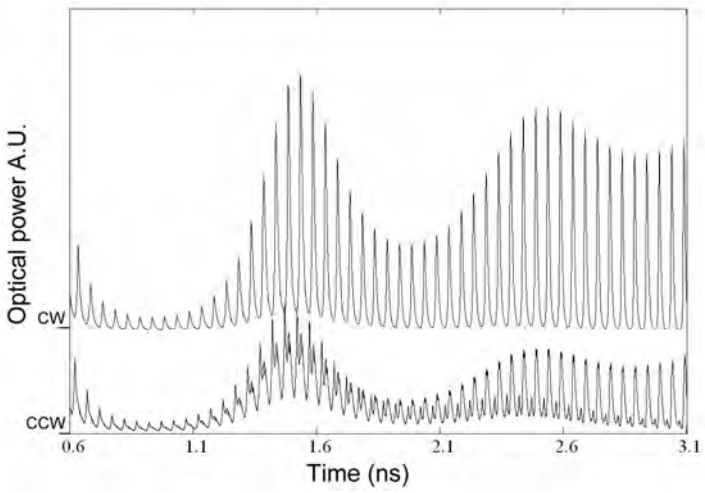

Figure 2.3.14 Simulated output power (CW and CCW) of the laser as a function of time. The time reference is the SA. In the CCW direction a pulse builds-up that is synchronized to the CW pulse, both pulses meet in the SA. (I = 65 mA τ_{SA} = 11 ps)

Simulations of the asymmetric RMLL have been performed for different amplifier current values and SA carrier lifetimes. As with the calculations on the symmetric design, in order to save computer time, two 2 ps pulses with a null phase have been injected into the cavity to start the laser. Pulses have the same intensity and are synchronized to meet in the SA. For this design, the lasing threshold is 55 mA. The first general observation is that, this configuration is much less stable than the symmetric design. The instability originates directly from the competition between the CW and the CCW modes. It is suspected that there is also a numerical stability issue in the model for calculations over periode longer than 5 ns. Part of the instability observed in the laser simulation can be attributed to the numerical discretization of the signals which is turns out to be more critical with different counter-propagating pulses. In particular the saturable absorber might require more than the 11 segments currently used. Amplifier current and SA carrier lifetime settings that gave rise to states which showed stable behavior over 5 ns have been analyzed further. These operating points are presented in Figure 2.3.15. For operating points where two counter-propagating pulses are supported, the ratio in peak power and the pulse widths for the two directions are indicated.

Different modes of operation can clearly be seen. Like the symmetric device simulated in Section 2.3.2, the pulse widths of the counter-propagating pulses increase with the current in the amplifier and decrease with τ_{SA}. The chirp of the pulses stays limited due to the integrated extended cavity. At high current injection (> 70mA) and all simulated carrier lifetime values the laser is in a Q-switching regime (non linear

dynamics of high dimension), just as the symmetric device. For a relatively short SA carrier lifetime (< 9 ps) and a current in the amplifier which is not too high (<65 mA), the laser produces short pulses modulated in intensity. The modulation depth of the envelope is indicated as a percentage in Figure 2.3.15. This modulation increases at higher amplifier current and at lower SA carrier lifetime.

SA Carrier lifetime (ps)	Amplifier current (mA)								
	57.5	60	62.5	65	67.5	70	72.5	75
17		5 ns CW CCW 1 0.15 1.3ps 1.1ps	*Unstable*	8 ns CW CCW 1 1 1.2ps 1.2ps	5 ns CW CCW 1 1 1.5ps 1.5ps	Q-Switching	Q-Switching	Q-Switching
15		*Unstable*	11 ns CW CCW 1 1 1.1ps 1.1ps	8 ns CW CCW 1 1 1.4ps 1.2ps	4 ns CW CCW 1 0.8 1.5ps 1.2ps	10 ns CW CCW 1 0.7 1.7ps 1.3ps	Q-Switching	Q-Switching
13		10 ns CW CCW 1 1 ? ?	10 ns CW CCW 1 0.8 1.1ps 0.85ps	*Unstable*	*Unstable*	*Unstable*	Q-Switching	Q-Switching
11		7 ns CW CCW 1 0.2 1.1ps 0.75ps	12 ns CW CCW 1 0.25 1.2ps 0.75ps	*Unstable*	14 ns CW CCW 1 0.3 1.5ps 1.1ps	Q-Switching	Q-Switching	Q-Switching
9		6 ns CW no Mod ?	11 ns CW 20% Mod 1.2ps	Q-Switching T=1.8ns	10 ns CW CCW 1 1 1.5ps ?	Q-Switching	Q-Switching	Q-Switching
7	*Unstable*	11 ns CW 15% Mod 0.95ps	11 ns CW 30% Mod 0.95ps	8 ns CW 40% Mod ?	Q-Switching	Q-Switching	Q-Switching	Q-Switching
5	*Unstable*	7 ns CW 50% Mod 1.0ps	*Unstable*	10 ns CW CCW 1 0.8 1.0ps 0.8ps	11 ns CW CCW 1 0.7 1.2ps 0.9ps	10 ns CW CCW 1 0.7 1.0ps 0.9ps	Q-Switching T=2.6ns	Q-Switching T=2.6ns

Figure 2.3.15 Different regimes of the asymmetric 20 GHz RMLL as function of amplifier current and SA carrier lifetime. If the laser is modelocked the ratio between the CW and CCW pulses is mentioned with the pulses width.

The most stable states are indicated as the light grey areas in Figure 2.3.15. From the location of these areas the conclusion can be drawn that the SA carrier lifetime (τ_{SA}) is the most important parameter to control the asymmetry between the CW and CCW output pulses.

At low τ_{SA} (<9 ps) the laser operates in a near-unidirectional regime as shown in Figure 2.3.16. The resulting pulses are plotted in Figure 2.3.17 for I = 60 mA τ_{SA} = 8 ps. The CW pulse has a peak power of 95 mW and a width of 0.95 ps. The down chirp is 60 GHz, but with a plateau near the maximum intensity. The CCW pulse has less than 5% of the energy of the CW pulse.

For 9 ps < τ_{SA} < 13 ps, two pulses with different intensities and pulse widths can be supported by the laser. Examples of counter-propagating pulses are plotted in Figure 2.3.18 for I = 67.5 mA and τ_{SA} = 11 ps. The CW pulse is more intense and

wider than the CCW one. The CW pulse has a peak power of 120 mW and a width of 1.45 ps when the CW pulse has a peak power of 45 mW and a width of 0.95 ps.

For τ_{SA} > 13 ps the two counter-propagating pulses can have almost the same peak power but the CCW pulse width is slightly narrower. The energy balance between the CW and the CCW regimes is not really constant. A modulation with a period larger than 4 ns is commonly observed from the simulation.

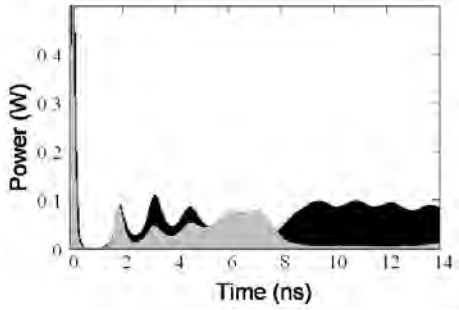

Figure 2.3.16 Simulated output power of the asymmetric 20 GHz RMLL as a function of time. After 8 ns, the laser is quasi unidirectional (CW). I = 60 mA τ_{SA} = 8 ps.

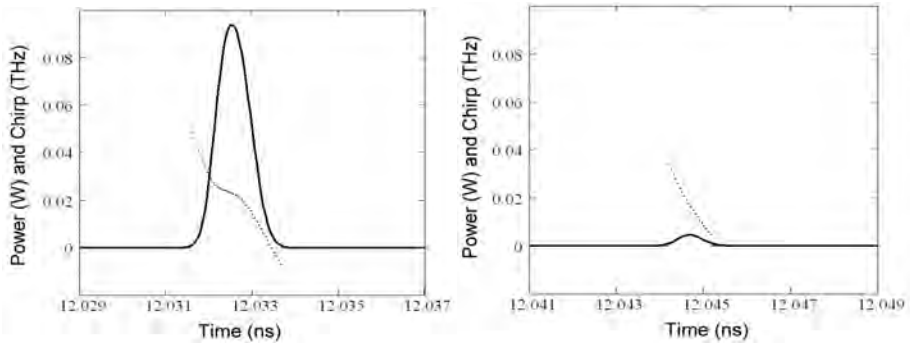

Figure 2.3.17 Simulated CW and CCW output pulses of the asymmetric 20 GHz RMLL when the laser is quasi unidirectional. I = 60 mA τ_{SA} = 8 ps.
CW: Peak power = 95mW, width = 0.95 ps, down chirp = 60GHz (nonlinear)
CCW: Peak power = 6 mW, width = 0.75 ps, down chirp = 30GHz (nearly linear)

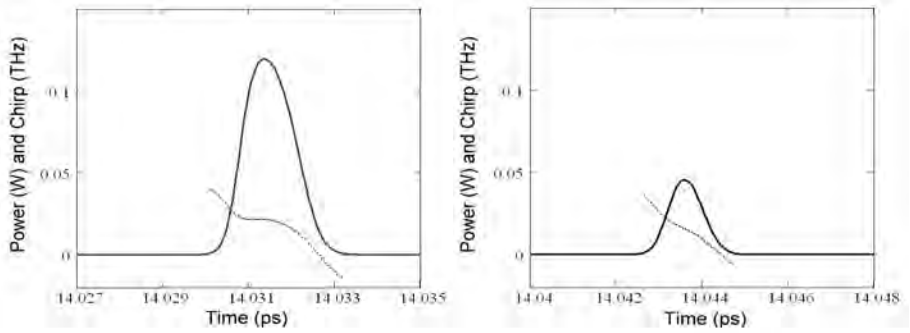

Figure 2.3.18 Simulated CW and CCW output pulses of the asymmetric 20 GHz RMLL I = 67.5 mA τ_{SA} = 11 ps.
CW: Peak power = 120mW, width = 1.45 ps, down chirp = 50GHz (nonlinear)
CCW: Peak power = 45 mW, width = 0.95 ps, down chirp = 50GHz (nearly linear)

A regime which was not perfectly stable in the symmetric regime is however more stable in the asymmetric case. The region is indicated in dark grey areas in Figure 2.3.15, it is for τ_{SA} = 5 ps and 65 mA < I < 70 mA. At the same settings, the symmetric laser produces pulses heavily modulated in intensity. The asymmetric simulations show pulses of different intensities and pulses width with a modulation in peak power <15%. The CW and CCW time series over 14 ns are shown in Figure 2.3.19. The CW and CCW pulses are plotted in Figure 2.3.20. The CW pulse has a peak power of 115 mW and a width of 1.35 ps and the CW pulse has a peak power of 65 mW and a width of 0.8 ps.

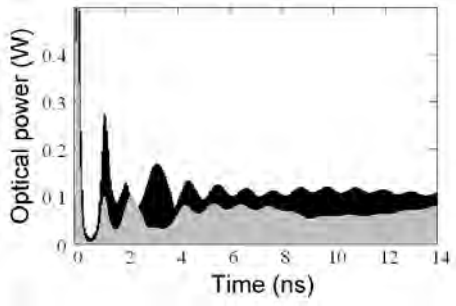

Figure 2.3.19 Simulated output power of the asymmetric 20 GHz RMLL as a function of time. I = 67.5 mA τ_{SA} = 5 ps.

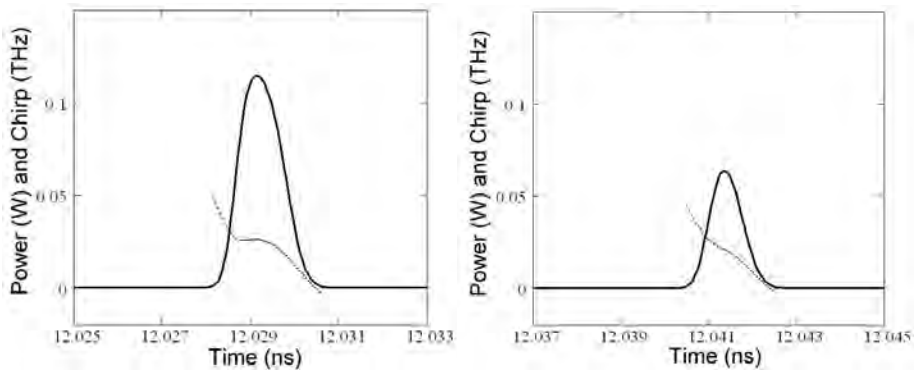

Figure 2.3.20 Simulated CW and CCW output pulses of the asymmetric 20 GHz RMLL when the laser support two pulses for I = 67.5 mA τ_{SA} = 5 ps.
CW: Peak power = 120mW, width = 1.35 ps, down chirp = 50GHz (nonlinear)
CCW: Peak power = 45 mW, width = 0.8 ps, down chirp = 50GHz (nearly linear)

A second asymmetric design has been studied. It is plotted in Figure 2.3.21. Two active regions are used: a long one for the amplifier which is 1000 μm long (2000 segments) and a short one for the SA 26 μm (13 segments). No isolation section is needed. This configuration is very similar to the previous one mentioned. Indeed, the counter-propagating pulses meet in the SA which is now "far" from the amplifier. Consequently the pulses then also meet at the right-hand side of the amplifier, just as in the design presented previously. The CCW has depleted the amplifier just before the CW pulse enters. Also here it was found that the SA carrier lifetime controls the asymmetry between the CW and CCW output pulses. The pulse widths (CW and CCW) increase with the current in the amplifier and decrease with τ_{SA}.

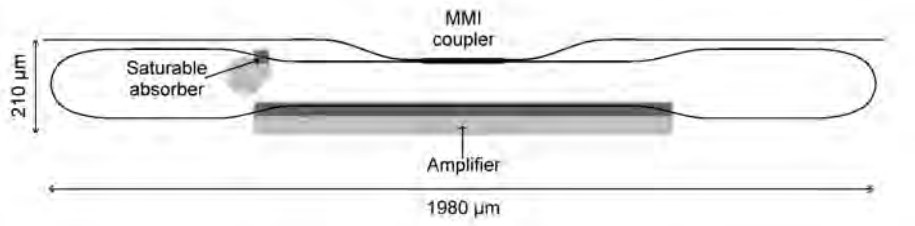

Figure 2.3.21 Design of a symmetric 20 GHz modelocked ring laser on an active passive wafer. The active region is 1000μm long the SA is 26 μm long.

2.3.4 Conclusion

A time domain bi-directional model for ring modelocked laser has been presented in the previous section. The model includes nonlinear effects and a logarithmic gain-carrier relation. The optical bandwidth of the system is controlled by a digital filter. The model has been used to simulate two types of RMLLs (symmetric and asymmetric). Simulation results show that a symmetrical cavity is better for stable modelocking. In that configuration, transitions from the modelocked state of the laser to other operating regimes have been explored with the model. The pulse width increases with the current in the amplifier and decreases with SA carrier lifetime. The 20 GHz design that was simulated contains long passive waveguides, which limits the amount of self phase modulation in the amplifiers, thus the pulses are not highly chirped. An asymmetric design has been proposed in order to investigate the possibility of having an integrated RMLL operating in a unidirectional regime. The simulation results of the asymmetric RMLL show that a modelocking regime is more difficult to achieve, however depending on the amount of absorption in the SA in the cavity, the laser can operate with two counter-propagating pulses with significantly different peak intensities.

2.4 List of references

1 Y. Barbarin, E.A.J.M Bente, T. de Vries, J.H. den Besten, P.J. van Veldhoven, M.J.H. Sander-Jochem, E.J. Smalbrugge, F.W.M.v. Otten, E.J. Geluk, M.J.R. Heck, X.J.M. Leijtens, J.G.M. van der Tol, F. Karouta, Y.S. Oei, R. Nötzel and M.K. Smit "Butt-Joint Interfaces in InP/InGaAsP waveguides with Very Low Reflectivity and Low Loss" proc. IEEE/LEOS Benelux Chapter, ISBN 2-960022645, Mons, Belgium, pp. 249-252. (2005)

2 H.A. Haus, "Theory of mode locking with a slow saturable absorber," IEEE Journal of Quantum Electronics, Vol. 11, Issue 9, pp. 736-746, (1975)

3 E.A. Avrutin, J.H. Marsh and E.L. Portnoi, "Monolithic and multi-GigaHertz mode-locked semiconductor lasers: constructions, experiments, models and applications," IEE Proc.-Optoelectronics, Vol. 147, Issue 4, pp. 251-278, (2000)

4 R.G.M.P. Koumans and R. van Roijen, "Theory for passive mode-locking in semiconductor laser structures including the effects of self-phase modulation, dispersion and pulse collisions" IEEE Journal of Quantum Electronics, Vol. 32, Issue 3, pp. 478-492, (1996)

5 J.A. Leegwater, "Theory of mode-locked semiconductor lasers" IEEE Journal of Quantum Electronics, Vol. 32, Issue 10, pp. 1782-1790, (1996)

6 S. Yu, T.F. Krauss, P.J.R. Laybourn, "Mode locking in large monolithic semiconductor ring lasers" Optical Engineering, Vol. 37, Issue 4, pp. 1164-1168, (1998)

7 Zhang L M and Carroll J E "Large-signal dynamic-model of the DFB laser" IEEE Journal of Quantum Electronics, Vol. 28, issue 3, p. 604, (1992)

8 M. Radziunas, "Numerical bifurcation analysis of the traveling wave model of multisection semiconductor lasers", Phys. D, 213 pp. 98-112. (2006)

9 U. Bandelow, M. Radziunas, A. Vladimirov, B. Hüttl, R. Kaiser, "Harmonic Mode-Locking in Monolithic Semiconductor Lasers: Theory, Simulations and Experiment", Optical and Quantum Electronics, Vol. 38, pp. 495-512, (2006)

10 M.J.R. Heck, E.A.J.M Bente, Y. Barbarin, D. Lenstra and M.K. Smit "Simulation and Design of Integrated Femtosecond Passively Mode-locked Semiconductor Ring Lasers Including Integrated Passive Pulse Shaping Components" IEEE Journal of Selected Topics in Quantum Electronics, Vol. 12, No. 2, pp 265-276, (2006)

11 J.M. Tang and K.A. Shore, "Amplification of strong picosecond optical pulses in semiconductor optical amplifiers," IEE Proc.-Optoelectronics, Vol. 146, Issue 2, pp. 45-50, (1999)

12 R. Olshansky, C. Su, J. Manning, W. Powazinik, "Measurement of radiative and nonradiative recombination rates in InGaAsP and AlGaAs light sources" IEEE Journal of Quantum Electronics, Vol 20, Issue 8, pp. 838- 854, (1984)

13 Y. Barbarin, E.A.J.M Bente, L. Mussard, G. Servanton, Y.S. Oei, R. Nötzel and M.K. Smit "Gain Measurements of Fabry-Pérot InP/InGaAsP Lasers using an Ultra High Resolution Spectrometer" Applied Optics, Vol. 45, Issue 35, pp. 9007-9012 (2006)

14 C.A. Williamson and M.J. Adams "Mode Locking of a Novel Split-Contact Semiconductor Laser - Experiment and Theory" IEEE Journal of Quantum Electronics, Vol. 40, Issue 7, pp. 858-865, (2004)

15 K.Y. Lau, J. Paslaski, "Condition for short pulse generation in ultrahigh frequencymode-locking of semiconductor lasers" IEEE Transactions Photonics Technology Letters, Vol. 3, Issue 11, pp. 974-916, (1991)

16 J. R. Karin, R. J. Helkey, D. J. Derickson, R. Nagarajan, D. S. Allin, J. E. Bowers, and R. L. Thornton, "Ultrafast dynamics in field-enhanced saturable absorbers" Applied Physics Letters, Vol. 64, Issue 6, pp. 676-678 (1994)

17 D.J. Derickson, R.J. Helkey, A. Mar, J.R. Karin, J.G. Wasserbauer and J.E. Bowers "Short Pulse Generation Using Multisegment Mode-Locked - Semconductor Lasers" IEEE Journal of Quantum Electronics, Vol. 28, Issue 10, pp. 2186-2202 (1992).

18 D. Van Thourhout, C. R. Doerr, C. H. Joyner and J. L. Pleumeekers "Observation of WDM Crosstalk in Passive Semiconductor Waveguides" IEEE Photonics Technology Letters, Vol. 13, Issue 5, pp. 457-459, (2001)

19 R. W. Hamming, "Digital Filters", Prentice Hall International (UK) Ltd., ISBN: 0-13-212812-6 (1989)

20 S Bischoff, J Mørk, T Franck, S D Brorson, M Hofmann, K Fröjdh, L Prip and M P Sørensen "Monolithic colliding pulse mode-locked semiconductor lasers" Quantum Semiclassical Optics, Journal of the European Optical Society B, Vol.9, Issue 5, pp. 655-674 (1997)

21 E.I. Jury, "Theory and application of the z-transform method", RE Krieger Pub. Co, (1973).

22 J. C. Butcher "The numerical analysis of ordinary differential equations: Runge-Kutta and general linear methods" ISBN:0-471-91046-5, Wiley-Interscience, New York, USA, (1987)

23 E.A.J.M Bente and M.K. Smit, "Ultrafast InP optical integrated circuits", Proc. Photonics West 2006, Integrated Optoelectronic Devices, 21-26 January 2006, San Jose, California, Vol. 6124, (2006)

24 Edward Ott, "Chaos in dynamical systems" Cambridge Univ. Press, ISBN: 0521811961, (1993)

Chapter 3
Fabrication technology and material characterization

3.1 Introduction

In this chapter, the fabrication technology and the material used to realize the modelocked lasers (MLL) are presented. The objective in this project is to realize MLLs using active-passive integration technology. Using the active-passive integration technology many different type of devices can be fabricated and integrated on a single chip [1]. The two principal categories of components are those using passive waveguides and those using Semiconductor Optical Amplifiers (SOAs). The integration technique is a so-called "butt-joint coupling" technique in which the index guiding structure for the passive and active components, is at the same height on the chip. The quality of the transition between the active and the passive waveguide structure, the butt-joint, is essential for modelocked lasers. This will be explained in Chapter 5. Therefore special efforts have been made to characterize the optical losses and reflections at the butt-joint and to minimize them. SOA characteristics such as the gain and the transparency carrier density have been characterized in order to be able to design and simulate modelocked lasers. The butt-joint coupling technique for active-passive integration has been chosen at the institute since it offers maximum flexibility for the design, i.e. layer composition, layer thicknesses and doping concentrations. This allows, for instance, to re-grow a passive film without doping in the index guiding layers. Therefore much lower losses in passive waveguides can be achieved than by using Quantum Well Intermixing (QWI) [2], Selective Area Growth (SAG) [3] or multiple vertical waveguide structure technique using evanescent field coupling [4].With this last technique mentioned, large coupling lengths (several hundred microns) are required which makes that devices will be larger than with the other techniques. Two types of passive waveguides can be fabricated on the chip. The

waveguides can have either a low horizontal index contrast or a high horizontal index contrast. The low index contrast waveguides are used for low loss (1 to 2 dB/cm) waveguides but these can only be used for bends with large radii (> 500 μm). High index contrast waveguides have higher propagation losses (2 to 4 dB/cm) but can be used for curved waveguides with small radii (<100 μm). The higher loss is often offset by the reduction in length that can be achieved and it leads to more compact devices (see Chapter 4). In the MLL realized with active-passive integration the two types of passive waveguides are used to obtain a short ring cavity to achieve repetition rates of over 20 GHz.

The layerstack in the active/passive integration technology used is such that an electrical contact can be placed on a passive waveguide to create an electro-optic phase shifter. Thus other components such as an electro-optic Mach-Zehnder interferometer switch or a fast tunable arrayed waveguide grating (AWG) can be combined with the MLL. Although this is not discussed further in this thesis, the MLL designs can e.g. be extended by the insertion of passive phase tuning sections in the laser cavity [5]. In principle the active-passive platform of COBRA can also integrate polarization components [6] and spot-size converters [7] but it requires others fabrication steps which are not presented in this thesis.

In the following section (3.2) the fabrication of an active-passive wafer and the complete processing of a chip are described. It will be presented that the butt-joint coupling design used gives rise to small reflections (~-40 dB) at the interface. Those small reflections are an issue for modelocked lasers and needed to be reduced. In Section 3.3 a method to characterize the butt-joint reflections [8] is presented. The method is based on the analysis of sub-threshold Amplified Spontaneous Emission (ASE) spectrum. The small reflections at the intra-cavity active-passive interfaces modify the spectrum of the modes in the sub-threshold output of the laser. By fitting the calculated sub-threshold mode structure to the recorded data, values of the reflectivities are extracted. It will be shown experimentally that those butt-joint reflections can be below -50 dB by crossing the interface with a waveguide under an angle [9]. A reflectivity of -50 dB is a minimum value required for good laser operation [10].The work presented in Section 3.3 has been published in [8] and [9]. In Section 3.4, the main characteristics of the SOA for CW amplification have been extracted to be used in our simulation model described in Chapter 2. The gain of the SOA has been measured accurately using an ultra high resolution (20 MHz) Optical Spectrometer Analyzer (OSA). The net gain curves obtained demonstrate the necessity of using the logarithmic relation between gain and carriers [11]. The differential gain parameter in the gain relation has been determined using measured transparency carrier density values for each wavelength and different temperature. Section (3.4) is founded on the results published in [12].

3.2 Active-Passive wafer fabrication and complete chip processing.

3.2.1 Fabrication of active-passive wafers

Two extensive studies of the integration on the same wafer of optical amplifiers, passive waveguide devices and electro-optic phase modulators are available in the thesis of Ronald Broeke [13, Chapter 4] for devices on an n-type InP substrate and in the thesis of Jan Hendrik den Besten [14, Chapter 3] for devices on a semi-insulating substrate. They have discussed the choice of the layerstack for each type of substrate as well as the decisions regarding trade-offs that have to be made in the integration process for the InGaAsP/InP material system. In all devices presented in this thesis n-type substrate material was used. Devices have been realized in all-active as well as active-passive material, including the first devices using active-passive material fabricated at COBRA. In this section the fabrication of active-passive wafers fully realized at COBRA is presented.

The semiconductor layers are grown by Metal-Organic Vapor Phase Epitaxy (MOVPE) with all metal-organic precursors. The fabrication of an active-passive wafer requires three epitaxial growth steps and an etching step (Figure 3.2.1). In the first epitaxy step, the layers of the active layer stack are grown up to the first doped 200 nm thick InP layer (Figure 3.2.1.a). Mesa blocks are then defined by photolithography using a 100 nm SiNx layer as etching mask. The latest mask designed of active blocks is shown in Figure 3.2.2. The mesa blocks (stripes) are 30 μm wide and the centers of the blocks are separated by 250 μm. Block lengths vary from 20 to 2000 μm and can be used to produce amplifiers, detectors or absorbers. The areas that are to be regrown with a passive layer structure are etched wet chemically down to 30 nm below the active layer, thus 530 nm is etched (Figure 3.2.1.b). Then undoped $\lambda = 1250$ nm InGaAsP and InP layers are regrown by selective area regrowth in the MOVPE using the same SiNx mask (Figure 3.2.1.c). An overhang below the SiNx mask prevents the lateral overgrowth at the butt-joint. A SEM picture of the overhang is shown in Figure 3.2.3. The thicknesses of both regrowth layers are matched to the original thicknesses at the butt-joint. Then the SiNx mask is removed and finally a p-doped top cladding layer and contacting layer are grown as shown in figure 1d. The quality achieved can be directly seen from the SEM picture depicted in Figure 3.2.4.

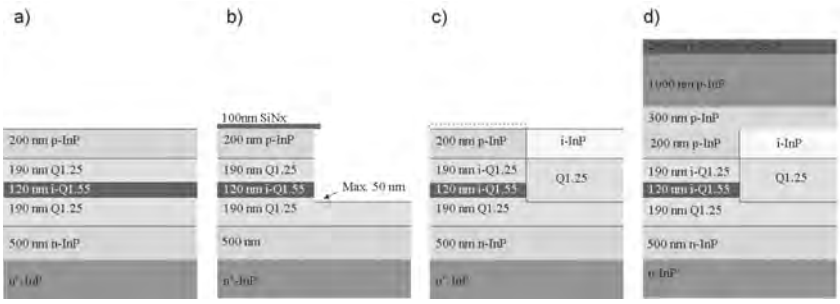

Figure 3.2.1 Process flow of the fabrication of the active-passive wafer

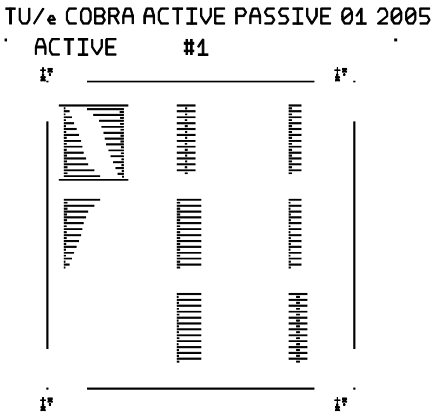

Figure 3.2.2 Mask of the active blocks of active-passive wafers. The width of the blocks is 30μm and their lengths vary from 20 to 2000 μm. The centers of the blocks are separated by 250 μm.

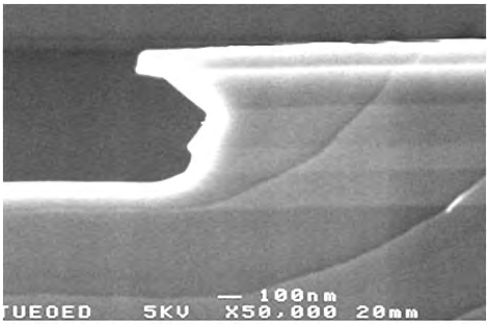

Figure 3.2.3 SEM picture of the overhang created after the wet etch in order to limit the overgrowth.

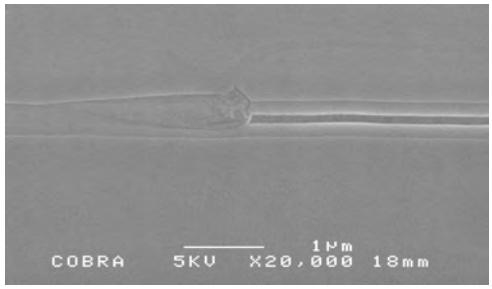

Figure 3.2.4 SEM picture of an active-passive but-joint after a stain etch to obtain contrast between the different materials. The sample is cleaved near the edge of the quarter wafer, better butt-joints are expected near the centre of the chip .

3.2.2 Complete chip processing

In this section, the complete processing of an active-passive chip is presented. The chip has up to 6 types of waveguides. Five types are shown in Figure 3.2.5 and Figure 3.2.6; from left to right: shallowly etched SOA, shallowly etched isolation between SOA, shallowly etched phase shifter, shallowly etched passive waveguide, and high contrast deeply etched waveguide. The phase shifter is a contacted shallowly etched passive waveguide [13,14]. For the isolation of phase shifters, the top cladding of passive waveguides is removed in the same way as the isolation of SOAs, which creates the sixth type of waveguide. The InGaAs layer from the passive waveguides is removed to reduce the losses [13,14].

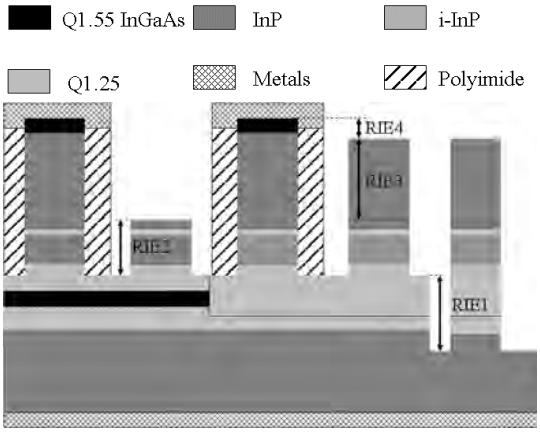

Figure 3.2.5 Sketch of the 5 types of waveguides after fabrication on an active-passive wafer. From left to right: shallowly etched SOA, shallowly etched isolation between SOA, shallowly etched phase shifter, shallowly etched passive waveguide, and high contrast deeply etched waveguide. The fabrication requires four RIE steps as indicated.

The full processing requires four masks. The different steps are shown in 12 steps (Figure 3.2.6) and are the following:

a) Deposition of a 70 nm SiNx layer using PECVD and definition of a masking for all the waveguides. A layer of positive photoresist (HPR-504) is spun on top of the SiNx layer, thus the waveguide layout can be defined in the photoresist by photolithography using the first mask. The patterns are transferred to the SiNx by dry etching the SiNx in a CHF_3 RIE process.
b) The deep areas are defined by photolithography (2nd mask) with thin negative photoresist (MaN 415). A 100 nm of Ti is evaporated. The shallow regions are covered by the Ti layer only and the deep areas are also protected by the negative photoresist under the Ti. The Ti layer on top of the photoresist is removed from the deep areas by lift-off process.
c) The deeply etched waveguides are partly etched in the RIE (***RIE1***), using an optimized CH_4/H_2 process alternated by an O_2-descum process. The etch depth corresponds to the difference between shallowly and deeply etched waveguides (~600 nm).
d) The Ti mask is removed wet chemically (chemistry) after which all the waveguides are partly etched in the RIE (***RIE2***). The etch depth corresponds to the difference that is required at the end of all etching between the top of the isolation waveguides and the floor of the shallow areas (~500 nm).
e) The SiNx mask is removed from the isolation waveguides. It is removed wet chemically (HF solution) by covering the other waveguides (3rd mask) with thick negative photoresist (MaN 440).
f) All the waveguides are partly etched in the RIE (***RIE3***). The etch depth corresponds to the difference that is required at the end of all etching between the top of the passive waveguides and the top of the isolating waveguides. (~1000 nm)
g) The SiNx mask is removed from the passive waveguides. It is removed wet chemically (HF solution) using the mask for the metallization. It does not cover the isolation waveguide but it is not a problem.
h) All the waveguides are etched in a final step in the RIE (***RIE4***). The etch depth corresponds to the thickness of the contact layer plus a margin (~200 nm). If all the etch steps went as set, the shallow waveguide etch is 100nm into the film and the deeply etched waveguide etch is 100 below the film.
i) The chip is planarized by spinning 5 layers of polyimide which is cured up to 325°C.
j) The polyimide is etched back in a controlled CHF_3/O_2 process until the contacts are open.
k) The metal pads are defined by photolithography using thick negative resist. 20 nm of the contact layer is etched (with 10 times diluted Q-etch) in order to clean the surface. A first metallization is performed by evaporation and lift-

off (Ti 60 nm / Pt 80 nm /Au 400 nm). In order to have a better current distribution along SOAs a second metallization by evaporation with only gold (500 nm) is applied.

l) The backside metallization is done by evaporation. (Ti 60 nm / Pt 80 nm / Au 400 nm). The chip is then annealed at 325°C for 25 s twice (top side and bottom side) and finally cleaved. Some designs require HR or AR coating which is done by a commercial contractor.

The final result of the fabrication of a shallowly etched SOA, a shallowly etched passive waveguide, and a high contrast deeply etched waveguide can be seen on the SEM pictures of Figure 3.2.7.

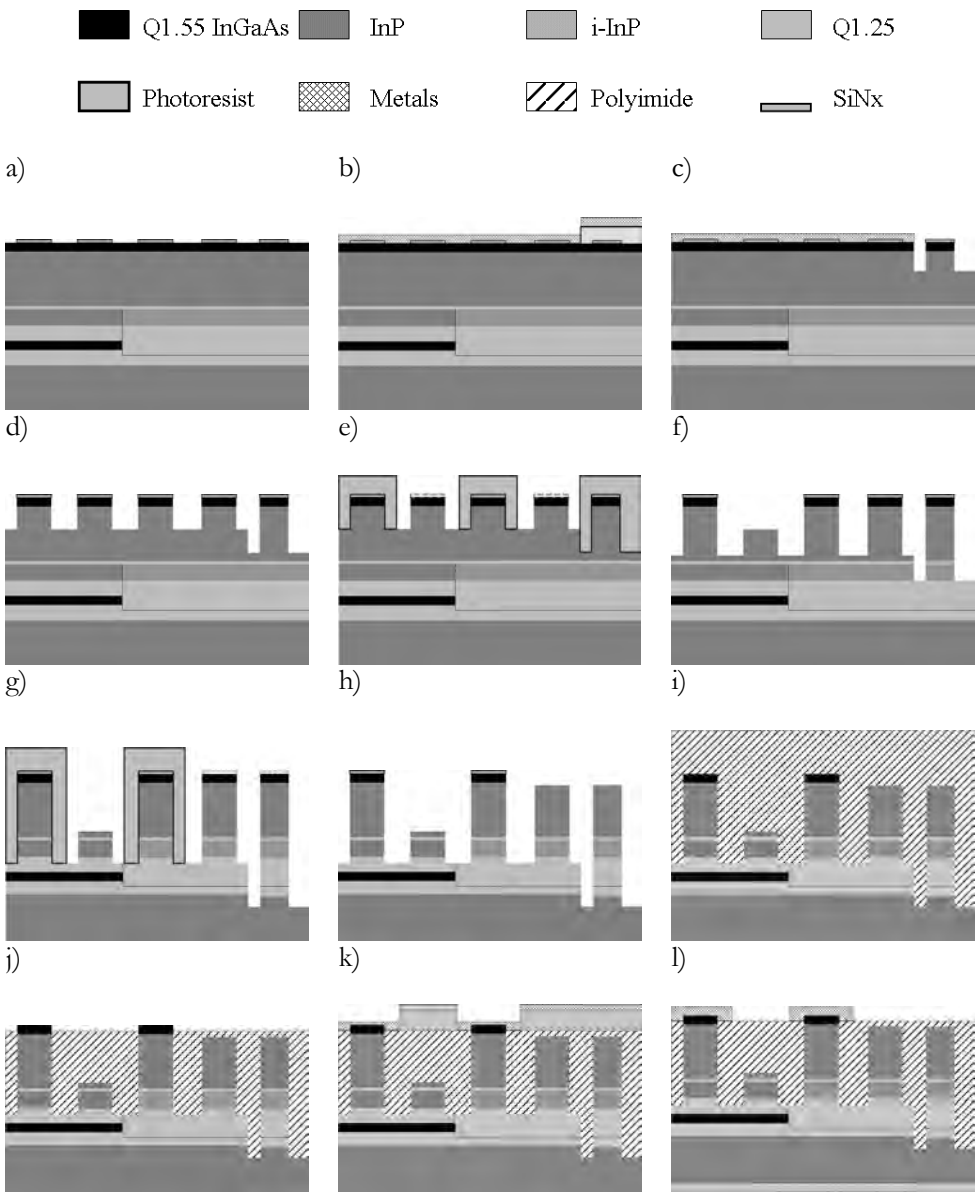

Figure 3.2.6 Illustration of the process steps in the fabrication of active-passive chips on n-type substrate.

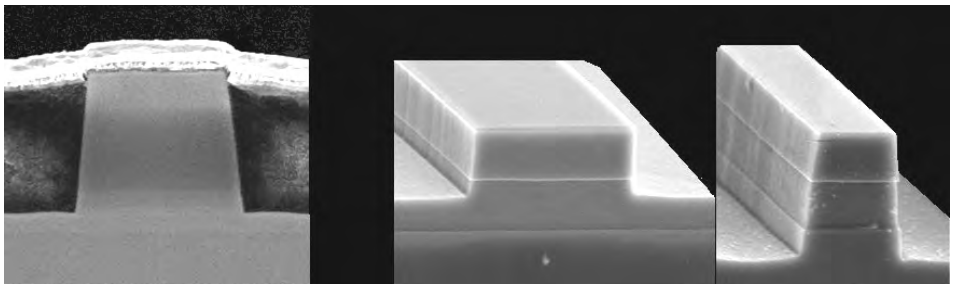

Figure 3.2.7 SEM pictures of a shallowly etched SOA (cross section), a shallowly etched passive waveguide (after a stain etch), and a high contrast deeply etched waveguide (after a stain etch).

The process scheme of has been developed for the realization of the devices presented in Chapter 6. The chips presented in this thesis are of different types: double-etch passive chip, double-etch all-active chip and double-etch active-passive chip with phase shifters. As explained in details below, the different chips do not always requires all the steps presented in Figure 3.2.6 or have been fabricated with an older process scheme.

The double-etch passive Arrayed Waveguide Grating (AWG) presented in Section 4.2 does not require any isolation and metallization. The fabrication of that chip stops at step d) and the last etching step corresponds to the depth of the shallowly etch waveguide. Furthermore for the fabrication of the AWG, the masking of the shallow areas (step b) was with positive photoresist. Masking with Ti has been introduced in our technology scheme afterwards to reduce waveguide sidewall roughness of the deeply etched waveguides.

The all-active chips that are presented in Sections 4.3, 5.2 and 5.3 have been fabricated following a similar process scheme than the one presented in Figure 3.2.6. However, as there is no passive waveguide, the step g) is skipped (this step is the contact removal of the passive waveguide). Since the all-active chips have deeply and shallowly etched SOA's, the second masking (step b) is necessary. A picture of a complete all-active chip realized is shown in Figure 3.2.8.a.

The modelocked ring laser presented in Section 5.5 was on an active-passive chip with many other devices and using wafer material fabricated at JDSU. The picture of the complete realized chip is shown in Figure 3.2.8.b. The chip has been processed using an older processing scheme. The masking of the shallow areas (step b) was with positive photoresist and the metallization was not self-aligned. The metallization was done, by first passivating the chip with a 350 nm SiNx layer, then opening the contacts with a special mask and finally sputtering the same metal layers as in step k). More details are available in [13].

a)

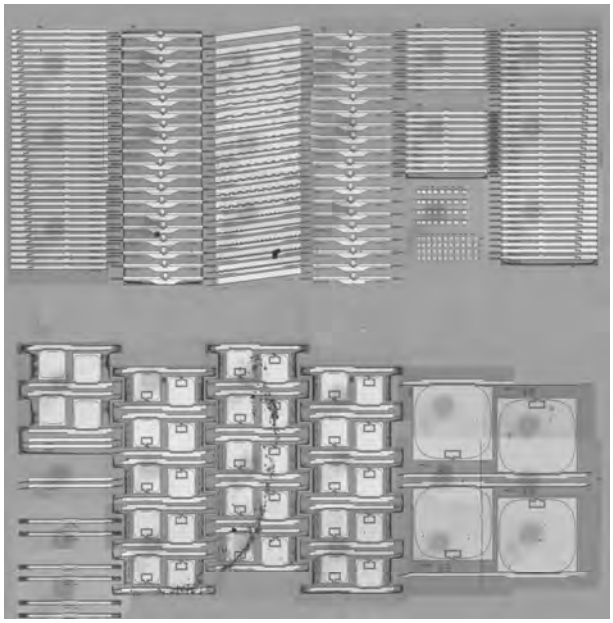

b)

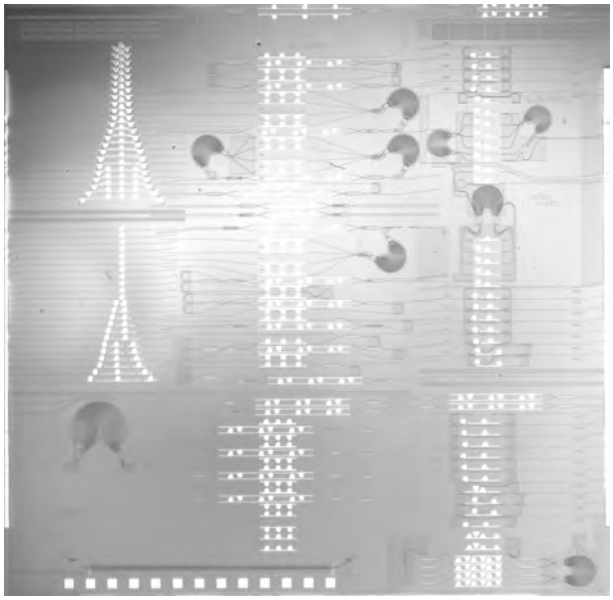

Figure 3.2.8 Photographs of an all active chip (a) and of an active passive chip (b). The shiny elements are metals contacts.

3.3 Measurement of Active-Passive butt-joint loss and reflections

3.3.1 Introduction

Low butt-joint loss and low butt-joint reflection values on active-passive interfaces are essential in Photonic Integrated Circuits (PIC). This is particularly so for lasers, where reflections down to –50 dB affect their operation [10] and lead to a modification of the structure in the output spectrum. Modelocked lasers for instance are very sensitive to any intra-cavity reflections as e.g. described in Chapter 5 and in [15]. Also, the noise properties of the output of a laser improve with lower roundtrip cavity loss [16], consequently the lowest butt-joint loss is preferable for good noise performance and efficiency. For the development of the technology, measurements of small reflectivity values on butt-joint active-passive interfaces are needed. Measurement of reflectivity based on the Hakki-Paoli method has been reported in simple two mirror cavities [17]. But in case of butt-joint reflectivity measurements inside a cavity, a full analysis of the sub-threshold optical spectrum is required. In this chapter, we present a method and measurement results of the reflectivity of butt-joint active-passive interfaces. First the method has been developed on a series of extended cavity Fabry-Pérot lasers on active-passive wafers from JDS-Uniphase [18]. Good values of –40 dB have been measured. We have obtained at the institute 0.19 dB loss per passive-passive butt-joint interface in single mode waveguides and reflection values < –50 dB at active-passive butt-joint interfaces in similar extended cavity Fabry-Pérot lasers.

3.3.2 Butt-joint loss of COBRA passive-passive wafer.

In the development of our active-passive integration technology, the loss due to the geometry and quality of the regrown material at the butt-joints was evaluated in passive-passive structures. In these tests first a passive layerstack is grown and selective areas are etched and regrown following the same process as for active-passive integration described in Section 3.2.1. A SEM picture of passive-passive butt-joint is plotted in Figure 3.3.1 after stain-etch to highlight the different material composition. The picture is taken from a sample at the edge of the chip, better butt-joint are expected for devices. Interface losses were then determined by comparing losses in: a) waveguides etched in first growth material, b) waveguides etched in regrown material and c) waveguides with butt-joints (crossing alternatively first-growth and regrown areas). The design of the test structures is plotted in Figure 3.3.2. Having determined the losses from first-growth waveguides and regrown waveguides accurately, the butt-joint loss per interface can be extracted.

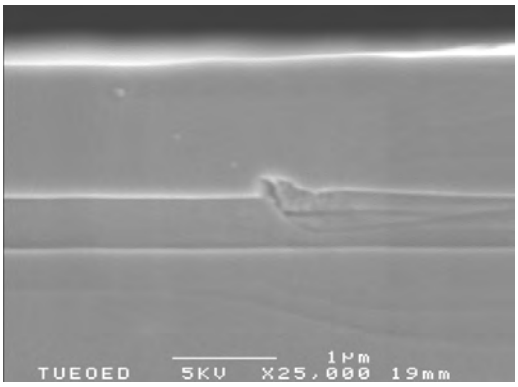

Figure 3.3.1 SEM picture of a passive-passive but-joint after stain-etch to obtain contrast between the different materials. The picture is taken at the edge of the chip, better butt-joints are expected near the centre of the chip.

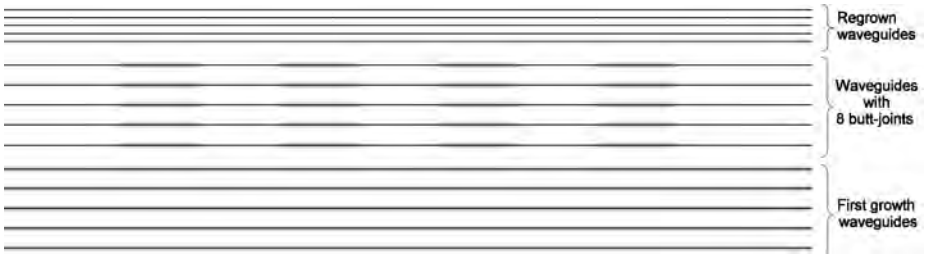

Figure 3.3.2 Structures used from the butt-joint loss measurements.

All waveguide losses were measured using the Fabry-Pérot technique [19]. The shallowly etched waveguides are 2 μm wide. 20 waveguides of each type have been measured. The average optical losses for first-growth waveguides are 2.64 dB/cm with a variation of ± 0.05 dB. The average optical losses for regrown waveguides are 2.72 dB/cm with a variation of ± 0.2dB. The increase of losses in the regrown waveguides is less than 0.1 dB. 22 waveguides each with four or eight butt-joints have been measured. The losses per interface were found to lie between 0.1 and 0.25 dB with an average value of 0.19 dB. These results show that butt-joints of high quality are obtained.

3.3.3 Butt-joint reflection measurement method

The method is based on the analysis of sub-threshold spectra of lasers with intra-cavity reflections. These spectra show a series of resonances at a regular spacing (Free Spectral Range of the total cavity). The intra-cavity reflections create a number of periodic modulations of the intensity of the resonances peaks. The modulation depth is directly related to the reflectivity of the interfaces. The frequency of a modulation is inversely proportional to the distances between the reflection points.

Both frequencies and modulation depths are easily observed in the Fourier transform of the spectrum [20]. By fitting a simulated sub-threshold spectrum to the recorded data, values of the reflectivities have been extracted.

A series of integrated Extended Cavity Lasers (ECL) has been produced. These lasers consist of a Semiconductor Optical Amplifier (SOA) waveguide connected to two passive waveguides terminated by cleaved mirrors. Each device has a different length of SOA (Figure 3.3.3). Details of the fabrication are given in [13]. The small reflections at the two intra-cavity active-passive interfaces modify the mode structure. A typical transformed spectrum is plotted in Figure 3.3.4, where the time axis has been translated into physical distance. Analyzing this graph, the highest peak corresponds to the longitudinal mode of the total cavity (3.736 mm). Other peaks belong to the intra-cavities formed by the two passive waveguides. Only cavities containing at least one cleaved facet are observed; the possible cavity formed by the SOA alone (L2) is not visible.

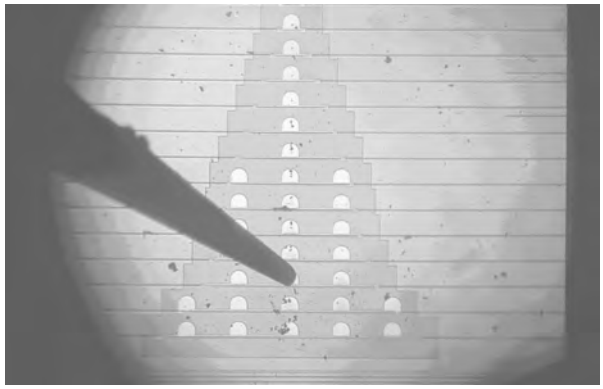

Figure 3.3.3 Picture of part of the chip with the series of extended cavity lasers. A probe is visible that supplies current to one of the SOAs.

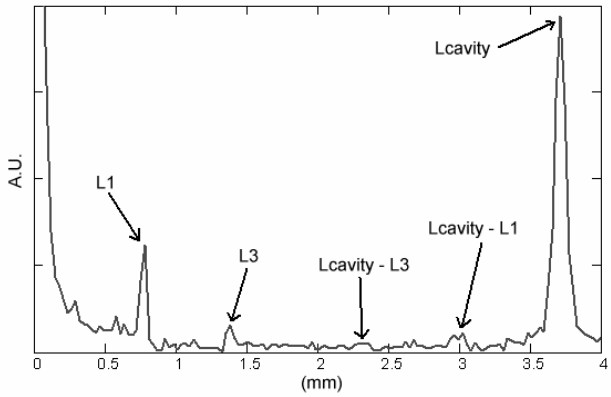

Figure 3.3.4 Fourier transform of a 12nm span ECL spectrum, Isoa = 76.5mA and Lsoa = 1500μm

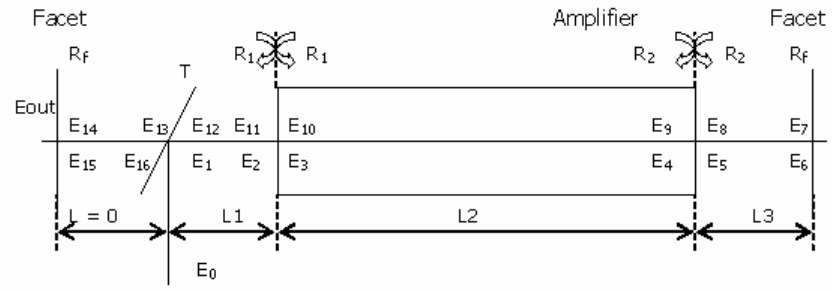

Figure 3.3.5 Schematic representation of an ECL in the model with definition of normalized fields and power reflectivity coefficients.

3.3.4 Modeling of the sub-threshold spectrum

The modeling of the sub-threshold spectrum is explained using the scheme in Figure 3.3.5. We model the generation of the ASE from the SOA by introducing a low reflectivity beam splitter ($T = 1\text{-}10^{-7}$) that couples light into the cavity from an external monochromatic source. The propagation of the field through WG 1, amplifier and WG 2 and back is calculated using a transmission matrix T_{Total}. The field E_{out} from the left cleaved facet can then be calculated for a range of wavelengths of the injected light:

$$E_{OUT} = E_0 \cdot \frac{Ttotal_{1,0} \cdot \sqrt{T} \cdot \sqrt{1-T} \cdot \sqrt{1-R_f}}{Ttotal_{0,0} - \left(Ttotal_{1,0} \cdot T \cdot \sqrt{R_f}\right)} \qquad \textbf{3.1}$$

Rf represents the power reflectivity at the cleaved mirrors (*Rf* = 0.34). The T-matrix T_{total} used is:

$$T_{Total} = T_{WG1} \cdot T_{Int\_Loss1} \cdot T_{Refl1} \cdot T_{SOA} \cdot T_{Refl2} \cdot T_{Int\_Loss2} \cdot T_{WG2} \cdot T_{Refl\_F} \qquad \textbf{3.2}$$

where T_{WG1} and T_{WG2} describe the passive waveguide sections, T_{SOA} the amplifier, T_{Int_Loss1} and T_{Int_Loss2} the interface losses, T_{Refl1} and T_{Refl2} the interface reflections and T_{Refl_F} the facet reflection.

$$T_{WG} = \begin{bmatrix} e^{Att+i\cdot\left(\frac{2\cdot\pi\cdot Ng_{WG}}{\lambda}\cdot L_{WG}\right)} & 0 \\ 0 & e^{-Att-i\cdot\left(\frac{2\cdot\pi\cdot Ng_{WG}}{\lambda}\cdot L_{WG}\right)} \end{bmatrix} \qquad \textbf{3.3}$$

$$T_{Int\_Loss}\left(Loss_{\mathbf{int}}\right) = \begin{bmatrix} e^{Loss_{\mathbf{int}}} & 0 \\ 0 & e^{-Loss_{\mathbf{int}}} \end{bmatrix} \qquad \textbf{3.4}$$

$$T_{Refl}\left(R\right) = \frac{1}{\sqrt{1-R^2}}\begin{bmatrix} 1 & -R \\ -R & 1 \end{bmatrix} \qquad \textbf{3.5}$$

$$T_{SOA} = \begin{bmatrix} e^{-G(\lambda)+i\cdot\left(\frac{2\cdot\pi\cdot Ng_{SOA}}{\lambda}\cdot L_{SOA}\right)} & 0 \\ 0 & e^{G(\lambda)-i\cdot\left(\frac{2\cdot\pi\cdot Ng_{SOA}}{\lambda}\cdot L_{SOA}\right)} \end{bmatrix} \qquad \textbf{3.6}$$

In our model the wavelength dependence of the gain in the SOA $G(\lambda)$ and the intensity of the spontaneous emission $E_0(\lambda)$ have been successfully fitted to the same Gaussian shape. *Att* is the loss in the passive waveguides. Ng_{WG} and Ng_{SOA} are the wavelength dependent group indexes. Dispersion in the different waveguides needed to be included to obtain agreement with the experiment.

$$Ng_{WG}\left(\lambda\right) = N_0^{WG} + \frac{N_1}{\lambda^2} \qquad \textbf{3.7}$$

$$Ng_{SOA}\left(\lambda\right) = N_0^{WG} + C + \frac{N_1}{\lambda^2} \qquad \textbf{3.8}$$

The dispersion is assumed to be equal for the active and passive waveguides (*N1*). The constant difference *C* between the group index of the active and passive waveguide has been measured separately by measuring the laser mode frequencies with a high resolution multi-wavelength meter (ANDO AQ6141). The optical spectrum analyzer (OSA) used for these measurements (ANDO AQ6315A) was limited in resolution. A high resolution OSA (APEX AP2041A) became available after those measurements with a 20 MHz resolution (0.16 pm) as mentioned in Section 3.3.7.

Passive losses of 4 dB/cm and a 0.2 dB butt-joint loss have been measured on passive regrown structures. The line width of the OSA has been determined using a single-mode 500 kHz line width CW laser. The line width of the OSA fitted well to a Gaussian function with a bandwidth of 0.07 nm FWHM. The effect of the finite bandwidth of the OSA is illustrated in Figure 3.3.6. Here the Fourier transforms (FT) are given of 1) a theoretical spectrum not including the effect of the OSA broadening 2) the same spectrum including the broadening and 3) the spectrum of the OSA transmission function. The intensities of the intra-cavity peaks are reduced by the instrumental broadening. The two peaks corresponding to the passive waveguides (*L1* and *L3*) are not strongly affected. However the peak for the total cavity is attenuated by a factor 5.5. The amplitude of this peak serves as the reference for the relative normalisation of the FT of the theoretical spectrum to the FT of the experimental one. This normalisation is required to obtain the reflection values from the peaks in the transformed experimental spectrum. Therefore knowledge of the exact line width of the OSA is essential.

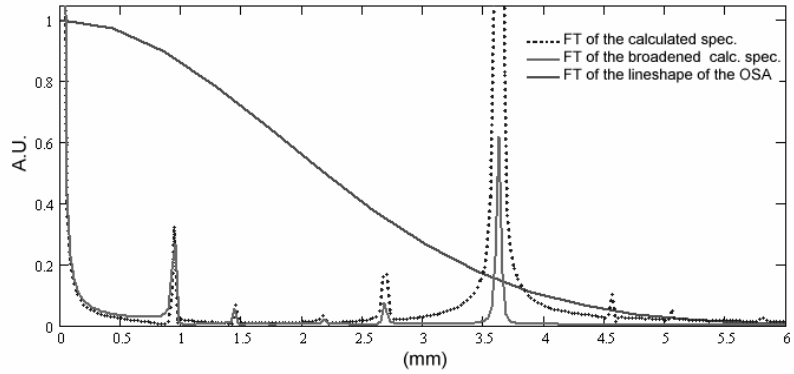

Figure 3.3.6 Effect of the finite bandwidth of the OSA on the Fourier transform of the optical spectrum.

The theoretical spectrum is fitted to the recorded data as follows. First it is broadened to simulate the finite bandwidth of the spectrum analyzer (0.07 nm). Then the coefficients of the group index are adjusted to fit the position of the modes along the spectrum. Adjusting the gain of the amplifier and its wavelength dependency reproduces the coarse shape of the spectrum. Afterwards, the reflectivity parameters are varied to optimize the agreement between the Fourier transforms of the measured and theoretical spectra. Finally the cavity lengths are fitted to the original data. This sequence is repeated at least two times.

3.3.5 Butt-joint reflectivity in ECLs on a JDSU active-passive wafer

Initial measurements and fits have been performed on a series of extended cavity Fabry-Pérot lasers with a fixed total length fabricated of active-passive wafer from JDS Uniphase. A SEM picture of a cleave through an active passive butt-joint along the (011) plane is plotted in Figure 3.3.7. The chip was soldered on a temperature controlled copper mount (20°C). Light from a laser output waveguide was collected using a lensed fiber and led to the optical spectrum analyzer (ANDO AQ6315A). The spectra were recorded over a 12 nm span which is sufficient to resolve the reflection peaks in the Fourier transformed spectrum. To illustrate the quality of the fitting of the simulation Figure 3.3.8 presents the central 2 nm part of the experimental and simulated spectra. The positions of the modes match perfectly. The modulation over the modes due to the butt-joints reflections is simulated correctly along the spectrum. The fitting has been performed for six devices and at different currents.

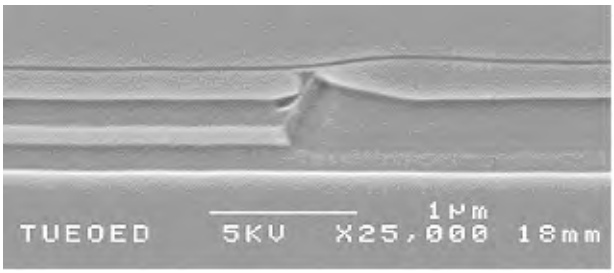

Figure 3.3.7 SEM picture of an active passive butt-joint (011) plane.

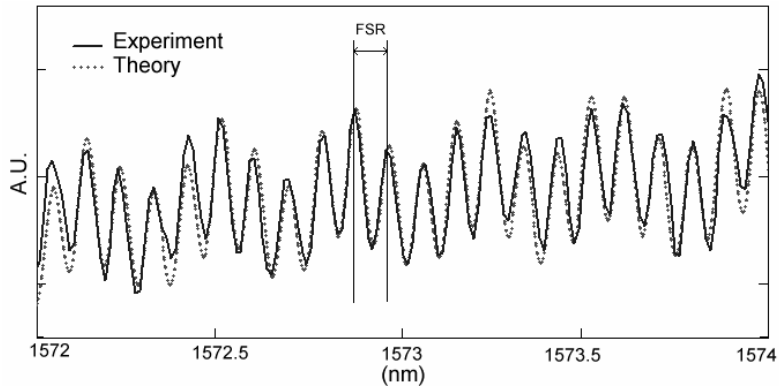

Figure 3.3.8 Central 2 nm part of a theoretical and experimental ECL sub-threshold spectrum (Lsoa = 1250µm Isoa = 70mA). The FSR for the total cavity is indicated.

An average value of -40.5dB has been determined. The results for the different devices are summarized in Table 3.3.1 for each SOA. L1 and L3 are the fitted values obtained of the two passive waveguides, L2 is the fitted value of the SOA length. Measured SOA lengths and waveguides lengths (L1 and L3) were used in the model as initial values and fitted with an accuracy of 5 nm. For each device, values for R1 and R2 have the same order of magnitude. Reflection values vary from – 47 dB to – 39 dB.

Table 3.3.1: Results of butt-joint reflectivity for the series of integrated extended cavity lasers

L_{SOA} (µm)	L_1 (µm)	L_2 (µm)	L_3 (µm)	R1 (dB)	R2 (dB)
600	1305.30	599.95	1829.01	- 47	- 41
700	1256.26	700.10	1777.64	- 43	- 39.5
900	1156.96	899.95	1677.10	- 41.5	- 45
1000	1104.83	999.99	1628.31	- 39.5	- 42
1250	980.12	1249.90	1503.90	- 39	- 41
1500	855.97	1500.00	1378.03	- 39	- 38

3.3.6 Discussion of the method

Reflectivities down to – 40.5 dB could be measured using the ANDO AQ6315A. Reflectivity values could be determined over a range of SOA currents (approximately 1-3 mA below the lasing threshold). The extracted values fell within a range of 1.10^{-5}. The determined reflectivities depend only weakly on the values used for the butt-joint loss or the waveguide losses. A ±0.05 dB change of the 0.2 dB butt-joint loss or a ±0.5 dB/cm change of the 4.0 dB/cm passive waveguide losses modifies the resulting reflectivity values by 0.1 dB. The minimum length of the laser cavity is determined by the number of modes needed in the spectrum for a reliable analysis and its total width. The maximum device length that can be used depends on the resolution of the OSA (typically 0.05 nm) in order to resolve the individual modes. Using the same equipment, spectra from similar devices with cavity lengths between 400 μm and 6 mm can be fitted. When a High Resolution OSA (HROSA) is used like the APEX AP2041A with 20 MHz resolution, these limitations are relaxed so strongly that in practice no limitations in device length are encountered.

3.3.7 Minimization of butt-joint reflectivity in ECLs on a COBRA active-passive wafer

We have redeveloped at the institute the realization of active-passive wafers and we have investigated the minimization of the butt-joint reflection in a single mode waveguide by crossing them at varying angles with the active-passive interface [9]. A SEM picture of an active-passive butt-joint is plotted in Figure 3.2.4. In these measurements the sub-threshold laser spectra are recorded with a very high resolution of 0.8 pm using the APEX AP2041A OSA. In that case, the transfer function of the OSA does not need to be taken into account. Three series of integrated ECLs have been characterized. These lasers consist of a SOA waveguide connected to one or two passive waveguides terminated by cleaved mirrors. The waveguides are 2 μm wide. We have measured 9 integrated ECLs having two butt-joints and different lengths of amplifier sections. In this series, the waveguide crosses the active region perpendicularly. The average reflection is $5.10^{-5} \pm 0.15.10^{-5}$ (– 43 dB). This value is close to the theoretical value simulated with FIMMWAVE (6.10^{-5}) and 2.5 dB lower than the value presented in paragraph 3.3.5.

Next, we investigated the minimization of the butt-joint reflectivity by crossing the interface at 6 different angles (from 5 to 15 degrees). Two designs are plotted in Figure 3.3.9: the waveguide is curved using adiabatic bends to avoid additional reflections and to cross two active-passive interfaces at 13 or 15 degrees. 24 ECLs with in total 32 butt-joints have been characterized. In Figure 3.3.10, reflectivity values are plotted versus the angle of the waveguide to the normal. An upper trend is also indicated. 90% of the measured reflectivities are below this line with a trend of 1 dB per degree. The results clearly show that the butt-joint reflectivity is below – 50 dB

for angles higher than 12 degrees. We expect even lower values which, however, we were not able to measure values below – 53 dB with our setup.

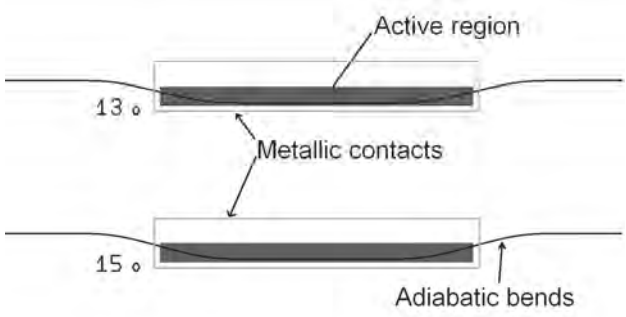

Figure 3.3.9 Design of two extended cavity lasers with crossing of the active region at different angles.

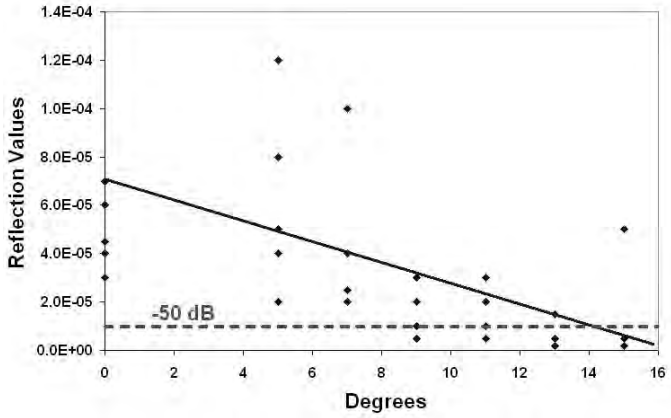

Figure 3.3.10 Results of butt-joint reflections for different angled at the crossing of the active-passive interface. An upper trend is also indicated, 90% of the measured reflections are below this line.

Figure 3.3.11 and Figure 3.3.12 depict the ASE spectra and their Fourier Transforms (experimental and fitted) of two ECLs with waveguide crossing angles of, respectively, 5 and 15 degrees. For the angle of 5 degrees, the reflection is found to be -43 dB. The spectrum shows a pronounced modulation which gives rise to a clearly identifiable peak in the FT. The FT spectra all show three small peaks (around 0.45 mm) which are present even without input signal and which originate from the high resolution spectrometer. They arise from the noise, which is visible in the spectra, and do not affect the measurements of the reflections. For the angle of 15 degrees, the reflection is found to be – 53 dB. The modulations in both the emission spectrum and

the Fourier transform have almost completely disappeared. This confirms a reflection lower than - 50 dB necessary for good laser performance discussed in [10].

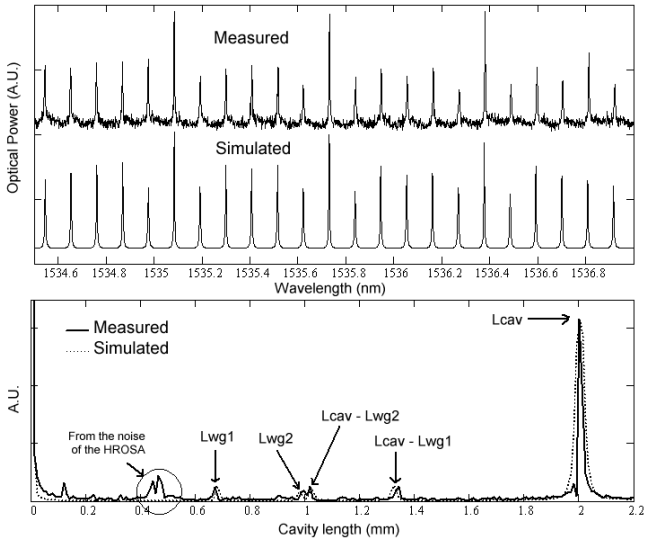

Figure 3.3.11 Sub-Threshold optical spectrum and its FT (measured and fitted) for an angle of 5° (R = - 43dB).

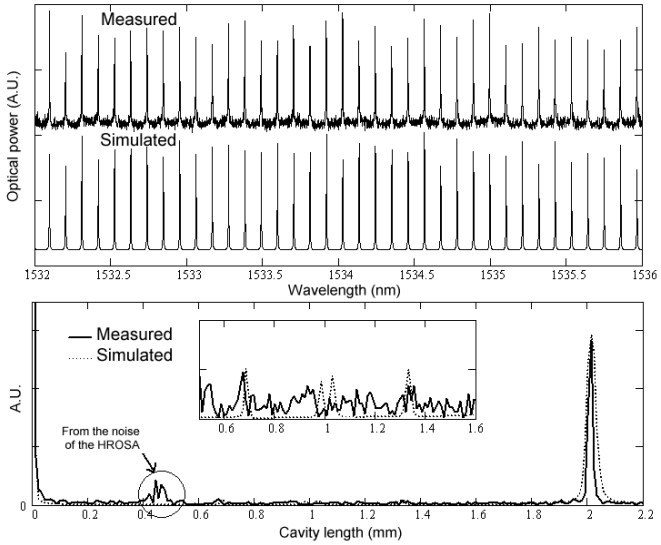

Figure 3.3.12 Sub-Threshold optical spectrum and its FT (measured and fitted) for an angle of 15° (R = - 53dB).

3.3.8 Conclusion

A method and measurement results have been presented for the determination of the reflectivity of butt-joint active-passive interfaces in a series of extended cavity Fabry-Pérot lasers. We observed reflection values < – 50 dB at active-passive butt-joint interfaces in extended cavity Fabry-Pérot lasers and 0.19 dB loss at passive-passive butt-joint interfaces. Minimization of the butt-joint reflection has been obtained by crossing the interface at different angles. For angles larger than 12 degrees, reflections lower than – 50 dB are obtained which guarantee optimum laser performance.

3.4 Gain measurements of bulk SOA

3.4.1 Introduction

In this section, the main characteristics of the bulk SOA for CW amplification have been extracted to be used in our simulation model described in Chapter 2. The advantages of using an ultra high resolution Optical Spectrum Analyzer are presented. The gain-carrier relation used has been validated and the differential gain parameter has been determined. The gain-carrier relation uses the results of the transparency carrier density values measured for each wavelength and different temperature.

The optical gain in a semiconductor laser is an essential parameter to characterize fabricated lasers and to simulate their behavior. The most commonly used method to measure the gain in laser cavities is the so called Hakki-Paoli method [21]. In this method the optical gain is derived from the contrast ratio of the modulations in the spectrum of the Amplified Stimulated Emission (ASE) caused by the resonances of the laser cavity operating below threshold. The main advantage of this method is that no external source, wideband antireflection coating of the laser facets or accurate values of the coupling efficiency are required. This intensively used method is however sensitive to noise and its results are significantly influenced by the response function of the spectrometer. Cassidy was first to improve the method by introducing a ratio between the integral of the intensity of a mode peak and the minimum intensity [22]. This makes the method less sensitive to the resolution of the Optical Spectrum Analyzer (OSA) however both methods are still sensitive to the noise. Wang and Cassidy have recently proposed and demonstrated a method using a non-linear least-squares fitting of the Fabry-Pérot equation which is less sensitive to noise [23]. By taking into account all the data points of the spectrum, it improves the accuracy as compared to previous methods. However they had to introduce a correction to take into account the resolution of the OSA. In this paper we present measurements done using an ultra high resolution OSA (20 MHz ~0.16pm). Thus the effect of the response function of the OSA does not need to be compensated. Such high resolution provides a very good accuracy in the gain measurement right up to the threshold of the laser. Also the cavity of the lasers under investigation can be longer than 1mm which is the typical limit for standard grating based OSAs. This can be an issue with devices with low gain, such as quantum dot lasers, or lasers in larger integrated circuits. The high accuracy of the method has been demonstrated and has been combined with measurements of the optical transparency point by determining the optical gain spectrum and the differential gain of an InP/InGaAsP Fabry-Pérot laser structure as a function of injected carrier density. Results for a range of heat sink temperatures around room temperature are presented. These parameters will be used in our simulation models for lasers fabricated with identical layer stacks.

3.4.2 Gain measurement method

The steady-state optical output spectrum of a Fabry-Pérot laser below threshold is described by the following Airy function equation [24].

$$I(\lambda) = B(\lambda).\frac{(1+R.G)\cdot(1-R)}{(1-R.G)^2 + 4.R.G.\sin^2\left(\frac{2\pi.Ng.L}{\lambda}\right)} \qquad \textbf{3.9}$$

Where $B(\lambda)$ is the total amount of spontaneous emission represented by an equivalent input flux, $G(\lambda)$ is the single-pass modal gain, R is the laser facet reflectivity, L is the cavity length and Ng is the group index of the waveguide. The equation is rewritten and a background level is added to obtain an equation that is to be fitted to each mode peak in the recorded subthreshold ASE spectrum (3.10). No convolution with the OSA response is necessary.

$$I_{fit}(\lambda) = \frac{C}{(1-R\cdot G)^2 + 4\cdot R\cdot G\cdot\sin^2\left(2\cdot\pi\cdot Ng\cdot L\left(\frac{1}{\lambda}-\frac{1}{\lambda_{peak}}\right)\right)} + BKG \qquad \textbf{3.10}$$

In the equation 3.10, $R\cdot G(\lambda)=R\cdot G(\lambda_{peak}) + \gamma\ (\ \lambda - \lambda_{peak}\ )$, $C(\lambda) = B(\lambda)(\ 1 + R\cdot G(\lambda)\ )\ (\ 1 - R\ ) = C\ (\lambda_{peak}) + \beta\ (\ \lambda - \lambda_{peak}\ )$, λ_{peak} is the peak wavelength of the individual mode, *BKG* is the background level. We assume that the spontaneous emission $B(\lambda)$ and the single pass gain $G(\lambda)$ vary linearly with wavelength over one mode. Thus, the small asymmetry of the Fabry-Pérot modes due to the change of the gain and ASE intensity with wavelength over the fitted range of approximately one free spectral range of the laser cavity is taken into account. The fitting is done in a Matlab program using the weighted non-linear least-squares fitting function *lsqnonlin* from the optimization toolbox. First a scan over the measured spectra is performed to extract starting values for λ_{peak} and *BKG*. Since the spectrometer also provides accurate frequency/wavelengths differences between the mode peak positions, the group index $Ng(\lambda)$ is calculated on the different $\lambda peak$ by using this formula: $Ng(\ (\lambda_{peak}^{\ i+1} + \lambda_{peak}^{\ i})\ /\ 2\ ) = (\lambda_{peak}^{\ i+1} + \lambda_{peak}^{\ i})^2\ /\ (8\cdot(\ \lambda_{peak}^{\ i+1} - \lambda_{peak}^{\ i})\cdot L)$. The group index as a function of wavelength is then fitted over the total spectral range using the Cauchy formalism: $Ng(\lambda) = N_0 + N_1\ /\ \lambda^2$. The fitting parameters in the airy function are therefore C, $R\cdot G$, β, γ, *BKG* and λ_{peak}. The weights used for the data points are defined in equation (3.11).

$$weight(\lambda) = \frac{1}{\sqrt{(\varepsilon.I(\lambda))^2 + \sigma^2_{BKG}}} \qquad \textbf{3.11}$$

$I(\lambda)$ is the measured signal intensity and σ_{BKG} the standard deviation of the background signal is determined from areas in spectrum with a very low signal intensity. The weight is one over the sum of the square root of the signals errors square [25]. The parameter ε is chosen in order to minimize the residue of the fit.

Tests have been performed for different spectrum intensities and InP based lasers. Results show that a clear reduction of the residue of the fit is obtained for low intensity signal $\varepsilon = 0.15 \pm 0.02$. The effect of ε is minor for signal closer to the threshold.

3.4.3 Gain curve measurements

The measurements were performed on a Fabry-Pérot InP/InGaAsP ridge waveguide laser on an InGaAsP chip that was fixed onto a temperature controlled copper mount. The laser output is coupled into a lensed fiber and led through an optical isolator to the high resolution OSA (APEX AP2041A). The OSA is based on a heterodyne receiver principle using a single mode tunable laser as a local oscillator which enables the achievement of a resolution of 0.16 pm (20 MHz) and a wavelength accuracy of ± 3 pm. The spectra were recorded in sections of 5 nm (20.000 points each) in order to have the full resolution available over the full wavelength range of interest. The measurement of one section takes less than 5 seconds. All the measurements were performed below the lasing threshold. No polarizer has been required as the polarization has been measured to be TE (30 dB polarizer extinction).

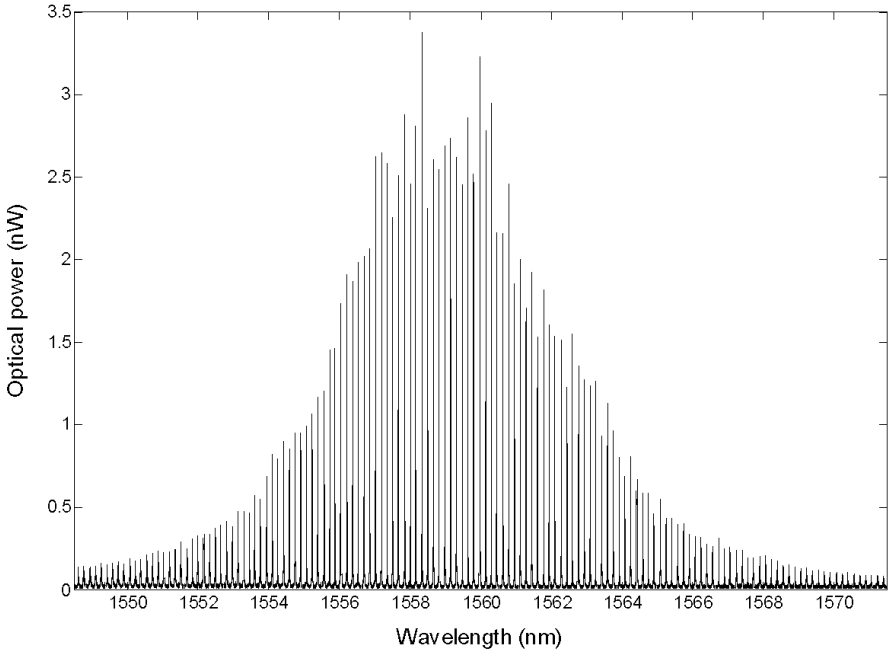

Figure 3.4.1 Typical example of a recorded subthreshold spectrum of a Fabry-Perot laser on a full span range. T=16°C I=89mA.

The laser layer stack consists of a 120 nm thick $\lambda = 1.5$ μm bulk InGaAsP layer between two 190 nm thick $\lambda = 1.25$ μm InGaAsP layers. The structure is clad by a

1500 nm thick p-InP layer with gradual doping levels and a 50 nm p-InGaAs contact layer. The cavity is 1985 μm long (± 1 μm) and the waveguide is 2 μm wide. The threshold is around 92 mA at 16°C and around 113 mA at 28°C. As can be seen in Figure 3.4.1 the cavity modes are very well resolved in this typical ASE spectrum. The result of a typical fit over three modes is presented in

Figure 3.4.2. The spectrometer fully resolves the modes which are fitted with an appropriate weighting of the data. Once all the modes in the spectra are fitted, the $R \cdot G$ products can be plotted versus the wavelength for each injected current value. Results for T= 16°C and T=28°C are plotted in Figure 3.4.3 a) and b). The typical gain shape is observed [26]. Very few observed modes did not lead to a good fit (<1%). This happened when an excess of noise is detected during the measurement. Those points are removed from further calculations on the gain curves. The gain peak shifts over 8.0 nm from 16°C to 28°C. The gain peak wavelength shifts to the smaller values with an increase in carrier density as expected. The temperature appears to have an effect on the shape of the gain spectrum on the short wavelength side. To bring out the difference in bandwidth observed at the two temperatures, the gain spectra recorded at 16°C and 28°C are combined in Figure 3.4.1. The gain spectra have been averaged over 1 nm (~6 modes) to reduce the noise. The gain maxima of the data at the two temperatures have been overlayed to illustrate that the bandwidth increases slightly with temperature by about 3 nm at the FWHM.

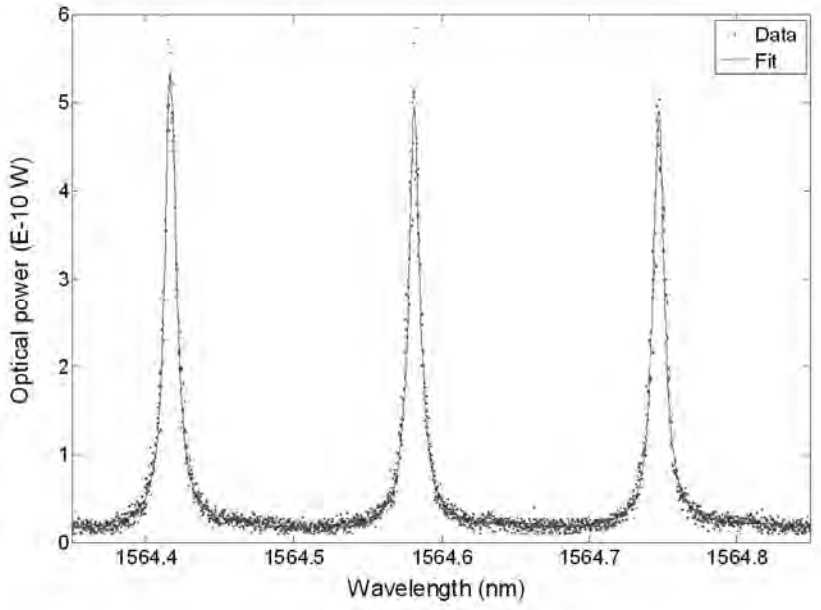

Figure 3.4.2 Measured and fitted spectra zoomed on three modes. T=16°C I=89mA.

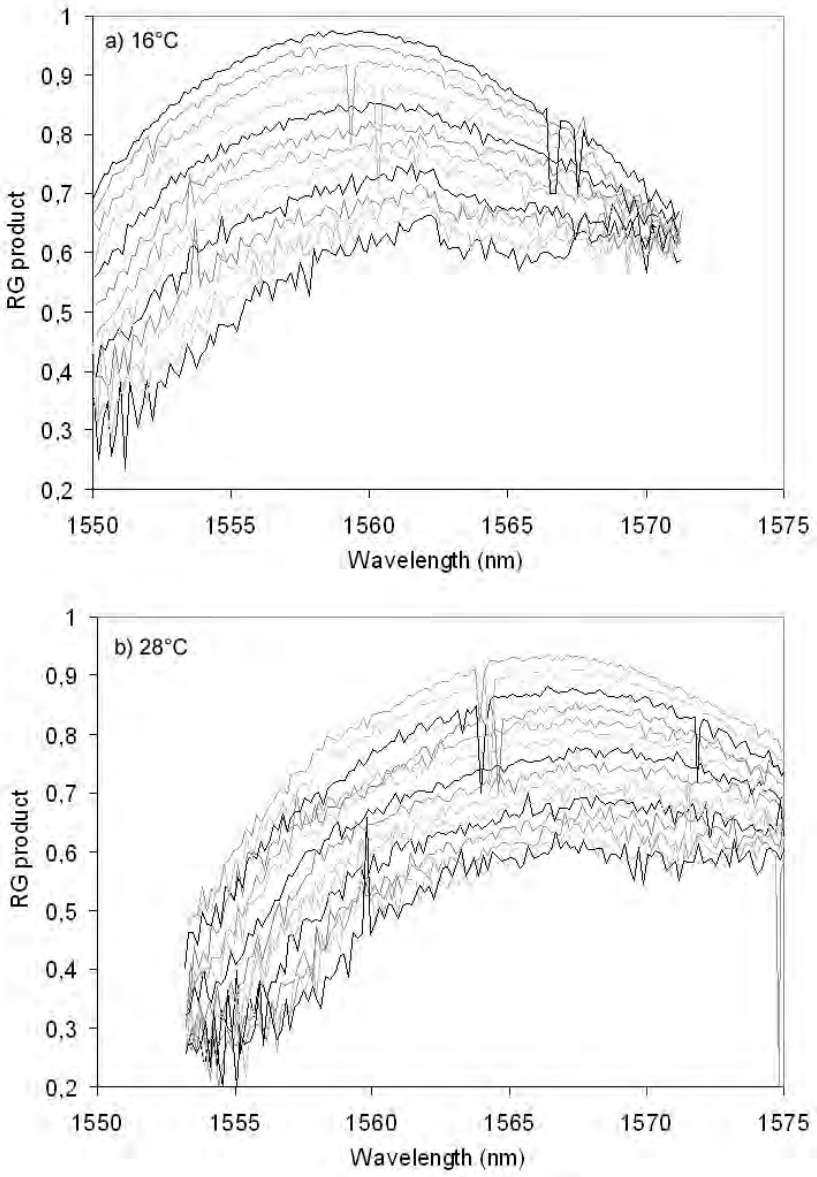

Figure 3.4.3 The *R·G* product versus the wavelength and for different laser current for a) T = 16°C b) T = 28°C. The gain Very few observed modes did not lead to a good fit, the *R·G* value is close to the guess value 0.7 chosen.

3.4.4 Discussion of the method

Measurements of the gain curves using the high resolution spectrometer gave smooth curves for $R \cdot G$ product values higher than 0.4, below this value $R \cdot G$ products becomes inaccurate. In a spectrometer, the high resolution inexorably limits the sensitivity of the equipment. The sensitivity of the instrument is specified for - 75 dBm. However level down to - 85dBm has been measured. On the other hand, high quality measurements are obtained at current values very close to the lasing spectrum. Wang and Cassidy have reported in [23] that the quality of their fitting of the modes became poor in the valleys in the gain regime where $R \cdot G$ came close to 1. In order to improve the fit, they tried to change the weighting. Performing the fit to the logarithm of the convolution of the airy function and thereby significantly increasing the weight of the lower values data points, as well as including their instrument response function, did improve their results. However they could not successfully fit to values of the $R \cdot G$ product close to and over 0.95. We have, using the high resolution spectrometer, been able to fit on the experimental data $R \cdot G$ products up to 0.975 using weighting as given in equation 3.11, while maintaining an excellent agreement of the measured and fitted laser modes. Figure 3.4.5 shows on a logarithmic scale the results of the fit of 3 modes compared with the experimental data. The $R \cdot G$ product is around 0.972 for the three modes. All the measured points of the mode peaks are distributed well on both sides of the fitted curve. We observed that above the laser threshold the measured optical mode becomes wider, and can no longer be fitted using the Airy function as is to be expected. The extracted $R \cdot G$ products are clamped to 0.99 and the shape of the mode starts to deviate from the airy function [27]. This is illustrated in Figure 3.4.6 where a measured and a fitted mode are shown at 1 mA above threshold.

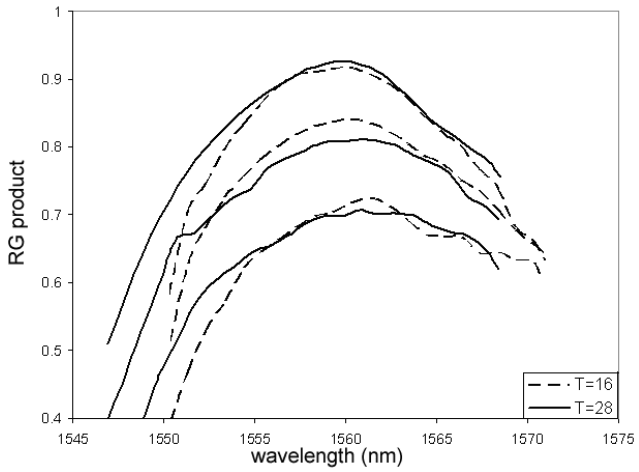

Figure 3.4.4 $R \cdot G$ product for two temperature 16°C and 28°C and 3 similar $R \cdot G$ values. The spectra for T=28°C has been shifted by 8 nm to better see the changes in shape.

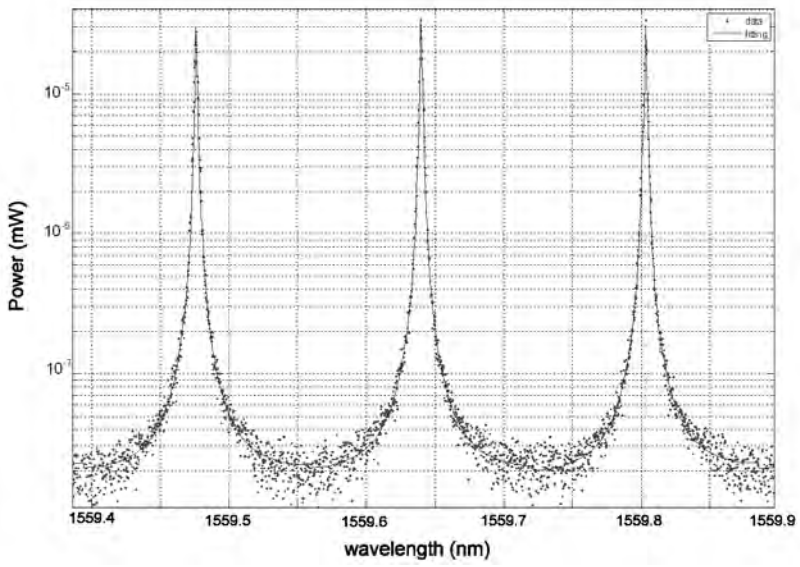

Figure 3.4.5 Measured and fitted spectra zoomed on three modes in a logarithmic scale. T=16°C I=90mA. The three modes are very well fitted.

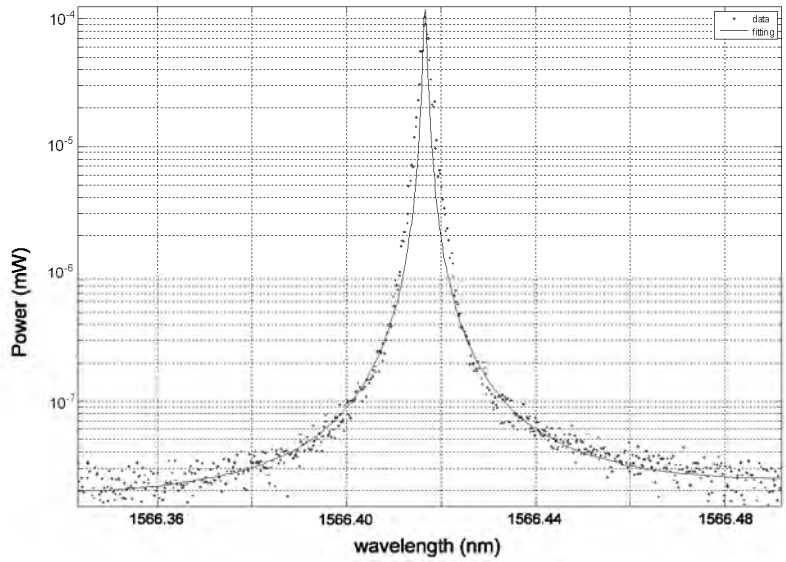

Figure 3.4.6 Measured and fitted spectra zoomed on a single mode in a logarithmic scale. T=28°C I=114 mA. This is 1 mA above threshold; the Airy function is not valid anymore.

3.4.5 Differential gain measurement

From the previously measured gain curves, the differential gain could be extracted. To improve the accuracy of the extracted differential gain per carrier, the gain curves have been smoothed over 6 modes (~ 1.0 nm). The net modal gain (g_{net}) per meter for each wavelength was then calculated using equation (3.12). This net gain is equal to the material gain g_m times the confinement factor Γ minus the total optical losses of the cavity α_{loss} which are comprised of the free carrier absorption within the active region and losses due to scattering.

$$g_{net} = \frac{1}{L} \cdot \ln\left(\frac{RG}{R}\right) = \Gamma \cdot g_m - \alpha_{loss} \qquad \textbf{3.12}$$

To determine the differential gain a relation between the injected current and the carrier density is required. Below the laser threshold N can be extracted from the simplified rate equation (3.13).

$$\frac{N}{\tau} + B.N^2 + C.N^3 = \frac{I}{q \cdot S_{ActiveLayer} \cdot L} \qquad \textbf{3.13}$$

Here τ is the carrier lifetime, B is the bimolecular recombination coefficient, C is the Auger recombination coefficient, I is the injected current, q is the charge of the electron, $S_{ActiveLayer}$ is the cross-section surface of the active layer of the SOA and L is the length of the laser cavity. All the values of the parameters used are listed in Table 3.4.1.

Table 3.4.1: Values of the parameters used for the carrier density calculation.

Parameter	Description	Value used
Γ	Confinement factor	0.285
τ	Carrier lifetime	600 ps
B	Bimolecular recombination coefficient	$2.62.10^{-16}$ $m^3.s^{-1}$
C	Auger recombination coefficient	$5.269.10^{-41}$ $m^6.s^{-1}$
$S_{ActiveLayer}$	Surface of the active region	0.12x2 μm^2
L	Length of the cavity	1.85 mm

A contour plot of the net optical modal gain as a function of carrier density and wavelength is presented in Figure 3.4.7. From this figure one can see that the net modal gain at one wavelength varies non-linearly with the carrier density, even over this small range of carrier densities. This is most pronounced at the shortest

wavelength in the plot. A common description for the relation between the material gain and the number of carriers is given below [28].

$$g_m = aN \cdot N_0 \cdot \ln\left(\frac{N}{N_0}\right) \qquad \textbf{3.14}$$

Here aN is the differential gain factor, N is the carrier density and N_0 is the transparency carrier density. The carrier density at transparency needs to be known for each wavelength and temperature. This was done by injecting light from a tunable laser (Agilent 81600B) that was modulated on/off at 1 kHz. The average power injected into the laser was - 3 dBm. The current of the laser under test is then scanned and the amplitude and phase of the modulation of the voltage over the laser as a result of the modulated input light is recorded using a lock-in amplifier. At the transparency current the interaction of the input light with the gain material should be minimal and the amplitude of the modulation is at a minimum. A clear jump in the phase of the modulation is also observed at the transparency point as the interaction of the laser light with the gain material changes from absorption to amplification. An example of an amplitude and phase signal from the lock-in amplifier is presented in Figure 3.4.8. In this way we have measured the transparency current for 12, 20 and 28°C and for wavelengths between 1510 and 1590 nm. The carrier densities were calculated from the measured current using equation 3.13. The results are presented in Figure 3.4.9 for different 3 temperatures. The transparency carrier density decreases almost linearly with the wavelength and increases significantly with temperature (~$8.4 \cdot 10^{21} \cdot m^{-3}$ per degree). To obtain values of the transparency carrier densities required in the differential gain calculation for wavelength values in the studied range and temperature, the presented graphs have been interpolated.

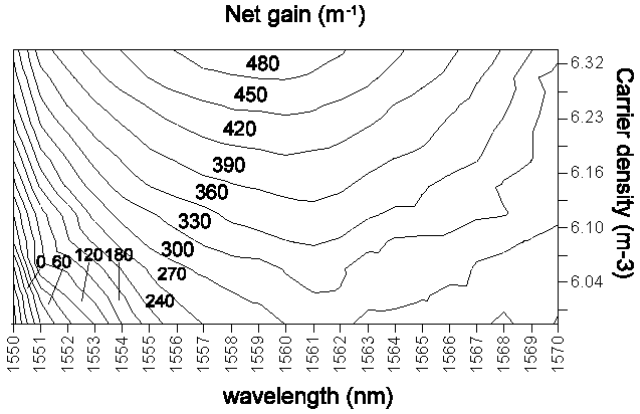

Figure 3.4.7 Contour plot of the measured net optical modal gain in the laser as a function of carrier density and wavelength at T = 16°C. At a fixed wavelength one can see that the gain does not increase linearly with carrier density, especially at the shorter wavelengths.

The discrete differential of the material gain ($\partial g_m/\partial N$) is calculated in order to extract $aN(\lambda)$ without knowing the optical losses (equation 3.15). Once the differential gain factor is known one can extract the internal losses from equation 3.12.

$$\frac{\partial g_m}{\partial N} = \frac{\partial}{\partial N}\left(\frac{1}{L\cdot\Gamma}\cdot \ln\left(\frac{RG(N,\lambda)}{R}\right)\right) = aN\cdot\frac{N_0}{N} \qquad \textbf{3.15}$$

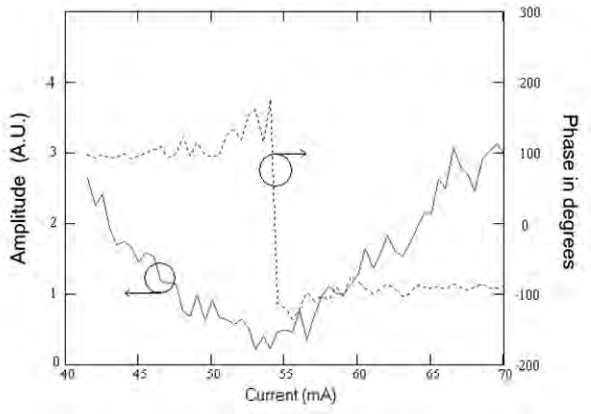

Figure 3.4.8 Measured amplitude and phase of the voltage modulation at the laser, versus the current injection, when a modulated light from a tunable laser is injected. A clear transition in the phase indicates the transparency current.

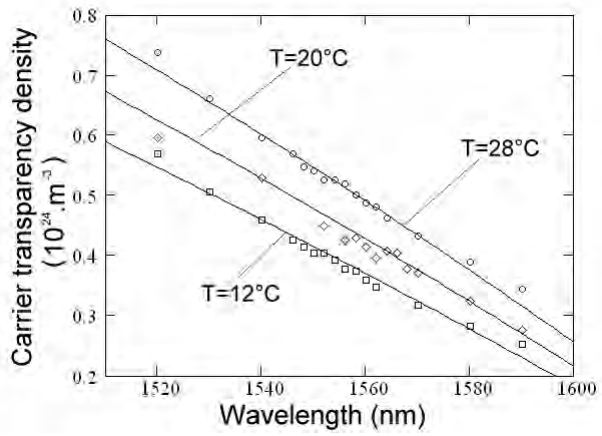

Figure 3.4.9 Measured transparency carrier, recalculated in carrier densities, as function of the wavelength (at the temperatures of 12, 20 and 28°C).

Figure 3.4.10 shows the results of the differential gain from two temperatures (16°C and 28°C). We observed that at a fixed temperature, the differential gain as well as the transparency carrier density, decreases linearly with the wavelength over the observed wavelength range. Indicated in Figure 3.4.10 are the wavelengths at which the device starts lasing for both temperatures which indicates the maximum modal gain. This graph has to be interpreted together with the transparency carrier density graph for different wavelength and temperatures (Figure 3.4.9). With an increase of temperature, the maximum modal gain shifts to longer wavelengths. The transparency carrier density increases with temperature and this rise is larger for the shortest wavelengths. Meanwhile the differential gain increases with temperature as well. We observed that the slope of the linear fits decreases slightly with temperature and that the differential gain is lower at the maximum gain. Values reported here are higher than typical values reported in the literature for bulk InP/InGaAsP material [29,30,31]. This difference stems from the definition that we have used for this parameter. The values listed here are the differential gains at the transparency density. The carrier density at laser threshold is typically significantly higher in order to overcome the mirror losses. If a linear gain model is used to describe the gain in a laser, the differential gain parameter is usually determined near the laser threshold. Looking at the equation 3.14 one can see that a lower value of the differential gain parameter in the linear gain model is to be expected.

Once the differential gain is known, the losses could be calculated. Values for 16°C are - 32 dB/cm and values for 28°C are - 33 dB/cm. We attribute this increase in losses with temperature to the higher carrier concentration needed in the semiconductor at higher temperature.

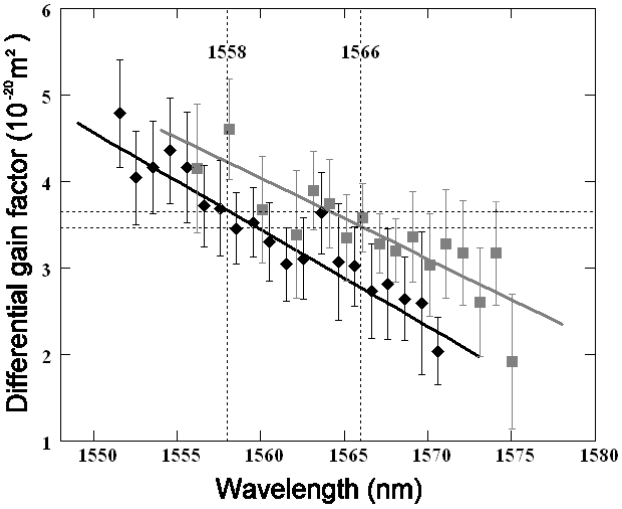

Figure 3.4.10 The differential gain parameter aN ($\cdot 10^{-20}$.m^2) as a function of the wavelength and for the temperatures T = 16°C (black diamonds) and T = 28°C (grey squares). Wavelengths at which the device starts lasing for the two temperatures (the maximum of the gain) are indicated.

3.4.6 Conclusion

We have demonstrated the use of an ultra-high resolution (20 MHz) spectrometer to accurately record subthreshold ASE spectra from a Fabry-Pérot InP/InGaAsP laser and determine the optical gain. The method is based on a non-linear least-squares fitting of the observed modes. The spectrometer fully resolves the modes which could be fitted accurately and the effect of the response function of the OSA does not need to be compensated for. 1 mm long device is a typical limit for a standard spectrometer in this wavelength range. Using the high resolution spectrometer allows to measure devices longer than this limit. Measurements have been performed on a 2 mm device and $R \cdot G$ products up to 0.975 have been measured without any discernable difference between the measured and fitted laser modes. It has been observed that nearer to and above the lasing threshold the shape of the mode deviates from the Airy function and cannot be fitted [27]. The optical gain spectrum of the laser has been measured successfully for different temperatures and subthreshold current values. The net gain curves obtained confirm the necessity of using the logarithmic relation between gain and carriers. The differential gain parameter in the gain relation has been determined using measured transparency carrier density values for each wavelength and temperature. The parameters determined in this paper will be used in our laser simulation models.

3.5 List of references

1 E. Pennings, G-D Khoe, M. K. Smit, and T. Staring, "Integrated-optic versus microoptic devices for fiber-optic telecommunication systems: A comparison," IEEE Journal of Selected Topics in Quantum Electronics, Vol. 2, Issue 2, pp. 151-164, (1996)

2 E.J. Skogen, J.S. Barton, S.P. Denbaars, L.A. Coldren, "A quantum-well-intermixing process for wavelength-agile photonic integrated circuits", IEEE Journal of Selected Topics in Quantum Electronics, Vol. 8, Issue 4, pp 863- 869, (2002)

3 N. Futakuchi, X. Song, D. Miyashita, M. Kato, Y. Nakano, "Fabrication of InGaAsP/InP Mach-Zehnder interferometer optical amplifier switches by metalorganic vapor phase selective area epitaxy" in Proc. IEEE IPRM 2001, pp. 583-586, (2001)

4 L. XU, M. R. Gokhale, P. Studenkov, J. C. Dries, C.P. Chao, D. Garbuzov, and S. R. Forrest, "Monolithic Integration of an InGaAsP-InP MQW LaserNaveguide Using a Twin-Guide Structure with a Mode Selection Layer" IEEE Journal Photonics Technology Letters, Vol. 9, Issue 5, pp. 369-371, (1997).

5 M.J.R. Heck, E.A.J.M Bente, Y. Barbarin, D. Lenstra and M.K. Smit "Simulation and Design of Integrated Femtosecond Passively Mode-locked Semiconductor Ring Lasers Including Integrated Passive Pulse Shaping Components" IEEE Journal of Selected Topics in Quantum Electronics, Vol. 12, No. 2, pp 265-276, (2006)

6 U. Khalique, Y. Zhu, J.J.G.M. van der Tol, L.M. Augustin, R. Hanfoug, F.H. Groen, P.J. van Veldhoven, M.K. Smit, "Ultrashort polarization converter on InP/InGaAsP fabricated by optical lithography" proc. IPRA 2005, IWA3, 11-15 April 2005, San Diego, CA, pp. 1-3, (2005)

7 F.M. Soares, F. Karouta, E.J. Geluk, J.H.C. van Zantvoort, H. De Waardt, R. Baets, M.K. Smit, "Low-loss INP-based spot-size converter based on a vertical taper", Proc. ECIO '05, 6-8 April 2005, Grenoble, France, pp. 104-107, (2005)

8 Y. Barbarin, E.A.J.M. Bente, C. Marquet, E.J.S Leclère, J.J.M. Binsma and M.K. Smit. "Measurement of Reflectivity of Butt-Joint Active-Passive Interfaces in Integrated Extended Cavity Lasers" IEEE Photonics Technology Letters, Vol. 17, issue 11, pp. 2265-2267, (2005)

9 Y. Barbarin, E.A.J.M Bente, T. de Vries, J.H. den Besten, P.J. van Veldhoven, M.J.H. Sander-Jochem, E.J. Smalbrugge, F.W.M.v. Otten, E.J. Geluk, M.J.R. Heck, X.J.M. Leijtens, J.G.M. van der Tol, F. Karouta, Y.S. Oei, R. Nötzel and M.K. Smit "Butt-Joint Interfaces in InP/InGaAsP waveguides with Very Low Reflectivity and Low Loss" IEEE LEOS Benelux 2005 Mons, Belgium

10 R.W. Tkach and A.R. Chraplyvy, "Regimes of feedback effects in 1.5 um distributed feedback lasers", Journal Lightwave Technology, Vol 4, pp. 1655-1661, (1986)

11 S.W Corzine, R.H Yan, L.A Coldren, "Optical gain in III-V bulk and quantum well semiconductors" Quantum well lasers (A95-14956 02-36), San Diego, CA, Academic Press, Inc., 1993, p. 17-96

12 Y. Barbarin, E.A.J.M Bente, L. Mussard, G. Servanton, Y.S. Oei, R. Nötzel and M.K. Smit "Gain Measurements of Fabry-Pérot InP/InGaAsP Lasers using an Ultra High Resolution Spectrometer" Applied Optics, Vol. 45, Issue 35, pp. 9007-9012 (2006)

13 R.G. Broeke "A wavelength converter integrated with a discretely tunable laser for wavelength division multiplexing networks" Ph.D Thesis Delft University of Technology (2002)

14 J.H den Besten "integration of multiwavelength lasers with fast electro-optical modulators" Ph.D Thesis Eindhoven University of Technology, ISBN 90-386-1643-0, (2004)

15 Y. Barbarin, E. A. J. M. Bente, M. J. R. Heck, J. H. den Besten, G. Guidi, Y.S. Oei, J.J.M. Binsma, M.K. Smit "Realization and Modeling of a 27-GHz Integrated Passively Mode-Locked Ring Laser", IEEE Photonics Technology Letters, Vol 11, Issue 11, pp 2277-2279, (2005)

16 K. Petermann "Laser Diode Modulation And Noise" Kluwer Academic, p. 161, 1988. ISBN 90-277-2672-8.

17 I.P. Kaminow, G Eisenstein and L.W. Stulz "Measurement of the modal reflectivity of an antireflection coating on a superluminescent diode" IEEE Journal of Quantum Electronics, Vol. 19, Issue 4, pp. 493-495, (1983)

18 J.J.M. Binsma, M. van Geemert, F. Heinrichsdorf, T. van Dongen, R.G. Broeke, and M.K. Smit, "MOVPE waveguide regrowth in InGaAsP/InP with extremely low butt joint loss," in Proc. IEEE/LEOS Symp. Benelux Chap. pp. 245-248, (2001)

19 D.F. Clark and M.S. Iqbal, "Simple extension to the Fabry-Pérot technique for accurate measurement of losses in semiconductor waveguides," Optics Letters, Vol. 15, Issue 22, pp. 1291-1293, (1990)

20 D.A. Ackerman, L.M. Zhang, L.J-P. Ketelsen and J.E. Johnson, "Characterizing Residual Reflection Within Semiconductor Lasers, Integrated Sources, and Coupling Optics", IEEE Journal of Quantum Electronics, Vol. 34, Issue 7, pp. 1224-1230, (1998)

21 B.W. Hakki and T. Paoli, "Gain spectra in GaAs double heterostructure injection lasers", Journal Applied Physics, Vol. 46, Issue 3, pp. 1299-1305, (1975)

22 D.T. Cassidy, "Technique for measurement of the gain spectra of semiconductor diode lasers", Journal Applied Physics, Vol. 56, Issue 11, pp. 3096-3099, (1984)

23 H. Wang and D.T. Cassidy, "Gain Measurement of Fabry-Pérot Semiconductor Lasers Using a Non-Linear Least-Squares Fitting Method", IEEE Journal of Quantum Electronics, Vol.41, Issue 4, pp. 532- 540, (2005)

24 E.I. Gordon "optical maser oscillators and noise" Bell System Technology Journal, Vol. 43, pp. 507-539, (1964).

25 S.B. Alexander "Optical Communication Receiver Design" IET Technology & Industrial Arts ISBN 0852969007, (1997)

26 J. Hader, J.V Moloney, S.W. Koch, "Microscopic theory of gain, absorption, and refractive index in semiconductor laser materials-influence of conduction-bandnon parabolicity and Coulomb-induced intersubband coupling" IEEE Journal of Quantum Electronics, Vol. 35, Issue 12, pp. 1878-1886, (1999)

27 G.P. Agrawal, N.K. Dutta, "Semiconductor lasers" ISBN 0-442-01102-4 NewYork: Van Nostrand Reinhold, p. 142, (1993)

28 A. DeTemple, C.M. Herzinger, "On the semiconductor laser logarithmic gain-current density relation" IEEE Journal of Quantum Electronics, Vol. 29., Issue 5, pp 1246-1252, (1993)

29 W. H. Guo, Y. Z. Huang, C. L. Han, and L. J. Yu, "Measurement of gain for Fabry–Pérot semiconductor lasers by the fourier transform method with a deconvolution process," IEEE Journal of Quantum Electronics, Vol. 39, Issue 6, pp. 716-721, (2003)

30 L. Occhi, L. Schares and G. Guekos, "Phase Modelling Based on the α-Factor in Bulk Semiconductor Optical Amplifiers", IEEE Journal of Selected Topics in Quantum Electronics, Vol.9, Issue 3, (2003)

31 T. Durhuus, B. Mikkelsen and K.E. Stubkjaer, "Detailed Dynamic Model for Semiconductor Optical Amplifiers and Their Crosstalk and Intermodulation Distortion", Journal of Lightwave Technology, Vol.10, Issue 8, pp. 1056-1065, (1992)

Chapter 4
Application of deep-etched waveguides in AWGs and QD lasers

4.1 Introduction

The rise in speed of the optical telecommunication networks creates a drive towards higher repetition rates and shorter pulse lengths of the laser sources. Therefore there is a drive to increase the repetition rate of modelocked lasers to values like 40GHz or more. The repetition rate of modelocked lasers is inversely proportional to its cavity length, thus to its foot print. At first, this is an advantageous as smaller size means more devices on a wafer, more functionality and lower cost. However for ring lasers, decreasing the size of the devices involves an increase in the required index contrast of the waveguides in order to be able to accommodate the smaller radius of curvature. For instance, a modelocked ring laser with a repetition rate higher than 20 GHz can not be realized in our technology with shallowly etched ridged or buried waveguides. Narrow deeply etched ridge waveguides allow for a small bending radius but unfortunately can in general not be used everywhere in all devices. Firstly, fully deeply etched structures have higher scattering losses. Secondly, deeply etched bulk or quantum well SOAs are detrimentally affected by sidewall recombination effects. Using the active-passive technology presented in Chapter 3 the repetition rate of an RMLL can be increased further. This can be realized by combining shallowly etched waveguides, shallowly etched active waveguides (SOA), and deeply etched passive waveguides for the sharp bends. For further increase of the repetition rate, lasers utilizing only high contrast waveguides need to use a different active material, Quantum Dots (QD) SOA, which is far less sensitive to surface sidewall recombination as demonstrated in the work presented here.

In this chapter we first present results from a very compact passive device, an Arrayed Waveguide Grating (AWG), in which the two types of passive waveguides are combined. The AWG is one of the key devices in PICs because of its use in optical communication. The results illustrate that a much smaller device can be realized with equivalent performances. The insertion losses are comparable and the crosstalk figures are slightly higher compared with more traditional AWGs realized in InP. However

with matured technology, crosstalk figures below − 30 dB are feasible. We have reported these results in [1]. In Section 4.3, we report on the realization and characterization of InAs/InP (100) quantum dot Fabry-Pérot and ring lasers that make use of narrow deeply etched ridge waveguides. The lasers operate in the 1.55 μm wavelength range. The fabrication of this particular wafer is described as well. The performance of the lasers appears not to be affected by sidewall recombination effects. Shallowly and deeply etched FP lasers show the same performance. We also present results obtained from a compact ring laser with a free spectral range close to 40GHz. Such a device could not be realized using shallowly etched waveguides. These results have been reported in [2].

4.2 Compact AWG realized using a double-etch process.

4.2.1 Introduction

Phased-array demultiplexers [3] or Arrayed Waveguide Gratings (AWGs) are key components for Wavelength Division Multiplexing (WDM) applications. Large-scale integration of this component pushes the size reduction to the limits of the current processing technology. Small polarization-independent phased-array demultiplexers have been reported with a size of 300 x 340 μm^2 by Bissessur et al. [4] using only deeply etched waveguides and a bending radius of 100 μm. To further decrease the size of an AWG and to have an acceptable loss value, it is required to decrease the radius of curvature of the waveguides and to combine deeply and shallowly etched waveguides [5,6]. The increased scattering losses introduced by the straight and curved deeply etched waveguides are compensated by the reduction of the device size. We have tested many AWGs, varying different parameters. In this section we present the design and the performance of the smallest: the size is reduced to 230 x 330 μm^2. Afterwards follows an analysis of the reduction of the Array Acceptance Factor (AAF) on AWG's crosstalk and insertion losses. The fabrication is a simple double etch process as described in Chapter 3, but at that time positive photoresist was used for the masking of the deep areas. The SiNx layer was removed in a buffered HF solution.

4.2.2 Design of the AWG.

We have designed an extremely small four-channel AWG with a 400 GHz channel spacing (3.2 nm at 1550 nm) and a Free-Spectral-Range of 12.8 nm (Figure 4.2.1). The minimum bending radius used for the array waveguides was 30 μm. Although an even smaller minimum radius could have been used, it does not significantly reduce the device size. The AWG was designed for a ridge waveguide structure consisting of a 720 nm thick InGaAsP waveguide layer (bandgap wavelength 1.25 μm) with a 1200 nm thick InP upper cladding layer. Next design parameter to be defined is the Array Acceptance Factor (AAF). A definition of this parameter is plotted in Figure 4.2.2. The beam propagating through the input waveguide and entering the slab region is no longer laterally confined and becomes divergent. The divergent beam is approximately Gaussian with a waist parameter θ_0. Only a part of the far field is accepted by the waveguide array. The corresponding far field angle divided by θ_0, defines the Array Acceptance Factor (AAF). In this design, the angular region corresponding to an AAF of 2.4 holds 12 array waveguides.

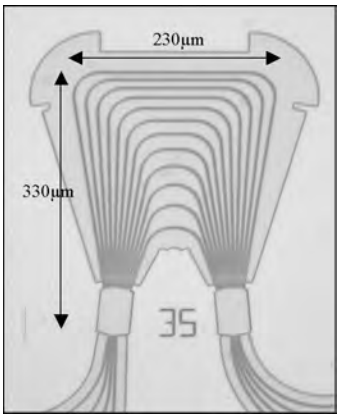

Figure 4.2.1 Photograph of the fabricated compact AWG

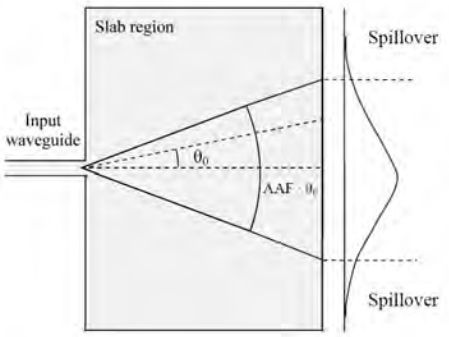

Figure 4.2.2 Definition of the Array Acceptance Factor (AAF), A value of AAF = 4 is shown.

The first 10 μm of the waveguides in the array of the small AWG, connected to the slab region (Figure 4.2.3), are 2.0 μm wide and shallowly etched (100 nm depth in the filmlayer). The array arms themselves and the input waveguides are 1.7 μm wide and deeply etched (150 nm through the filmlayer). The deep-shallow transition is done gradually using a 50 μm long taper. A better coupling is obtained by using an extra width of 0.3 μm between the taper and the shallow waveguide. More details are available in [7]. The device was designed for a 720 nm thick filmlayer (bandgap wavelength 1.25 μm) and a 1200 nm thick InP cladding layer. With this layerstack and a deeply etched waveguide width of 1.7 μm the propagation constant of the fundamental mode is polarization independent. However, due to the material available, we have realized this AWG in a layer stack with a 500 nm thick InGaAsP waveguide layer (bandgap wavelength 1.35 μm) with a 300 nm thick InP cladding layer. Because of this change, the device is not polarization independent.

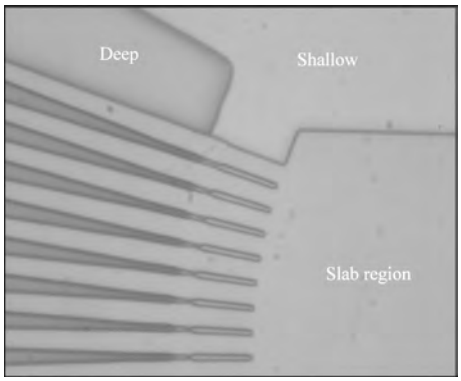

Figure 4.2.3 Photograph of deep-shallow waveguide transition. The transition is done gradually using a 50 μm long taper.

4.2.3 Measurements results of the compact AWG.

Losses for deeply and shallowly etched straight waveguides were measured using the Fabry-Pérot technique [8]. An average of 2.2 dB/cm was obtained for shallowly etched straight waveguides. 5.5 dB/cm was obtained for deeply etched straight waveguides. Losses for a 1.7 μm wide deeply etched waveguide are almost 2 dB/cm higher than with a single etching process. This is due to the masking of the shallow parts by photoresist, which has introduced sidewall roughness during the etching. Losses for 2 μm wide shallowly etched waveguides are slightly higher in comparison to similar waveguides made with a single etch process. The transmission spectrum of the small AWG was measured using the spontaneous emission spectrum of an EDFA as a broad-band light source and a polarizer to select the polarization state. Light was coupled into the chip using microscope objectives, then coupled out of the waveguides by a single-mode lensed fiber and analyzed with an optical spectrum analyzer. The reference EDFA spectrum that defined the insertion loss level was determined from transmission spectra of a large number of separate good waveguides. Figure 4.2.4 shows the measured transmission spectra for both polarizations of the small AWG. Measured insertion losses are less than 5 dB and the crosstalk is below – 12 dB. As expected, due to the fact that we used a 500 nm thick filmlayer instead of 720 nm, the devices have some polarization dependence in agreement with simulations. This particular device shows a 2.3 nm shift between the two polarizations. We notice a difference of 2 dB between the transmission of the center channel and the outer channels. This is to be expected for a periodic device.

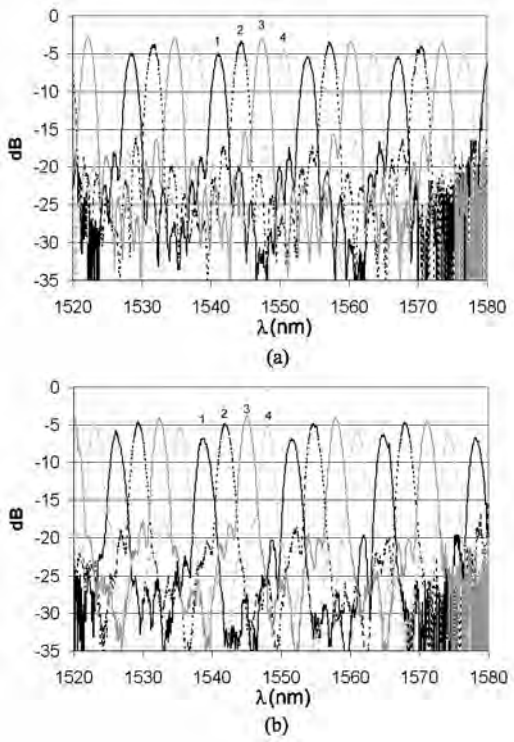

Figure 4.2.4 Measured transmission spectra of the small AWG for TE (a) and TM (b). As expected with a 500 nm thick filmlayer the device shows some polarization dependence.

Because of the crosstalk, the device presented is more suitable to be integrated in a multi-wavelength laser (MWL) [9,10] than in an add-drop multiplexer (ADM) or an optical crossconnect (OXC). For MWL integration, the periodicity of the device requires narrow gain material centered on the transmission spectra to avoid the lasing in other Free Spectral Range.

4.2.4 Effect of the reduction of the AAF

The Array Acceptance Factor (AAF) is an important parameter in the design of a small AWG as it determines the number of arms and thus the size of the device. Figure 4.2.5 and Figure 4.2.6 show the AAF influence on the insertion losses and the crosstalk measured from a series of AWGs with a constant a bending radius of 100 μm and a design similar to the one described in [4]. The insertion loss is almost independent of the AAF for values above 2.5. Below that factor, however, the loss starts to rapidly increase. The crosstalk shows the same behavior: a clear increase for an AAF factor below 2.5. We believe that these results are independent of the bending radius and the specific design of the array arms.

The device presented above has an AAF of 2.4 and a minimum bending radius of only 30 μm. The measured insertion losses are less than 5 dB and the crosstalk is below – 12 dB. Those values fit well with the previous graphs for this value of the AAF.

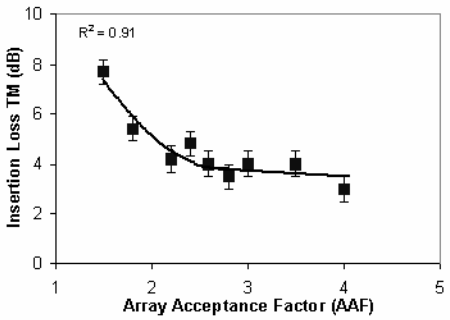

Figure 4.2.5 Measured insertion losses versus the Array Acceptance Factor (AAF)

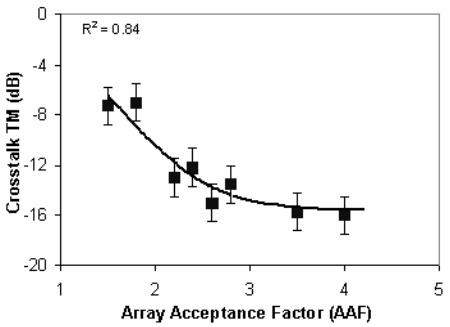

Figure 4.2.6 Measured crosstalk versus the Array Acceptance Factor (AAF)

4.2.5 Conclusion

A compact low-loss 4x4 AWG demultiplexer with a channel spacing of 400 GHz has been fabricated. The device size is only 230 x 330 μm², this was the smallest AWG reported at the date of publication. Measured insertion losses are less than 5 dB and the crosstalk is below – 12 dB. The results illustrate that a much smaller device can be realized with equivalent performances.

4.3 Deeply etched quantum dots lasers

4.3.1 Introduction

Quantum dot (QD) lasers and amplifiers are of great interest for optical telecommunication. QD lasers have a very low transparency current density per dot layer, a wide gain bandwidth and can have a much lower threshold current density [11] compared to bulk or quantum well lasers. The use of QD optical amplifiers for the regeneration of optical data streams has been reported in literature (e.g. [12]). For the use of QD lasers and amplifiers in optical integrated circuits for telecommunication, there are two important aspects. The first is the operation in the C and L band; the second is the option to have deeply etched mono-mode ridge QD waveguide amplifiers which allow for significantly more compact devices. QD material has the advantage over other active materials with respect to the spreading and sidewall recombination [13] of injected carriers. . It has been reported in [14] that PL intensities of 1.2 μm InAs QDs deeply etched mesas depend weakly on the mesa size down to 200 nm. Deeply etched InAs/GaAs QD lasers have been reported with waveguide mesa widths down to 1 μm in the 1.3 μm wavelength range [13,15,16,17]. A ring laser at 1.3 μm has also been reported [18], with a 10.28 mm long ring shallowly etched. Our main interest in the work presented here is the ability to produce ring laser cavities with a free spectral range such as 40 GHz or higher. In this paper we present first results on QD lasers, lasing in the 1.55 μm wavelength range, with mono-mode deeply etched waveguides (1.65 μm width). The presented lasers are Fabry-Pérot (FP) and ring cavity types. All our high contrast deeply etched QD lasers have the same threshold current density as shallowly etched ones and do not deteriorate over many hours of operation. It appeared that due to the low absorption of the QDs, the output waveguides of the ring lasers do not need to be contacted and injected with current for operation of the ring lasers with reasonable output power. This shows that for specific applications QD active materials offer the possibility to integrate active and passive devices on a single chip in a uniform layer stack.

4.3.2 Fabrication of the quantum dots wafer

The QD laser structure was grown on n-type InP (100) substrates by metal organic vapor-phase epitaxy (MOVPE). In the active region, five-fold stacked InAs QD layers separated by 40 nm thick InGaAsP (λ_Q = 1.25 μm; Q1.25) were placed in the center of a 500 nm thick lattice-matched Q1.25 waveguide core. The choice of the Q1.25 waveguide core is the result of an optimization made with regards to the application of this material in active/passive photonic integration using selective area regrowth (Section 3.2, [19]). It is a compromise between the maximum confinement energy of the QDs for temperature stability of active devices, a large electro-optic effect for phase modulators in passive areas, and maintaining a large refractive index contrast for strong vertical optical mode confinement. The nominal InAs amount for QD formation was 3.5 monolayers. One monolayer GaAs interlayer was inserted underneath each QD layer to suppress unwanted As/P exchange reactions during QD

growth to tune the QD emission wavelength into the 1.55 μm region [20]. An Atomic Force Microscope (AFM) image shown in Figure 4.3.1 reveals defect free QDs with an area density of ~ 3×10^{10} cm^{-2}. QD dimensions are 30 – 60 nm in diameter and 4 – 7 nm in height. A cross-sectional Transmission Electron Microscope (TEM) image of the grown layer stack centered on 3 layers of dots is shown in Figure 4.3.2. Bottom and top claddings of the laser structure are 500 nm n-InP buffer and 1.5 μm p-InP completed by a compositionally graded 75 nm p-InGaAsP contact layer. The device performance of shallowly etched narrow ridge waveguide QD lasers processed from the same material is reported in [21].

The waveguides have been processed using Reactive Ion Etching (RIE). For electrical isolation between contacted waveguides, the contact layer and part of the top cladding were removed. Before contacting the waveguides have been planarized by polyimide (see Section 3.2.2). A cross-sectional scanning electron microscopy (SEM) image of the laser structure is shown in Figure 4.3.3. The electrical isolation between different contacts is 200 kΩ, which is more than sufficient.

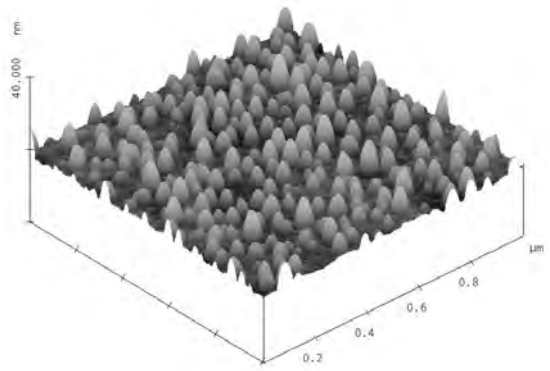

Figure 4.3.1 AFM image of the surface the same QDs than the one used in the lasers

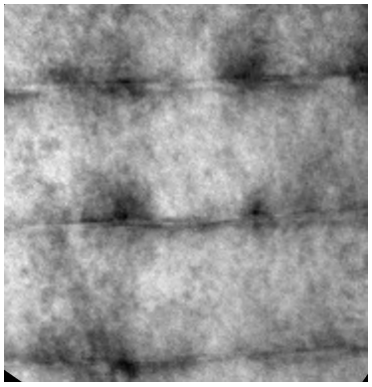

Figure 4.3.2 TEM image of the cross section of the similar wafer than the one used for the lasers. The spacing between the QDs layers is 40 nm.

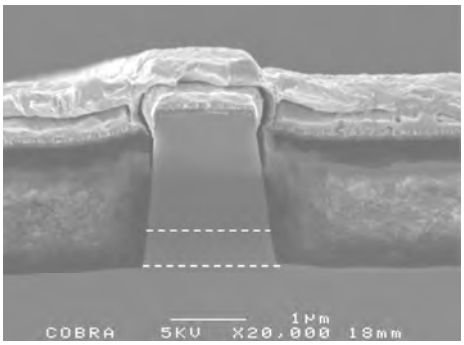

Figure 4.3.3 SEM image of the cross section of the 1.65 μm wide deeply etched ridge waveguide QD laser. The Q1.25 waveguide core is indicated by two dashed lines.

4.3.3 Fabry-Pérot laser results

The cavity length of the 1.65 μm wide deeply etched FP QD laser is 2.0 mm, defined by cleaving. The cleaved facets are un-coated. Comparison with the shallowly etched QD lasers shows that lasing occurs on the QD ground states [21]. The threshold current density in continuous wave (CW) operation is 3.3 kA/cm² at 15°C, which is the average value for eight different lasers. The value is affected by thermionic emission of the carriers from the QDs to the InGaAsP barriers due to the relatively low energy barrier height. Most remarkable, the threshold current density is the same as that of the 2 μm wide shallowly etched ridge QD lasers which are on the same chip. This demonstrates that the performance of the deeply etched lasers does not suffer from surface recombination at the etched sidewalls due to the three-dimensional confinement of injected carriers in the QDs [13]. The QD lasers did not degrade with time as compared with bulk lasers fabricated in the same way and passivated by the polyimide, where lasing stops after one hour when pumped at twice the initial threshold current.

The optical output power of the FP QD laser from one facet as a function of the current density for different temperatures in CW operation is plotted in Figure 4.3.4. The light was collected using an objective lens (N = 0.65). Output powers up to a few milliwatts are obtained. From the PI curves a value of the critical temperature T_0 of 20 K at room temperature is determined, the same value as that for shallowly etched lasers. This relatively low T_0, for CW operation, is dominated by thermionic emission of carriers from the QDs to the Q1.25 barriers. Figure 4.3.5 shows a typical lasing spectrum measured with a high resolution optical spectrum analyzer (HROSA), APEX 2401A. The wide lasing spectrum is due to the 80 nm gain bandwidth [21] and the inhomogeneous character of the QD gain medium. For the eight lasers measured, the central wavelength varies from 1565 nm to 1595 nm.

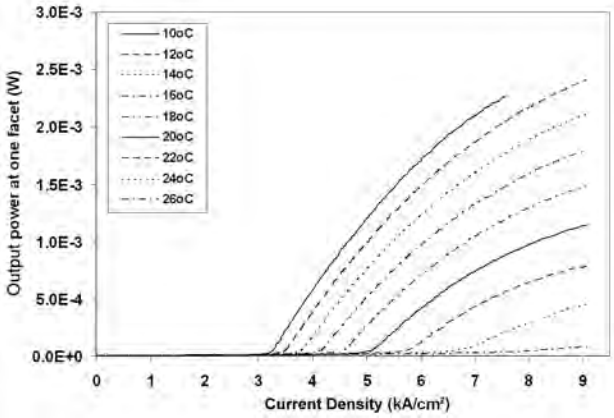

Figure 4.3.4 Output power at one facet of the deeply etched FP QD laser as a function of current density for different temperatures. The light was collected using an objective lens (N = 0.65). The critical temperature T_0 is 20 K.

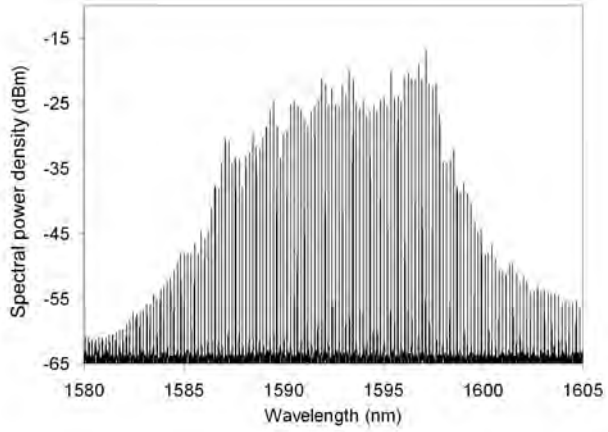

Figure 4.3.5 Lasing spectrum of the deeply etched FP QD laser for I = 300 mA and T = 12°C, (resolution 0.16 pm).

4.3.4 Ring laser results

A photograph of two realized compact QD ring lasers is presented in Figure 4.3.6. The deeply etched waveguides are visible as dark lines. The rings are 2.0 mm long. The bends have a radius of curvature which decreases adiabatically down to 100 μm in order to avoid offsets between straight and curved waveguides which can give rise to reflections. The length of such 90° bend is twice longer compared to a circular bend with offsets. The directional coupler is double-etched with the gap shallowly etched and the outer ridges deeply etched to increase the fabrication

tolerances [22]. The coupler is 200 μm long and the gaps vary from 0.9 to 1.2 μm in width resulting in output coupling efficiency between 25 and 50 %. The reflectivity of the cleaved facets of the output waveguides is reduced by the 7° angle and anti-reflection coating. The lasers have two separate electrical contacts, one for the rings and the directional couplers and another one for the two output waveguides. The electrical isolation sections which separate the ring from the output waveguides are 15 μm long under an angle of 45 degrees with respect to the waveguides.

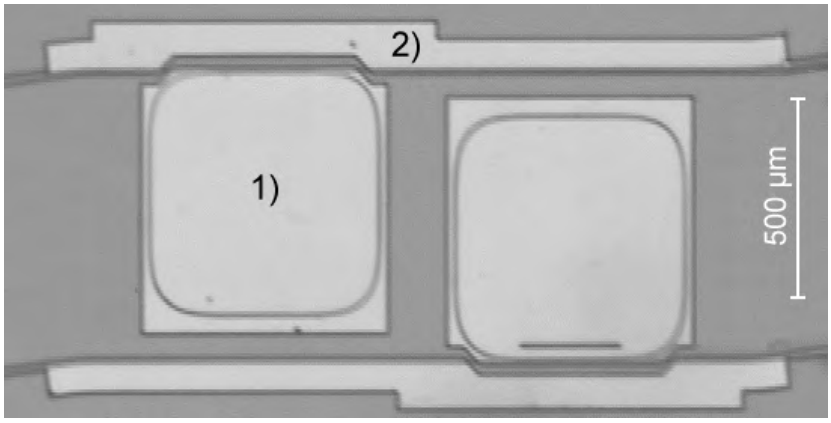

Figure 4.3.6 Top view of two QD ring lasers with two separate electrical contacts, 1) for the ring and the directional couplers and 2) for the output waveguides. The length of the rings is 2mm, the directional coupler gaps are 1.0 and 1.2μm.

In Figure 4.3.7 a), the total optical output power from the long and short output waveguides of the QD ring laser with a directional coupler gap of 1.2 μm is plotted as a function of ring current (I_{Ring}), for different current values in the output waveguides (I_{WG}). Operation is in CW mode at 12°C. The output powers are corrected for lensed fiber coupling and optical isolator losses. The total current for transparency of the QD gain material in the output waveguide is estimated at 3 mA [21]. The low absorption of the QDs allows for use of the ring laser without pumping the output waveguides. In unpumped FP lasers, an optical loss of 10 dB/cm ± 1dB around 1555 nm has been measured by injecting 1 mW from an EDFA broadband source. The presented light versus current (LI) curves are not linear above 10 mA pump current in the output waveguides. This is certainly due to the spontaneous emission generated in the output waveguides injected into the ring and maybe to an unperfect AR coating. In Figure 4.3.7 b) output powers are plotted from the two outputs separately as a function of I_{Ring} for I_{WG} = 5 mA. The laser is operating bi-directional; however, above 150 mA some power is transferred between the clockwise and counter clockwise modes [23]. The lasing spectra of the ring laser are similar to those of the FP lasers as shown in Figure 4.3.8 for I_{WG} = 0 mA, however, with 40 GHz mode spacing.

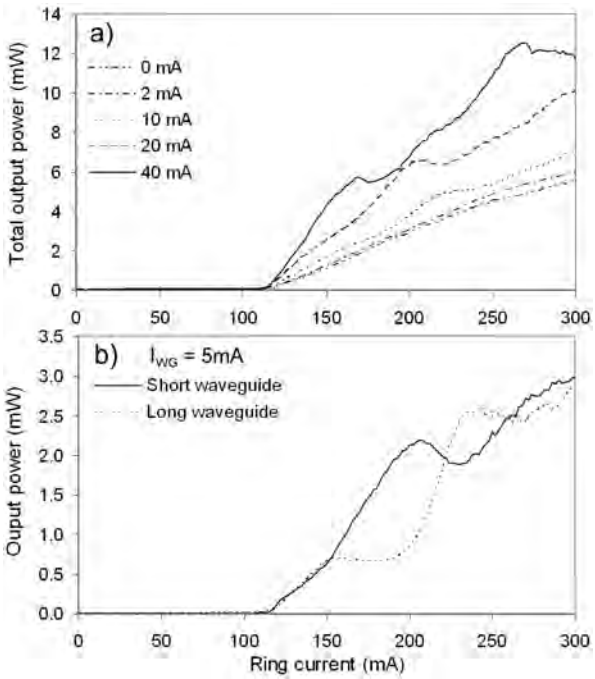

Figure 4.3.7: a) Total optical output power as a function of ring current for different output waveguides pump currents. b) Short and long output waveguides power as a function of I_{Ring} for I_{WG} = 5mA. The output powers are corrected for coupling and optical isolator losses. T = 12°C. Directional coupler gap of 1.2 μm.

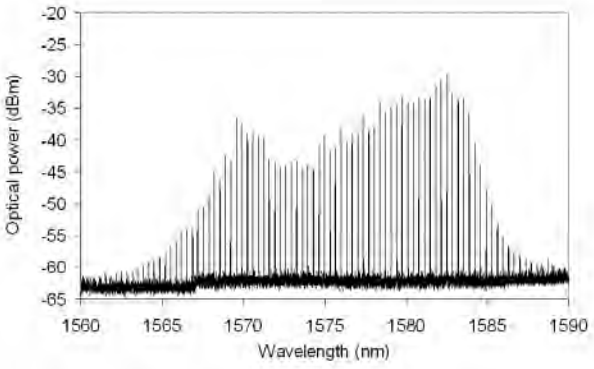

Figure 4.3.8 Lasing spectrum of the deeply etched QD ring laser for I_{Ring} = 300 mA, I_{WG} = 0mA and T = 12°C, (resolution 0.16 pm).

4.3.5 Conclusion

We have presented the results on quantum dot Fabry-Pérot and ring lasers employing narrow deeply etched waveguides (1.65 μm width) and lasing in the 1.55 μm range. We have observed that the performance of such lasers does not suffer from surface recombination of injected carriers. The deeply etched lasers have the same threshold current densities as shallowly etched ones and do not deteriorate with time. These observations show that more compact integrated photonic devices can be realized through the use of deeply etched bends with a small radius of curvature. This was demonstrated by the realization of small ring lasers. The measurements performed with unpumped output waveguides of the ring lasers, due to the low absorption and transparency current densities, reveal that quantum dot gain materials offer further increased flexibility for photonic integration for specific applications. Short sections of unpumped waveguides are easily bleached with limited power loss. One can consider the possibilities for integrating lasers, photodetectors and passive waveguides for interconnection, using the same layer stack and thus avoiding sophisticated active-passive integration technology.

4.4 List of references

1 Y. Barbarin, X.J.M. Leijtens, E.A.J.M. Bente, C.M. Louzao, J. Kooiman, M.K. Smit. "Extremely small AWG demultiplexer fabricated on InP by using a double-etch process" IEEE Photonics Technology Letters, Vol. 16, Issue 11, pp. 2478-2480, (2004)

2 Y. Barbarin, S. Anantathanasarn, E.A.J.M. Bente, Y.S. Oei, M.K. Smit and R. Nötzel "1.55 μm Range InAs/InP Quantum Dot Fabry-Pérot and Ring Lasers using Narrow Deeply Etched Ridge Waveguides" IEEE Photonics Technology Letters, Vol. 18, Issue 24, pp. 2644-2646, (2006)

3 M. K. Smit and C. van Dam, "PHASAR-based WDM-devices: Principles, design, and applications" IEEE Journal of Selected Topics in Quantum Electronics, Vol. 2, Issue 6, pp. 236–250, (1996)

4 H. Bissessur, P. Pagnod-Rossiaux, R. Mestric, and B. Martin, ``Extremely small polarization independent phased-array demultiplexers on InP," IEEE Photon. Technol. Lett., vol. 8, no. 4, pp. 554-556, Apr. 1996.

5 J.H. den Besten, M.P. Dessens, C.G.P. Herben, X.J.M. Leijtens, F.H. Groen, M.R. Leys, and M.K. Smit, ``Low-loss, compact, and polarization independent phasar demultiplexer fabricated by using a double-etch process," IEEE Photonic Technology Letters, Vol. 14, Issue 1, pp. 62-64, (2002)

6 Y.C. Zhu, F.H. Groen, D.H.P. Maat, Y.S. Oei, J. Romijn, and I. Moerman, ``A compact phasar with low central channel loss," in Proc. 9th Eur. Conf. on Integr. Opt. (ECIO '99), pp. 219-222, Torino, Italy, (1999)

7 C.G.P. Herben, "Compact integrated cross connects for wavelength-division multiplexing networks", PhD Thesis, ISBN 90-9014303-3, Delft University, December 2000,

8 D.F. Clark and M.S. Iqbal, "Simple extension to the Fabry-Pérot technique for accurate measurement of losses in semiconductor waveguides" Optic Letters, Vol. 15, Issue 22, pp. 1291-1293, (1990)

9 P.J. Harmsma, M.K. Smit, Y.S. Oei, M.R. Leys, C.A. Verschuren, and H. Vonk, ``Multi wavelength lasers fabricated using selective area chemical beam epitaxy," in Technical Digest Integr. Photon. Res. (IPR '99), pp. 17-19, Sta. Barbara, USA,(1999)

10 J.H. den Besten, R.G. Broeke, M. van Geemert, J.J.M. Binsma, F. Heinrichsdorff, T. van Dongen, E.A.J.M. Bente, X.J.M. Leijtens, and M.K. Smit, ``Compact digitally tunable seven-channel ring laser," IEEE Photonic Technology Letters, Vol. 14, Issue 6, pp. 753-755, (2002)

11 M.V. Maksimov, Y.M. Shernyakov, N.V. Kryzhanovskaya, A.G. Gladyshev, Y.G. Musikhin, N.N. Ledentsov, A.E. Zhukov, A.P. Vasil'ev, A.R. Kovsh, S.S. Mikhrin, E.S. Semenova, N.A. Maleev, E.V. Nikitina, V.M. Ustinov and Z.I. Alferov "High-power 1.5 μm InAs-InGaAs quantum dot lasers on GaAs substrates" Semiconductors, Vol. 38, Issue 6, pp. 732–735, (2004)

12 M. Sugawara, N. Hatori, M. Ishida, H. Ebe, Y Arakawa, T. Akiyama, K. Otsubo, T. Yamamoto and Y Nakata "Recent progress in self-assembled quantum-dot optical devices for optical telecommunication: temperature-insensitive 10 Gb s-1 directly modulated lasers and 40 Gb s 1 signal-regenerative amplifiers" Journal of Physics D: Applied Physics, Vol. 38 pp. 2126-2134, (2005)

13 S.A. Moore, L. O'Faolain, M.A. Cataluna, M.B. Flynn, M.V. Kotlyar, T.F. Krauss, "Reduced Surface Sidewall Recombination and Diffusion in Quantum-Dot Lasers" IEEE Photonics Technology Letters, Vol. 18, Issue 17, pp.1861-1863, (2006).

14 N.N. Ledentsov, M.V. Maximov, P.S. Kop'ev, V.M. Ustinov, M.V. Belousov, B.Ya. Meltser, S.V. Ivanov, V.A. Shchukin, Zh.I. Alferov, M. Grundmann, D. Bimberg, S.S. Ruvimov, W. Richter, P. Werner, U. Gösele, U. Heidenreich, P.D. Wang and C.M. Sotomayor Torres "Optical spectroscopy of self-organized nanoscale heterostructures involving high-index surfaces" Microelectronics Journal 26, pp.871-879 (1995)

15 D. Ouyang, N.N. Ledentsov, D.Bimberg, A. R. Kovsh, A.E. Zhukov, S.S. Mikhrin and V.M. Ustinov "High performance narrow stripe quantum-dot lasers with etched waveguide" Semiconductor Science and Technology, Vol. 18, Issue 12, L53-L54 (2003)

16 M Kuntz, G Fiol, M Lämmlin, D Bimberg, M G Thompson, K T Tan, C Marinelli, A Wonfor, R Sellin, R V Penty, I H White, V M Ustinov, A E Zhukov, Yu M Shernyakov, A R Kovsh, N N Ledentsov, C Schubert and V Marembert "Direct modulation and mode locking of 1.3 μm quantum dot lasers" New Journal of Physics, Vol 6, p. 181, (2004)

17 S.K. Ray, K.M. Groom, R.A. Hogg, H.Y Liu, I.R. Sellers, M. Hopkinson, T.J. Badcock, A.J. Ramsay, D.J. Mowbray and M.S. Skolnick "Growth, Fabrication, and Operating Characteristics of Ultra-Low Threshold Current Density 1.3 μm Quantum Dot Lasers" Japanese Journal of Applied Physics, Vol. 44, No. 4B, pp. 2520-2522, (2005)

18 H. Cao, H. Deng, H. Ling, C. Liu, V.A. Smagley, R.B. Caldwell, G.A. Smolyakov, A.L. Gray, Z. Laser, L.F. Lester, P.G. Eliseev, M. Osińskia "Highly unidirectional InAs/InGaAs/GaAs quantum-dot ring lasers" Applied Physics Letters 86, 203117 (2005)

19 E.A.J.M Bente and M.K. Smit, "Ultrafast InP optical integrated circuits", Proc. Photonics West 2006, Integrated Optoelectronic Devices, 21-26 January, San Jose, California, vol. 6124., (2006)

20 S. Anantathanasarn, R. Nötzel, P.J. van Veldhoven, F.W.M. van Otten, T.J. Eijkemans, and J.H. Wolter, "Stacking and polarization control of wavelength-tunable (1.55-μm region) InAs/InGaAsP/InP (100) quantum dots", Applied Physics Letters, Vol. 88, pp. 063105, (2006)

21 S. Anantathanasarn, R. Nötzel, P.J. van Veldhoven, F.W.M. van Otten, Y. Barbarin, G. Servanton, T. de Vries, E. Smalbrugge, E.J. Geluk, T.J. Eijkemans, E.A.J.M. Bente, Y.S. Oei, M.K. Smit and J.H. Wolter, "Lasing of wavelength-tunable (1.55-μm region) InAs/InGaAsP/InP (100) quantum dots grown by metalorganic vapor phase epitaxy", Applied Physics Letters, vol. 89, pp. 073115, (2006)

22 G. Griffel, J.H. Abeles, R.J. Menna, A.M. Braun, J.C. Connolly, M. King,"Low-threshold InGaAsP ring lasers fabricated using bi-level dryetching" IEEE Photonics Technology Letters, Vol. 12, Issue 2, pp. 146-148, (2000)

23 M. Sorel, G. Giuliani, A. Scire, R. Miglierina, S. Donati, P.J.R. Laybourn, "Operating regimes of GaAs-AlGaAs semiconductor ring lasers: experiment and model" IEEE JQE, 39, 10, 1187- 1195, (2003)

Chapter 5
Integrated modelocked lasers

5.1 Introduction

Semiconductor modelocked lasers (MLLs) are of interest for a large number of applications which are not restricted to optical telecommunication. For instance, the fastest sampling oscilloscopes currently employ MLLs for optical sampling measurements [1] and in the near future expectations are high for the use of MLLs in high speed analogue to digital conversion [2]. In microelectronics systems, the integration density in circuits is continuously becoming higher and the copper links between the components and sections are becoming so thin that their resistance and associated power loss becomes a problem. The use of MLL pulse sources to interconnect CMOS devices and/or to distribute clock signals in high speed microprocessors [3,4] is investigated by microelectronics companies. A well known medical application of MLLs is the use of Ti-sapphire femtosecond modelocked lasers for surgery in for instance corneal refractive surgery [5]. New medical applications emerging are in optical coherence tomography and multiphoton imaging where semiconductor MLLs can be used in the telecom wavelength range and up to GHz level repetition rates [6,7]. Closer to optical telecommunication, in radio over fiber applications, optical transmitters can make use of MLLs [8]. In this project, MLLs integrated on an InP chip have been developed. The final goal of these devices was their use as optical pulse sources in All Optical Clock Recovery (AOCR) [9] for application in Optical Time Division Multiplexing (OTDM) systems. The work has been largely concentrated on ring laser cavities. Indeed, much of the published research effort has been focused on monolithic modelocked lasers in Fabry-Pérot (FP) type configurations. A ring configuration has however significant advantages. Firstly, the repetition rate of the laser can be controlled accurately by photolithography as opposed to a device with cleaved facet mirrors. Secondly, a ring laser typically operates as a Colliding Pulse Modelocked (CPM) laser where two counter-propagating pulses collide in the saturable absorber. This improves the modelocking performance, in particular the stability. Furthermore, when active-passive technology is used the laser can be directly integrated with other devices such as an all-optical switch or a pulse compressor [10].

In this chapter, after a short description of the characterization setup used for all the measurements presented, different types of semiconductor MLLs fabricated and characterized are presented. The results from the all-active devices are presented first. Here the same active layerstack is used throughout the device. The results obtained from devices fabricated on active-passive wafers follow after that. Firstly, 20 GHz and 40 GHz linear all active Fabry-Perot MLL (FPMLL) lasers are presented in Section 5.3. Modelocking has been achieved with these lasers in the CPM and Self Colliding Pulse Modelocked (SCPM) configurations. Pulse lengths down to 1.6 ps (at 20 GHz) have been observed. A 40 GHz repetition rate was demonstrated in a CPM laser with a Saturable Absorber (SA) positioned in the center of the FP cavity. All these all active FPMLLs produce pulses with a time-bandwidth product slightly higher than 0.6, which is almost twice the transform limited value. The pulses are chirped. These results are presented in [11]. In the following section (5.4), results from all-active 15 GHz Ring-MLL (RMLL) are described in detail. These lasers show a relatively good timing stability due to the ring configuration. Measured output pulses are highly chirped and an FWHM bandwidth of up to 4.5 nm was obtained. These results have been published in [12]. Such lasers with high bandwidth pulses and compatible with active-passive integration are of great interest for Optical Code Division Multiple Access (O-CDMA) applications, where information is coded in the spectrum [13]. The goal of this work is to be able to realize modelocked lasers in the active-passive integration technology. In Section 5.5 passive modelocking has been demonstrated in integrated Extended Cavity FPMLLs with minimized intra-cavity reflections. Pulses of 2.1 ps duration and with a small pedestal have been observed. The pulses are almost transform-limited. The longer timescale dynamics of the EC-FPMLLs are reduced compared to the all-active FPMLLs, due to the short amplifier section. Finally, results from a 27 GHz RMLL are presented in Section 5.6. This first realization of modelocked lasers at COBRA used designs which were not optimal for intra-cavity reflections. These devices have been fabricated on active-passive wafer material fabricated at JDSU. Experimental results show that intra-cavity reflections make it difficult to reach a stable modelocked state. However in small windows of operation modelocked regimes have been observed and they are in line with theoretical results. This laser was the first integrated extended cavity passively modelocked ring laser using active-passive integration. These results have been published in [14]. Starting from these results, efforts have been undertaken for the minimization of all the intra-cavity reflections (Chapter 3). All these considerations are included in the new design of RMLL on active-passive wafers which is presented in Chapter 6.

5.2 The characterization setup

Optical spectra have been recorded using either an ANDO Optical Spectrometer Analyzer (OSA) which has a resolution of 50 pm or, when it became available, with a high resolution OSA (APEX AP2041A) which has a resolution of 0.16 pm (20 MHz). An EDFA has been commonly used for the amplification of the laser output in order to have sufficient power to measure modelocked laser output RF spectra and autocorrelator traces. Lasers of Section 5.3 have been amplified with an SOA since their lasing wavelength was just below the EDFA window. The RF spectra were recorded by a 50 GHz Agilent PSA E4448A spectrum analyzer. The photodetector used was either a 50 GHz u²t photodetector (XPDV 1020R) or if not available a 12 ps rise time IR photodetector (New Focus model 1024). The Single Side Band (SSB) phase noise spectra have been measured directly on the PSA spectrum analyzer using the phase noise measurements utility. Autocorrelator traces have been recorded using an APE "PulseCheck TC" autocorrelator.

All measurement results on the lasers presented here have been obtained using the same characterization setup. The chips have been fixed onto a small copper mount as shown in Figure 5.2.1. The chip temperature is controlled using a thermo electric controller. The Peltier cell is positioned under the small mount and cools (or heats) the chip mount. A thermistor in the copper mount records the mount's temperature. The electrical ground is connected to the copper mount as the lasers have been fabricated on n-type substrates. The current (or the voltage) is supplied to the devices through electrical probes (up to 3 for the ring laser of Section 5.4). The light from the lasers is coupled into optical fiber using a coated lensed fiber. It is then led to the optical instruments via an optical isolator. The alignment of the lensed fiber is realized using a 3 transverse axes nanoblock. In order to keep the alignment of the lensed fiber and chip stable for several hours, the large copper block below the Peltier cell was water cooled. When the chip is cooled below 15°C, the setup was covered by a Plexiglas box for better temperature stability.

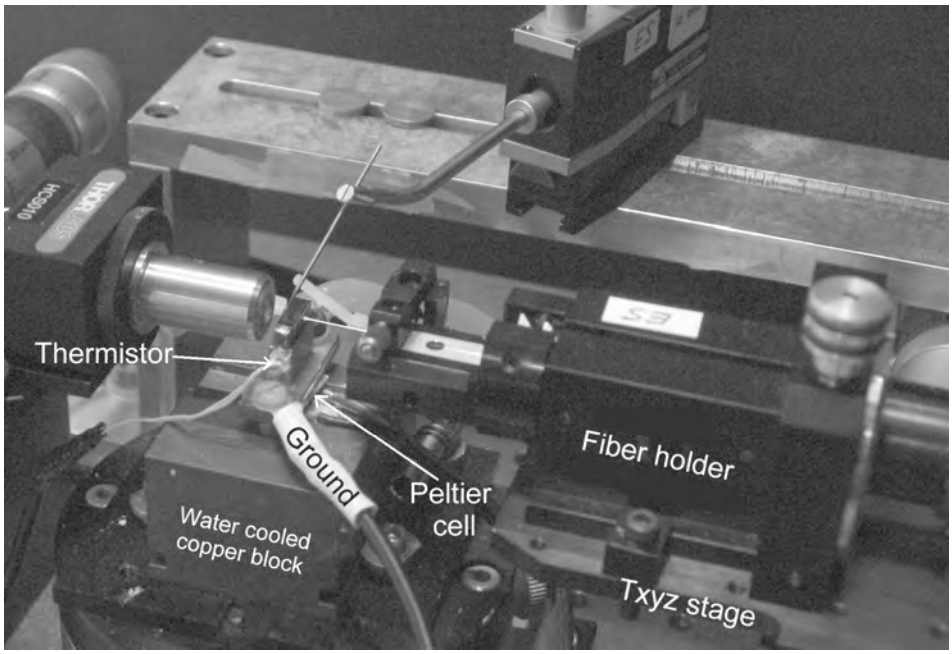

Figure 5.2.1 Photograph of the chip mounted on the setup.

5.3 All active integrated Fabry-Pérot passively modelocked lasers.

5.3.1 Introduction

In this section we report on two types of passively modelocked lasers using a 120 nm thick bulk 1.5 μm InGaAsP gain region. Modelocking is achieved using a short reversely biased section of the ridge waveguide as a Saturable Absorber (SA). The bulk InGaAsP active material layer stack is the same as the one used in our active-passive integration technology with low butt-joint loss and reflections (see [15] and Chapter 3). 20 GHz Fabry-Pérot SCPM lasers as well as 40 GHz Fabry-Pérot colliding pulse lasers were demonstrated using this active bulk material. Pulse lengths down to 1.6 ps have been observed from the 20 GHz device. These results showed that good modelocking can be achieved using bulk gain material and provided data on the dimensions that are to be used, in particular the SA. These experiments showed the way to design passively modelocked lasers in our Active-Passive integration scheme and integrate them with other devices such as an integrated pulse compressor [10].

5.3.2 20 GHz SCPM laser design and performance

The Figure 5.3.1 shows the Self Colliding Pulse Modelocked (SCPM) lasers fabricated with varying SA lengths at one side of the chip. A 2.0 μm wide and 1985 μm long straight ridge waveguide defines the laser channel after cleaving. The electrical isolation between SA and the amplifier is realized by a 15 μm long section where 500 nm of the top cladding have been etched (R = 150kΩ). Details of the fabrication have been presented in Chapter 3.

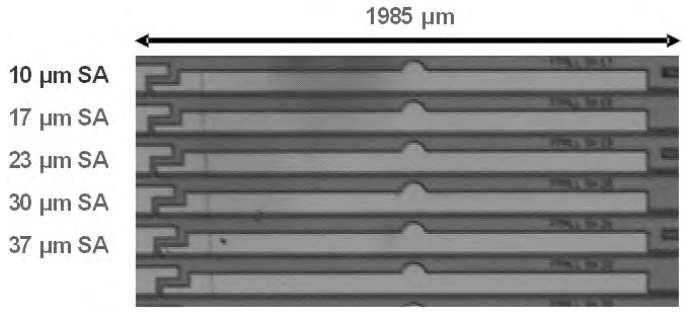

Figure 5.3.1 Top view picture of the 20 GHz FP MLL. The absorbers are on the side. Best results have been obtained from the 10 μm long SA.

The range of amplifier current and absorber voltage for which modelocking was obtained was largest for the shortest saturable absorbers (10 μm long). The range of these parameters for modelocked operation is continuously reduced with the

increase in absorber length. The SCPM with the 37 μm long absorber did not modelock. The different lasing regimes of the SCPM with the 10 μm SA are plotted in Figure 5.3.2. Modelocking is achieved over a continuous range of reverse bias voltages on the SA between 0.9 and 2.4 V and a range of amplifier currents between 110 and 125 mA. The evolution of the RF spectrum of the laser output versus the amplifier current at a reverse bias voltage on the SA is fixed at 1.8 V is presented in Figure 5.3.3. At 110 mA amplifier current, the RF peak at the fundamental frequency is 25 dB above the floor. However the laser output is dominated by a strong modulation (~800 MHz). In this region we interpret this modulation of a modelocked pulse train with a relaxation oscillation of the laser (see also Section 2.3.2), this is low dimension quasi-periodic dynamic [16]. In theoretical literature "proper" modelocked operation is identified when the height of the peak in the RF spectrum at the fundamental frequency is 25 dB above any other component in the RF spectrum below the fundamental frequency [17]. This is the case for the second RF spectrum plotted in Figure 5.3.3, the fundamental RF peak is 27 dB above the relaxation oscillation peak. For higher current values Q-switching is observed in the RF spectrum of the laser output, the peaks around the fundamental frequency are much widened. In fact, this region contains nonlinear dynamic regimes of different dimensions, but has not been studied for this device [18].

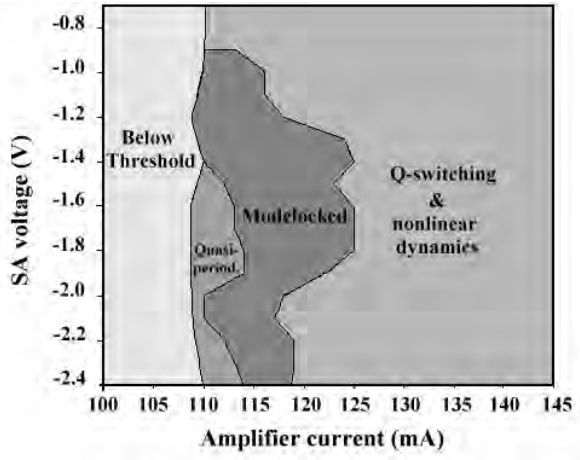

Figure 5.3.2 Modelocking regimes versus amplifier current and SA reverse voltage. Three regimes are observed.

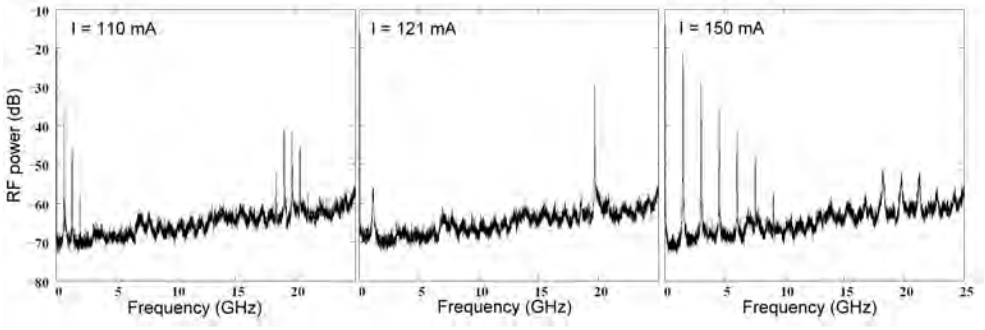

Figure 5.3.3 RF spectra for different amplifier current and for 1.8 V reverse voltage on the 10 μm long SA.

Short pulses down to 1.6 ps have been measured from this device. The corresponding RF spectrum for this working point is plotted in Figure 5.3.4. A 10 MHz wide peak (at – 20 dB) is visible at 19.65 GHz. The relaxation oscillation peak at ~1 GHz is 40 dB lower than the one at the fundamental frequency. The autocorrelator trace and the optical spectrum are plotted in Figure 5.3.5 a) and b). In the graph, the curve which is the envelope of the ideal transform limited optical spectrum has been added to the measured optical spectrum. The optical spectrum shows some extra components at the lower wavelengths. The time bandwidth product is 0.76 which means the pulses are chirped. For longer pulses (2-3 ps) the spectrum is symmetric and the time-bandwidth product is ~0.65. Depending on the settings, the MLL frequency is between 19.73 and 19.78 GHz. When the laser changes from the modelocked to a non modelocked state, we have observed in the RF spectrum a decrease of 50 MHz in the frequency of the peak near the free spectral range frequency. The roundtrip time of the laser cavity is slightly longer for a single pulse traveling in the cavity due to the reshaping effects it undergoes (see also Section 2.1.1).

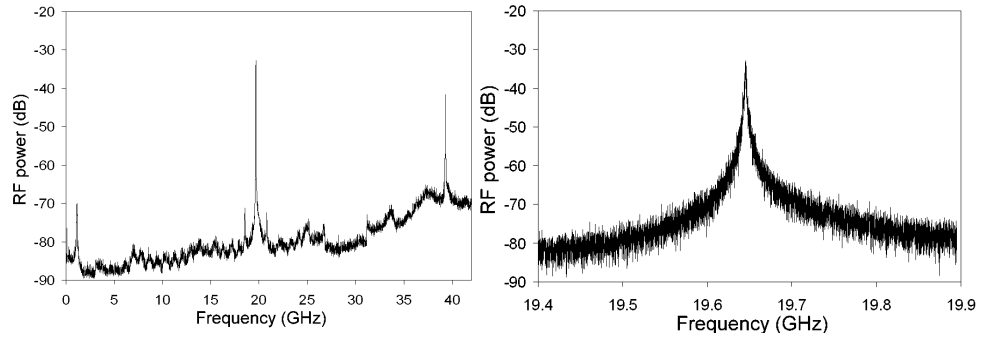

Figure 5.3.4 RF spectra for I_{amp} = 121.7 mA and V_{SA} = – 1.9 V on the 10 μm long SA. The RF peak is 40 dB above other components in the spectrum.

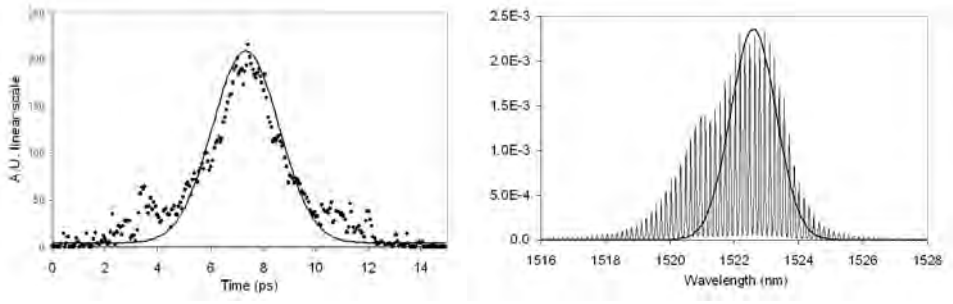

Figure 5.3.5 a) Autocorrelator trace and b) optical spectrum for I_{amp} = 121.7 mA and V_{SA} = – 1.9 V on the 10 μm long SA. The pulse is ~1.6 ps wide and the time-bandwidth product is 0.76. The transform limited ideal spectrum is shown as well.

5.3.3 40 GHz CPM laser design and performance

Colliding pulse modelocked (CPM) lasers were fabricated on the same chip as the 20 GHz SCPM lasers. The saturable absorbers are 20 or 40 μm long and positioned near the center of the cavity. From device to device the position of the SA is shifted by steps of 10 μm; it guarantees that we have one laser with a well centered SA. The two amplifiers have the same electrical contact and are optically coupled though the SA. The symmetry of the device is very important in order to obtain a large range op the operating parameters for modelocking in CPM lasers. Modelocking has not been achieved with the series of devices with the 20 μm long SA. But it has been achieved with the most symmetric device with the 40 μm long SA. A longer SA could be more tolerant for a small asymmetry, but still the modelocking range is limited. At high reverse bias voltages the MLL shows strong dynamics dominated by oscillations in the range of the relaxation frequency of the laser. The dynamics of the lasers under such conditions have been studied and a clear evidence of nonlinear dynamics and chaos in the integrated circuit has been demonstrated, this is the subject a publication [18].

Modelocking in the CPM device has been found for reverse bias voltages between 0.6 and 1.1 V. Pulses of 2.4 ps duration have been observed. In the RF spectrum of Figure 5.3.6 a) only a narrow peak at 39.75 GHz is visible. Looking in detail at that peak, it consists of two 5 MHz wide peaks spaced by 10 MHz. It is concluded that the laser operates with an overall intensity modulation at 10 MHz. The autocorrelator trace of Figure 5.3.6 b) shows well defined peaks spaced by 25 ps without background. Pulses down to 2.0 ps have also been measured with a higher reverse voltage on the absorber (V_{SA} = - 1.1V) however with some background.

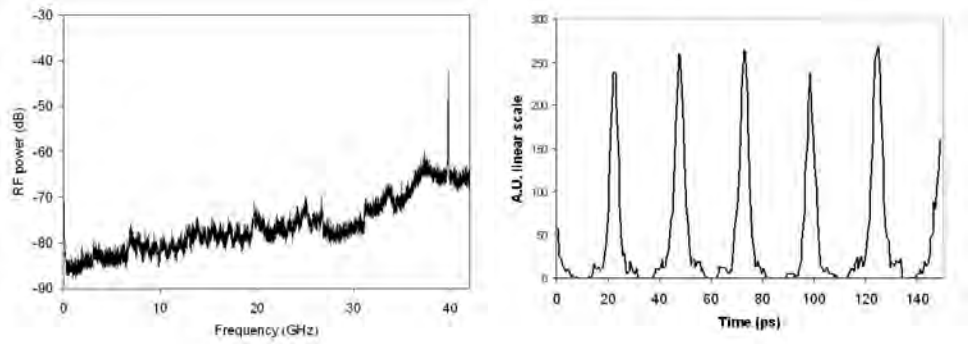

Figure 5.3.6 a) RF spectra and b) autocorrelator trace, for I_{amp} = 175.5 mA and V_{SA} = - 0.9 V on the 10 μm long SA. The pulses are ~2.4 ps wide.

5.4 All active 15 GHz integrated passively modelocked ring laser.

5.4.1 Introduction

The first monolithic modelocked semiconductor ring laser was reported by Hohimer and Vawter in 1993 [19]. The lasing wavelength of around 874 nm and 1.3 ps transform limited pulses at 86 GHz repetition rate have been reported. The output coupling used was a Y junction. Unfortunately, no RF spectrum of the laser output was reported. In 1998, Yu et al. [20] have reported on realizations of a number of designs of passively modelocked ring lasers using one or two Saturable Absorbers (SAs). Lasers were fabricated using double quantum well (DQW) GaAs/AlGaAs material. Their symmetric laser cavity where a single Saturable Absorber (SA) is exactly opposite the output coupler, showed approximately a two times smaller modelocked range than a symmetric device with two SAs and an asymmetric device using a single SA. In this thesis we mean by symmetric cavity, a cavity where the two counter propagating pulses experience the same optical path, but in opposite direction. Yu et al. attributed the poor performance of the symmetrical ring laser to the pulses colliding in the (active) MMI coupler. No RF spectra had been measured at that time, and the streak camera used had a resolution of 12 ps FWHM, which did not fully resolve the pulses. Avrutin et al. in 1999 reported the first results in passively modelocked InP/InGaAsP ring lasers [21]. Their design included two SAs as well in order to double the pulse narrowing effect of the CPM and to avoid the pulse collision in the gain section. Despite applying a range of biases to the absorbers sections, no modelocking at the fundamental frequency was observed. More recently Ohno et al. reported on a 30 GHz hybridly modelocked ring laser with integrated passive waveguides [22]. We have also reported in 2005 on a 27 GHz modelocked ring laser using active-passive integration [14]. The results from this laser are the subject of the Section 5.6. This device was passively modelocked but its operation suffered from internal reflections.

In this section we report on the most complete and detailed characterization of an integrated passively modelocked ring lasers reported up to now. After a description of the design, the modelocking regions are presented on a map of the amplifier current and the reverse bias applied on the SA. The modelocking operation is defined on the basis of the recorded RF spectra. The laser shows modelocked operation for a relatively large range of current and reverse biases on the SA. The RF peak linewidth of the modelocking states has been measured as well. The lasers show a relatively good timing stability for a passively modelocked device compared to Fabry-Pérot devices fabricated on the same wafer. Optical spectra have been measured at all the studied operating points; the optical bandwidth of the laser is wide at a high reverse bias voltage i.e. a 4.5 nm FWHM has been measured from one of our devices. Pulses that we measured are wide (5-8 ps) with regard to the available bandwidth, which means that the pulses are highly chirped. The range of tunability of the modelocked repetition rate is also presented. Finally jitter measurements have been performed on

the passively modelocked ring lasers. Such lasers with high bandwidth pulses and compatible with active-passive integration are of great interest for Optical Code Division Multiple Access (O-CDMA) applications [23].

5.4.2 Design of the all active 15 GHz ring laser

A photograph of two realized 15 GHz mode-locked ring lasers is presented in Figure 5.4.1. It shows the layout of the lasers. The ridge waveguides are 2 μm wide and are visible as dark lines. The ring is 5.291 mm long. In order to avoid any reflections that can occur, a number of measures have been taken in the design. The bends have their radius of curvature which decreases adiabatically down to a 500 μm in the middle of the curve, in order to avoid offsets between straight and curved waveguides which can give rise to reflections. The coupler is a 200 μm long directional coupler with a gap of 0.9 μm, this design was preferred to multimode interference coupler (MMI) also to avoid any reflection [24]. The coupler was designed to give ~35% of output coupling. Facet reflectivity is reduced using angled facets at 7° and an AR-coating. The design uses three metal contacts as indicated in Figure 5.4.1. The larger one contacts most of the ring and the directional coupler. The two output waveguides have their own electrical contact. Finally a short separate electrical contact connected to a larger pad is used for the SA. The SA lengths used are 30 or 60 μm. The electrical isolation sections that separate the different electrical contacts are 20 μm long and under a 45 degrees angle with the waveguide, furthermore part of the cladding (1200 nm) has been removed during the processing. The electrical isolation obtained between different contacts is 200 kΩ, which is more than sufficient.

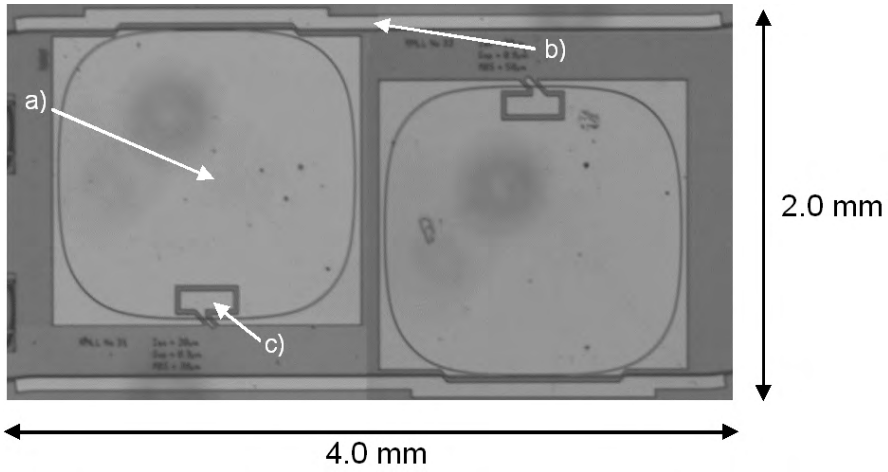

Figure 5.4.1 Top view of two realized 15 GHz modelocked ring lasers. Electrical contacts are indicated by arrows: a) the electrical contact of the ring and the directional coupler, b) the electrical contact of the two output waveguides and c) the small electrical contact of the Saturable Absorber. The total length of the ring is 5.291 mm.

For all the results presented here, the current of the two output waveguides has been kept at 140 mA. It is above transparency so there is a small amount of amplification but low enough for the ASE or reflections not to influence the behavior of the modelocked ring laser.

5.4.3 Modelocking region and RF spectra

The modelocking region has been delimited from the measured RF spectra. Two detailed observed RF spectra from the ring laser are presented in Figure 5.4.2 a) and b). In theoretical literature "proper" modelocked operation is identified when the height of the peak in the RF spectrum at the fundamental frequency is 25 dB above any other component in the RF spectrum below the fundamental frequency [17]. In this paper we also use this convention to identify proper modelocked operation of the laser. In addition to this we identify the laser as being imperfectly modelocked when the peak at the fundamental frequency is 25 dB over the noise floor, but does not satisfy the requirement for proper modelocking. In the spectrum in Figure 5.4.2 a) the peak at the fundamental frequency is 50 dB over the noise floor and 33 dB over the lower frequency signal intensity. In this situation the ring laser is thus properly modelocked. Next to the low frequency noise a small peak around 1 GHz is visible. It corresponds to the relaxation oscillation of the laser which is becoming dominant in Q-switching regimes at high current injection in the amplifier. A detailed view of the RF spectrum around the fundamental frequency (span of 250 MHz) is presented in Figure 5.4.2 b). The linewidth of the peak in the RF spectrum is 2.8 MHz at – 20 dB and less than 400 kHz at – 3 dB. For each measured point, the RF spectra have been recorded on a large span and short span. The parameter ranges for both modelocking regimes have been determined by scanning the amplifier current and absorber voltage and recording the RF spectra from the laser output. When the current is increased, the peak at the fundamental frequency slowly increases in intensity and gradually narrows down to a constant value for the properly modelocked states. At higher current values the transition from a modelocking state to a Q switching regime occurs abruptly. An animation of the evolution of the spectrum when scanning the amplifier current and keeping the SA voltage fixed at – 2.0 V is available in [12].

Modelocking is achieved for a range of reverse bias voltages on the SA between 0.9 and 2.2 V and a range of amplifier currents between 355 and 410 mA (3.3 kA/cm² and 4.9 kA/cm²). The parameter range for modelocked operation is presented in Figure 5.4.3. Here the intensity of the peak at the modelocking frequency in the RF spectrum is presented as a function of amplifier current and SA reverse voltage (device $L_{SA} = 40\ \mu m$). Operating points that show proper modelocking are represented in a grey scale in the graph. The imperfect modelocking are represented in black, the intensity of the peak is at least 25 dB over the noise floor but not above the other frequency components. For most of the detected modelocked states the peak at the fundamental frequency in the RF spectrum is higher than 40 dB above the noise floor. Figure 5.4.4 shows the width of the peak in the RF signal at 20 dB below its maximum for all recorded current and reverse bias voltage values. We have chosen a threshold of 20 dB, as we used a 16 kHz resolution, the discretization of the data

would be too much visible at the bandwidth at - 3 dB. For reverse bias voltages between 1.2 and 2.2 V and for operating points where the laser is properly modelocked, most of the measured –20 dB linewidths are between 2.5 and 5.5 MHz.

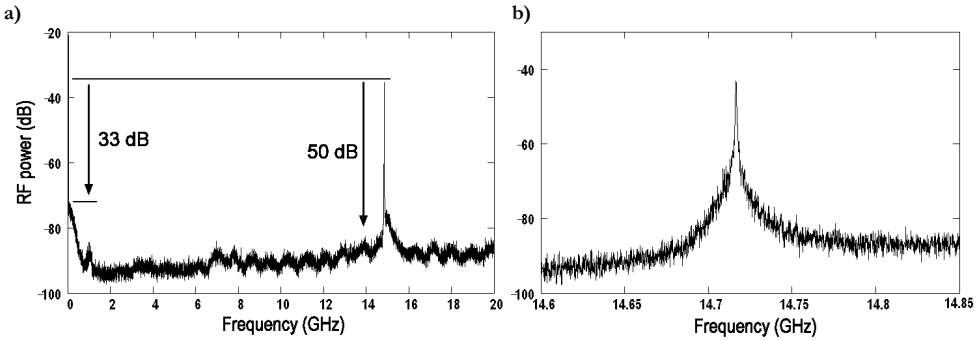

Figure 5.4.2 a) and b): measured RF spectra of the passively modelocked ring laser output (L_{SA} = 40µm, I_{WG} = 140 mA, I_{amp} = 389mA, V_{SA} = – 2.0V).
a) Span 20 GHz / Res. 200 kHz
b) Span 250 MHz / Res. 16 kHz

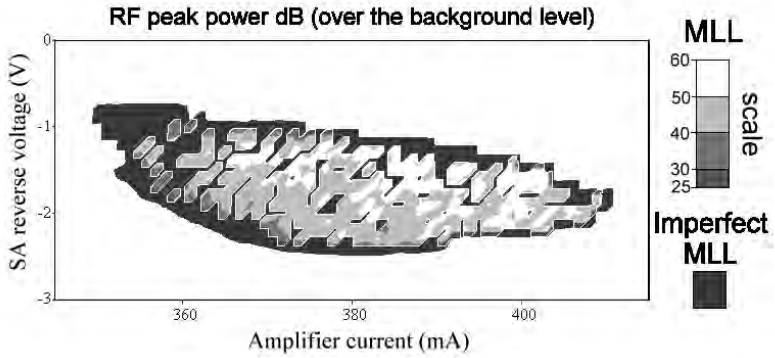

Figure 5.4.3 The intensity of the peak in the RF spectrum at the fundamental frequency as function of amplifier current and SA reverse voltage. Only peaks higher than 25 dB above the noise floor are plotted. The proper modelocking states are indicated with a color scale and the imperfect modelocking states in a grey scale. (L_{SA} 40 µm, I_{WG} = 140 mA).

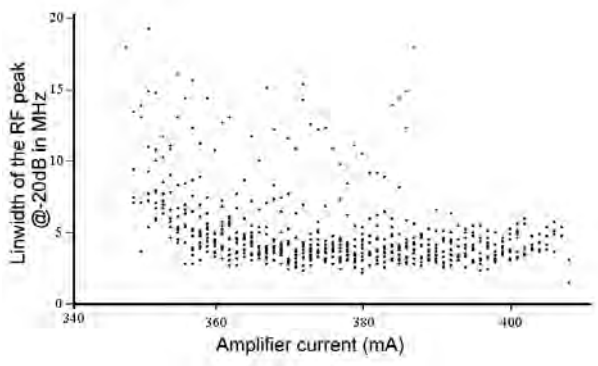

Figure 5.4.4 RF peak full linewidth in MHz at -20dB as a function of amplifier current for different values of the SA reverse bias voltage. (L_{SA} = 40µm, I_{WG} = 140 mA). Color version available in [12]

5.4.4 Output power of the RMLL

The power of both outputs of the ring laser (corrected for coupling and isolator losses) are plotted in Figure 5.4.5 a) and b) as function of amplifier current and SA reverse bias voltage. In Figure 5.4.5 c), the sum of the power from the two outputs is plotted. The common current supply of the two output waveguides is kept at 140 mA. No hysteresis has been observed at the laser threshold. The laser starts lasing at 338 mA and at 347 mA for an applied reverse bias voltage on the SA of respectively 0.8 V and 2.5 V. Figure 5.4.5 d) shows the output power levels in the two directions at – 1.8 V on the SA in detail. The ring laser operates CW in both directions below and within the current range where the laser is modelocked. Increasing the current further from the modelocking regime, depending on the reverse bias voltage on the SA, the ring laser enters a self-pulsating regime. The transition into the modelocked state from the lower current values is almost not visible on the output power curves. Knowing the transition from the modelocking to the Q-switching state from the evolution of the RF spectra, one can notice a small asymmetry in both output power levels from the laser.

The larger current range, for which the ring laser stays operating with the same output power in both directions, is at a reverse bias voltage of 1.9 V on the SA. For all measured SA voltages, the transition where the symmetry in lasing direction is broken is very clear in the graphs a), b) and c). Actually this transition might be explained by differences in either in feedback from the end facets [25] or Amplified Spontaneous Emission (ASE) from the two pumped output waveguides injected into the laser cavity, or a combination of these effects. These output waveguides differ in length by a factor of four (see Figure 5.4.1). From 0.8 V to 1.9 V reverse bias voltage on the SA, a possible explanation would be that the ASE of the long output waveguide coupled into the ring laser cavity is more intense and makes the laser operating almost uni-directionally. For reverse bias voltages of 1.9 V to 2.5 V on the SA, the situation is

more complex and no obvious explanation is available. For any reverse bias voltage on the SA, above 445 mA laser injection current, the situation becomes more complicated; intermittent switching of the lasing direction in the ring is observed.

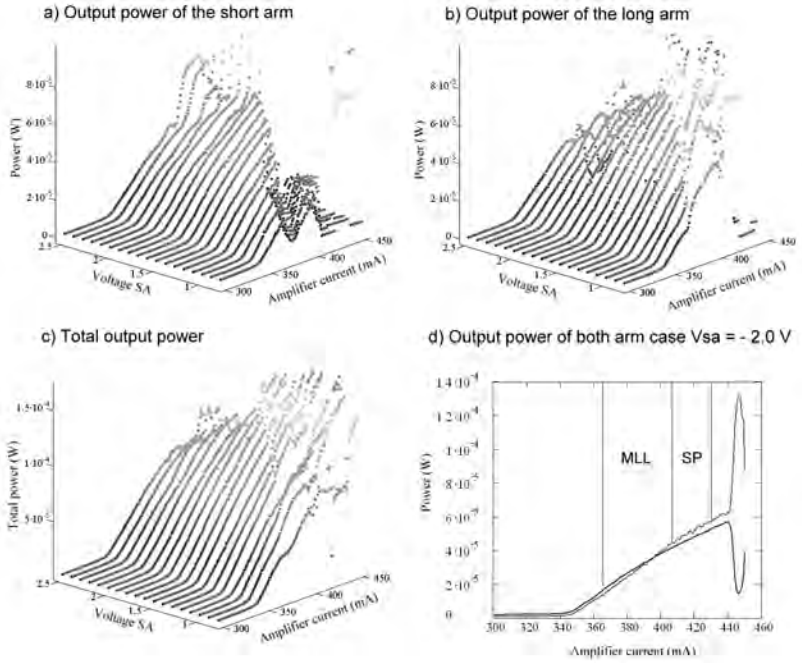

Figure 5.4.5 RF Output power levels as a function of amplifier current and SA reverse bias voltage for a) the short output waveguide (left in Figure 5.4.1) and b) the long output waveguide (right in Figure 5.4.1). In c) the sum of both output powers is presented. In d) the output power levels of both waveguides at a reverse bias voltage of 2.0 V is given to show the behavior in more detail.

5.4.5 Optical spectra of the RMLL

A typical example of an optical spectrum of a ring laser in a modelocked state is plotted in Figure 5.4.6 b). The spectrum is smooth and wide (4 nm FWHM). The shape is not symmetric, more modes are active at the lower wavelength side of the peak. The linewidth of a lasing mode is typically around 600 MHz. The evolution of the optical spectrum versus the amplifier current is the following for a reverse voltage of 2.0 V on the SA. The laser starts lasing at 340 mA. The ring laser operates CW in both directions up to 364 mA before modelocking. The spectrum is not uniform as seen in Figure 5.4.6 a). The transition is clearly visible in the spectrum; the top of the optical spectrum becomes more rounded like in Figure 5.4.6 b). If the current is increased further, the laser stays modelocked until 408 mA in the case presented. The transition to from the modelocked state to a Q-switching state is smooth and not visible in the optical spectrum but well visible in the RF spectrum. Between 408 and

428 mA the modelocking deteriorates and shows oscillations around 1 GHz. The deterioration is visible on the optical spectrum in Figure 5.4.7.a) for I_{amp} = 420 mA. Above 428 mA the evolution of the spectrum can be interpreted as that the gain curves of the amplifier and absorber shift away from each other at high current, making the laser to become unstable Intermittent switching of the lasing direction in the ring is observed above 445 mA Figure 5.4.7.b).

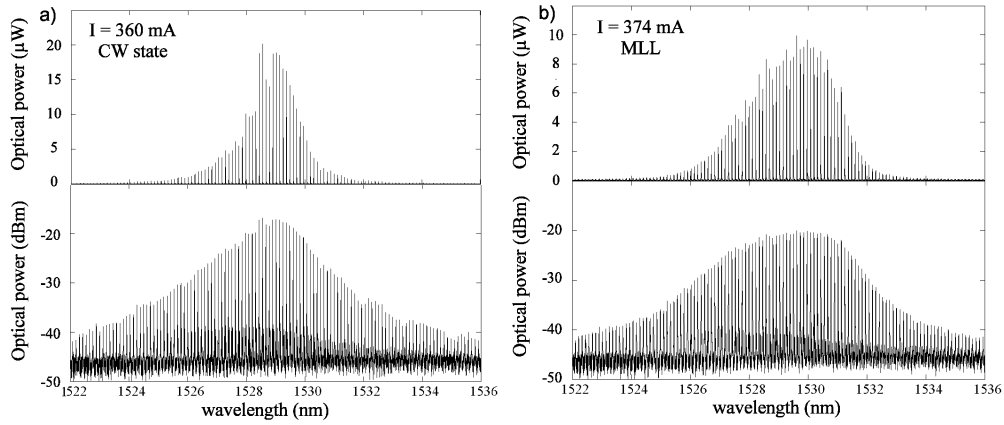

Figure 5.4.6 a) and b). Optical spectrum in linear and dB scales of a ring laser in a) a CW state at I_{amp} = 160mA and b) in a modelocked state at I_{amp} = 374 mA (L_{SA} = 40 μm, I_{WG} = 140 mA V_{SA} = – 2.0 V). The spectral resolution used was 0.80 pm.

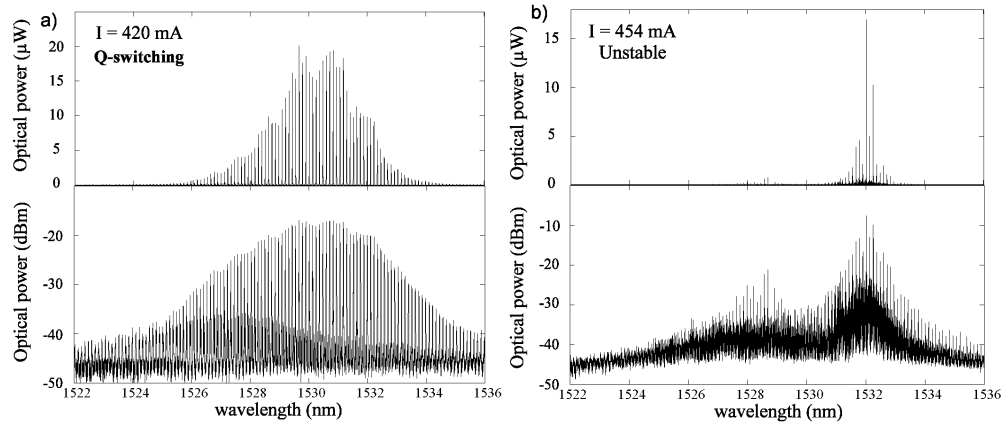

Figure 5.4.7 a) and b) Optical spectrum in linear and dB scales of a ring laser in a) a Q-switching state for I_{amp} = 420 mA and b) a unstable state for I_{amp} = 454 mA. (L_{SA} = 40 μm, I_{WG} = 140 mA V_{SA} = – 2.0 V). The spectral resolution used was 0.80 pm.

The FWHM of the optical spectrum of the laser is plotted in Figure 5.4.8 as a function of the amplifier current and SA reverse bias voltages. Only the operating points that show good or imperfect modelocking, delimited in Figure 5.4.3, are plotted.

One can clearly see that the bandwidth increases with the reverse bias voltage and thus with absorption, but only up to a certain point. Above that point the modelocking deteriorates and the bandwidth reduces as well. This can be attributed to a change in absorption or a mismatch in spectrum between the absorber and amplifier due to the increasing electric field strength in the absorber. In the case of the 40 μm long SA, for V = – 2.3 V the bandwidth does not exceed 3.5 nm. The largest bandwidth recorded was 4.5 nm from the device with the 50 μm long SA.

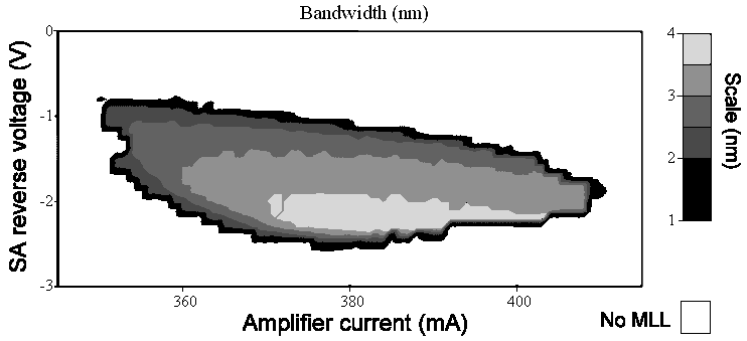

Figure 5.4.8 Optical bandwidth (FWHM) of the laser output as a function of amplifier current and SA reverse bias voltage for the modelocked states of the laser. For L_{SA} = 40μm, I_{WG} = 140 mA.

5.4.6 Autocorrelator results

The measured optical spectrum would support pulses down to 700 fs if the laser would produce transform limited pulses. However, the autocorrelator reveals long pulses (5-8 ps) with sharper peaks on top and a clear zero level in between. An example of an autocorrelator trace is plotted in Figure 5.4.9 for the device with a longer SA (50μm). The shape of the autocorrelator trace indicates there is an issue with the dispersion in the fibers used in the setup and/or a chirp on the pulses. The peaks on the top of the pulses are not coherence peaks but they are due to a partial compression of the pulse [26]. The output pulses are highly and nonlinearly chirped. This was shown by filtering the laser output with a 1.0 nm bandwidth filter before leading it to the autocorrelator. In this situation the autocorrelation showed 7.5 ps pulses without sharp peaks on top of the pulses. Adding 8 meters of standard single mode fiber the pulse could be compressed down to just over 4 ps which is approximately two times over the bandwidth limit. We suspect that the non-linearity of the chirp is linked to the colliding pulse regime and the very long all active laser cavity with a high confinement factor (0.28) in the bulk gain material. The transition from the modelocking regime and the Q-switching one is almost not visible on the autocorrelator traces.

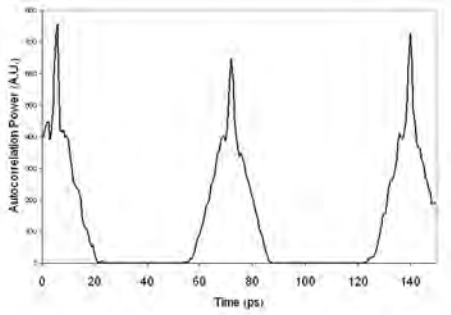

Figure 5.4.9 Autocorrelator traces of the ring laser with L_{SA} = 50 μm, I_{WG} = 145 mA V_{SA} = - 1.6 V I_{amp} = 450 mA. The shape of the peaks is caused by the highly chirped output pulses.

5.4.7 Repetition rate

The repetition rates have been recorded for all the modelocked states (good and imperfect). The repetition rate as a function of amplifier current and SA reverse bias voltage is plotted in Figure 5.4.10. The total range of tuning is 60 MHz. As described by Arahira and Ogawa in [27] the tuning is led by the gain/absorption saturation effects. Changes in refractive index are not sufficient to cover such a range. According to the explanation of Arahira and Ogawa, the presented device operates with a low unsaturated gain and in such a case the repetition rate decreases with increasing pulse energy. The pulse energy increases with the amplifier current thus the repetition rate decreases. Increasing the reverse bias voltage on the SA decreases the pulse energy, as a consequence the repetition rate increases.

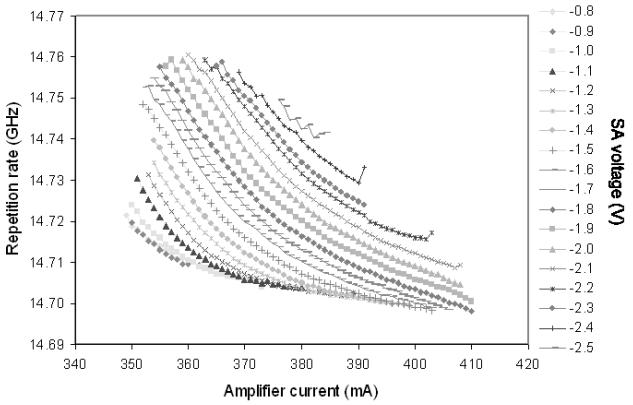

Figure 5.4.10 Repetition rate in GHz as a function of amplifier current and SA reverse bias voltage. (L_{SA} = 40 μm, I_{WG} = 140 mA).

5.4.8 Jitter measurements

No measurements of the timing jitter are reported in literature for modelocked ring lasers. In literature only a limited number of measured jitter values are available on passively and hybridly modelocked Fabry-Pérot lasers. Jitter values reported for passively modelocked lasers are typically higher than 8 ps [28, 29, 30, 31, 32, 33]. Details of the measured values are listed in Table 5.4.1 .The range of integration over the phase noise signal is not always the same or even indicated in many publications. A reduction of the timing jitter value by a factor greater than two has been demonstrated in [32] by using an integrated External Cavity Laser (ECL). The reduction in length of active waveguides has two positive effects. It first reduces the nonlinear phenomena in the amplifier (dispersive effects and total amount of carriers) thus the pulses width. It decreases as well the total amount of Amplified Spontaneous Emission (ASE) and carrier dynamics which are the main sources of timing jitter in a passively modelocked laser [34].

A recent paper [33] of Ji et al. reports a low value of 3.6 ps (range of integration: 20 kHz – 80 MHz) in free running mode for a colliding pulse modelocked laser (MQW) with two integrated extended passive waveguides. Colliding pulse modelocked (CPM) lasers provide a deeper saturation of the SA and a more effective pulse narrowing compared to a conventional modelocked laser design with the absorber at one side of the FP cavity. An important technological issue with a linear CPM design is that the absorber needs to be very precisely in the middle of the cavity which is difficult to achieve with cleaved facets. Our symmetric ring MLL is a CPM due to its bidirectional operation. The advantage of the ring is that the alignment of the SA in the middle of cavity is lithographically controlled and therefore much easier compared with the cleaved devices. The Single Side Band (SSB) [35] phase noise spectrum is plotted in Figure 5.2.1. Timing jitter values obtained from our ring lasers for a number of ranges of integration of the phase noise are listed in Table 1 for a good operating point (I_{amp} = 369 mA, V_{SA} = – 1.8V). There is no ITU recommendation for 15 GHz, the integration ranges of the phase noise used are the ones for 10 GHz. We have measured for the 20 kHz – 80 MHz range a timing jitter of 7.1 ps, which is low for an all-active device using bulk material. Furthermore a sizeable 3.0 to 4.5 nm bandwidth is available.

Table 5.4.1 Summary of the jitter measured reported on passively modelocked Fabry-Pérot lasers

Ref	Timing jitter value (ps)	Range for timing jitter calculation	Repetition rate (GHz)	Wavelength (nm)
[28]	12.5 Integrated ECL 12.2 ECL	150kHz – 50 MHz	5.5	834
[29]	> 8 (hybrid detuned)	-	1.0	1320
[30]	> 8 (Hybrid low power)	-	10.68	1590
[31]	>10	-	10 and 20	1555
[32]	15 All Active 6 Integrated ECL	10 kHz – 10 MHz	7.6 AA 9.3 I-ECL	860
[33]	3.6 CPM + Integrated ECL	20 kHz – 80 MHz	10.3	1556
ML ring laser	1.46 7.06 3.18 3.32	100 Hz – 20 kHz 20 kHz –80 MHz 4 MHz – 80 MHz 80 MHz – 10 GHz	14.7	1530

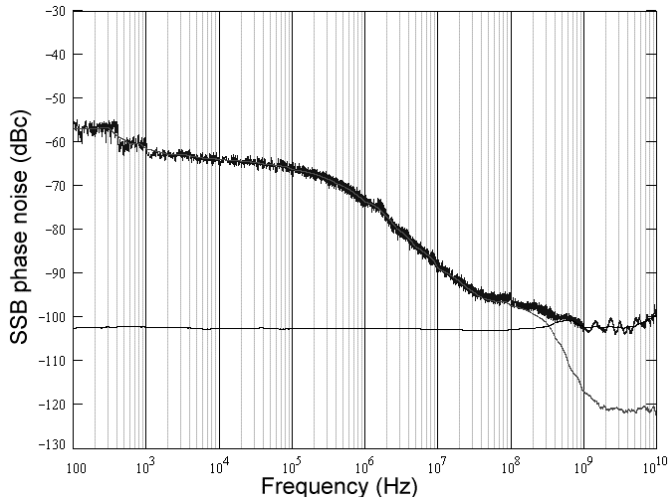

Figure 5.4.11 Single SideBand (SSB) phase noise spectrum corrected from the Displayed Average Noise Level (DANL). L_{SA} = 40μm, I_{WG} = 140 mA, I_{amp} = 369 mA, V_{SA} = – 1.8V.

5.4.9 Conclusion

In this section we have reported on the complete characterization of a 15 GHz integrated bulk InGaAsP passively modelocked ring laser at 1530 nm. The laser is modelocked for a wide range of current values in the optical amplifier and reverse bias voltages on the SA. The lasers show a relatively good timing stability for a passively modelocked device i.e. a 50 dB RF peak power with a linewidth < 400 KHz at -3 dB. We have measured for the 20 kHz – 80 MHz range a timing jitter of 7.1 ps, which is low for an all-active device using bulk material and in our opinion due to the ring configuration. Measured output pulses are highly chirped, a FWHM bandwidth is obtained of up to 4.0 nm for the device with a 40 μm long SA and even 4.5 nm for a 50 μm long SA. The repetition rate has a tuning range of 60 MHz. Such lasers with high bandwidth pulses and compatible with active-passive integration are of great interest for OCDMA applications [13] where information is coded in the spectrum.

5.5 Fabry-Pérot integrated extended cavity passively modelocked lasers

5.5.1 Introduction

In this section results from linear integrated extended cavity passively modelocked lasers (EC-MLL) are presented. The active-passive wafer on which the EC-MLLs were realized, is the one that showed very low butt-joint loss and reflections presented in [36] and Chapter 3. The SAs in these devices have been realized in a way that is different from all other devices presented in this chapter. A number of 18 GHz self-colliding pulse modelocked lasers have been demonstrated. Pulses with a length of 2.1 ps and with a small pedestal have been observed. The linear lasers presented here demonstrate that butt-joint active-passive integration developed at COBRA can be utilized for integrated modelocked lasers. Moreover, the pulses obtained are close to transform limited and the intensity modulations of the laser output in the range of the relaxation oscillation are significantly lower than the values observed in the all-active FPMLL of Section 5.3.2.

5.5.2 Design and fabrication of the EC-MLL

A photograph of four realized 18 GHz EC-MLL is presented in Figure 5.5.1. The devices have been realized starting from extended cavity Fabry-Perot lasers that have been fabricated in the active-passive integration technology. A chip containing 12 lasers was cleaved at a length of 2.2 mm and no coating has been applied. One of the cleaves was through the amplifier (active section). The other cleave went through the passive waveguides. The ridge waveguides are 2 μm wide and are visible as dark lines. The active regions are 30 μm wide, 750 μm long and are fully covered by the bright metal pads. The short SAs at the side of the FP cavity have been realized using a Focused Ion Beam (FIB) machine at Bristol University within the COST 288 frame work. The ion beam was used to etch away the metal layer and highly doped layers to create an isolation between two parts of the amplifier. By realizing the SA in this way, no extra mask was required and the SA lengths could be accurately controlled to vary from 5 to 17.5 μm. The electrical isolation sections that separate the SAs from the amplifiers are 15 μm long. Furthermore part of the cladding (400 nm) has been removed during the etching processing (see Figure 5.5.2). The electrical isolation obtained is 150 kΩ, which is more than sufficient. The waveguide in the EC-MLL cavities is not straight. The waveguide contains adiabatic bends to make the crossing of the butt-joints at varying angles. The original purpose of these devices was to study the effect of the different crossing angles [36] (Section 3.3.7). The minimum radius of curvature of the bends in the waveguide is 250 μm. No offset between straight and curved waveguides is used.

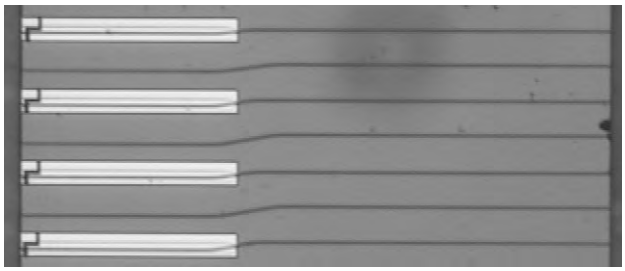

Figure 5.5.1 Top view of four realized 18 GHz integrated extended cavity modelocked lasers. The active regions are covered by the bright metal pads. The short SAs at the left hand side of the FP cavity have been fabricated using a Focused Ion Beam (FIB) machine. One can see that the butt-joints are crossed at different angles.

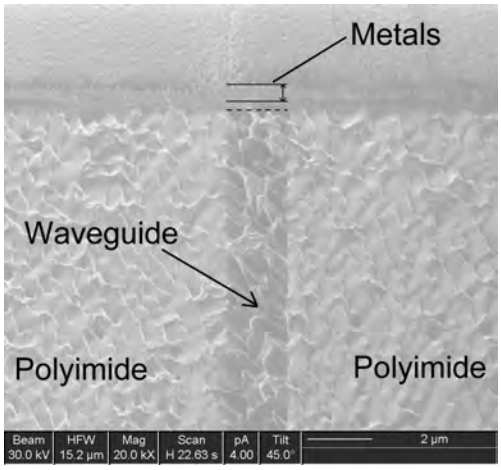

Figure 5.5.2 Focused Ion Beam (FIB) picture of a realized isolation between an amplifier and a saturable absorber. The metal layers of the electrical contact and part of the top cladding are etched away. Isolation obtained is >150 KΩ.

5.5.3 18 GHz EC-MLL performance

The characteristics of each laser are listed in Table 5.4.1. Modelocking has been observed for the devices with a 10 and a 12.5 μm long SA. The device with a 15 μm long SA has a very limited modelocking region. The devices with a 5 and a 7.5 μm long SA did not modelock. The absorption was too low, a higher reverse voltage than 3.0 V could have been applied but the reverse current density (>20 kA/cm^2) would have damaged the SA. The device with a 17.5 μm long SA, either the SA is too long or it suffers from small internal reflections on the butt-joint, no modelocking has been observed.

Table 5.5.1: Characteristics of the extended cavity modelocked lasers

SA length in μm	5.0	7.5	10.0	12.5	15.0	17.5
Butt-joint angle in deg.	15	13	11	9	7	5
Reflection in dB	-53	-51	-49	-47	-45	-43
Modelocked	No	No	Yes	Yes	Limited	No

The largest modelocking region has been obtained for the 10 μm long SA device. It is modelocked continuously for a range of reverse bias voltages on the SA between 2.1 and 3.0 V and a range of amplifier currents between 144 and 162 mA. Two RF spectra of the laser output are plotted in Figure 5.3.1. Here the reverse bias voltage on the SA is fixed at 2.5V. Just above threshold the laser is in a quasi-periodic state (Figure 5.3.1.a). The RF peak at the fundamental frequency is 35 dB above the floor, but the laser behavior is dominated by strong amplitude modulation at frequencies below 1 GHz. It is interesting to compare those modulations to the low frequency ones recorded from all-active FPMLL devices (see Section 5.3.2 and Figure 5.3.3). Just above threshold the EC-MLL shows modulation of the output at a much lower frequency of ~150 MHz compared to approximately 1 GHz for the FPMLL output. The intensity of the peak at the fundamental frequency of the EC-MLL output is already quite high (40 dB over the noise floor), close to the value in the modelocked state. For the EC-MLL, at current values higher than those for the modelocked state, there is only a single low frequency component in the spectrum and two peaks separated by 150 MHz around the fundamental frequency (Figure 5.3.1.b). It corresponds to a quasi-CW regime with few longitudinal modes beating. Increasing further the current, the laser becomes more quiet. It demonstrates that the dynamics around the modelocking regime of the EC-MLL are reduced comparing to the all-active FPMLL [32]. This is due to the reduction of the reservoir of carriers in the EC-MLL from the FPMLL. Figure 5.3.4 shows the RF spectrum of an EC-MLL in a modelocked state. The peak at the fundamental frequency is 50 dB above the noise floor and 35 dB above the relaxation oscillation peak (~800 MHz). The peak is 10 MHz wide (at – 20 dB). The modelocked RF spectra are very similar to the ones of the all active FPMLL (see Figure 5.3.4).

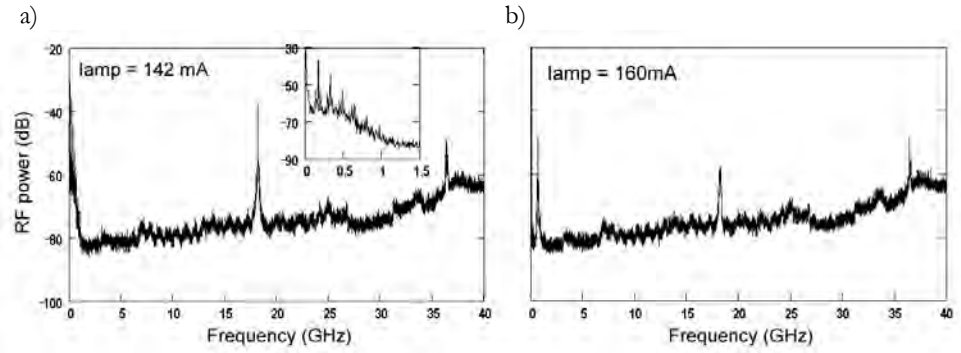

Figure 5.5.3 a) and b): measured RF spectra of the passively modelocked laser output (L_{SA} = 10 μm, V_{SA} = – 2.5V) in a) a quasi-periodic state and b) quasi-CW regime with few longitudinal modes beating

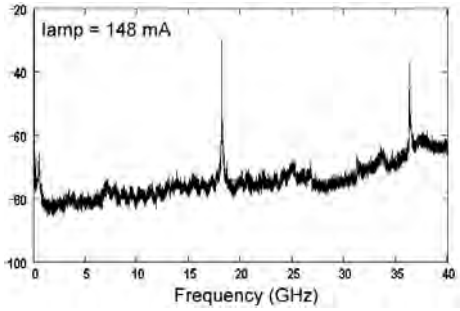

Figure 5.5.4 measured RF spectra of the passively modelocked laser output in modelocked state. (L_{SA} = 10 μm, I_{amp} = 148 mA V_{SA} = – 2.5V)

In the modelocked state, differences between the output pulses and the optical spectra of the EC-MLL and the FPMLL are clearly visible. An optical spectrum of the EC-MLL output is plotted in Figure 5.5.5 for I_{amp} = 148 mA and V_{SA} = - 2.5V. Plotted in a linear scale, it reveals extra components at both sides of central longitudinal modes. The spectrum is approximately 1.6 nm wide (FWHM) but the shape of the wings of the spectrum is obviously not Gaussian or sech² like. The corresponding observed autocorrelation trace is plotted in Figure 5.5.6. The autocorrelation shows pulses that are short with a considerable pedestal, but with a zero floor level between the pulses. In this condition, because of the pedestal, it is difficult to quantify with accuracy the length of the pulses from an autocorrelation. The estimated pulse length is ~2.0 ps FWHM. The time-bandwidth product for a transform limited pulse depends on the shape of the pulse (0.441 for a Gaussian pulse and 0.315 for sech² pulse). If it is assumed that the pulses from the laser are transform limited a pulse length and time-bandwidth product can be calculated from the

observed optical spectrum. This time-bandwidth product is found to be ~0.33. Using the measured pulse width and spectral width leads to a time-bandwidth product of 0.39. Since these two values are close to each other the observed pulses are not far from being transform limited.

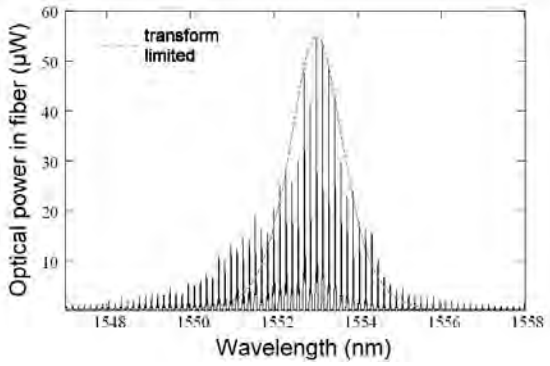

Figure 5.5.5 Optical spectrum in linear scale of an extended cavity laser in a modelocked state for I_{amp} = 148 mA, L_{SA} = 10 μm, V_{SA} = – 2.5 V. Resolution used: 0.80 pm.

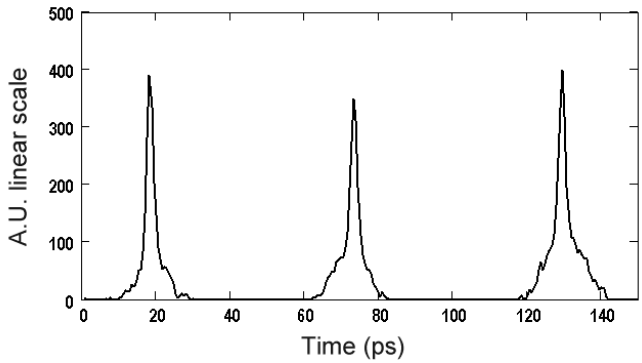

Figure 5.5.6 Autocorrelator trace of an extended cavity modelocked laser for I_{amp} = 148 mA, L_{SA} = 10 μm, V_{SA} = – 2.5 V.

5.5.4 Conclusion

Experimental results from these EC-FPMLL show that modelocked lasers can be realized using butt-joint active-passive integration. The intra-cavity reflections can be kept sufficiently low using a waveguide that crosses the butt-joint under an angle. The fabrication of SAs using a FIB did not create problems for the device. It allows for accurate control of the SA length in a cavity with cleaved mirrors. Comparing the experimental results of the EC-FPMLL with the all-active devices that were presented in Section 5.3.2, a smaller time-bandwidth product is observed from the EC-FPMLL. Furthermore the dynamics outside the modelocking operating region are reduced. In fact, due to the shorter amplifier of the EC-FPMLL, it operates at one and a half to two times higher carrier density compared to the all-active FPMLL. Therefore, the effective differential gain will be smaller (see Figure 2.2.1) and this leads to reduced Self-Phase Modulation (SPM).

5.6 27 GHz integrated passively modelocked ring laser

5.6.1 Introduction

In this section we present the first integrated extended cavity passively modelocked ring laser using active-passive integration and its modeling. The modelocked ring laser is fabricated on an active-passive wafer from JDSU and with a metallization scheme as described in [37]. This ring laser is one of the first series of MLLs that were fabricated [14]. Experimental results show that internal reflections are the major factor affecting operation stability. CW, self-pulsating and in small ranges of operating parameters, modelocked regimes have been observed. At the time, in that phase of the project, our model was at an earlier stage of development than the model described in Chapter 2. The model however predicted similar regimes as have been observed experimentally. The experimental and theoretical results are compared and discussed.

5.6.2 Modelocked laser device

A picture of the fabricated device is given in Figure 5.6.1, waveguides are visible as dark lines. To better understand the layout, one must remember that the positions and sizes of the active regions were predetermined through the re-growth process. The white bar at the bottom is the metallization of a 500 μm long amplifier. To realize a 30 μm saturable absorber a waveguide was positioned to cross at an angle the second active area. Light is coupled out from the ring cavity using a Multi-Mode Interference Coupler (MMI). For this design, the ring laser Free Spectral Range (FSR) could not be over 27 GHz due to the minimum ring length that could be fitted through the active regions. Deep and shallow etched waveguides were used in order to combine deep etched waveguides for small (100 μm) bending radii with low propagation loss in shallow waveguides. To reduce facet reflectivity, output waveguides (not visible in the Figure 5.6.1) are angled by 7° with respect to the facets normal and contain mode filters [38].

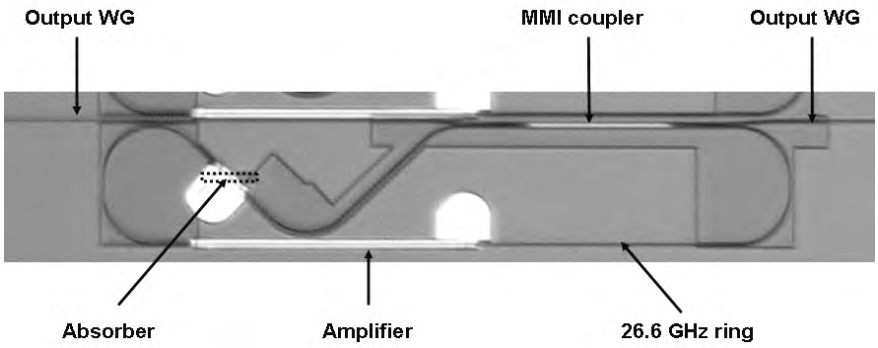

Figure 5.6.1 Photograph showing a top-view of the fabricated device.

5.6.3 Initial modelling of the modelocked ring laser

To simulate the performance of our device, as seen in Chapter 2 a numerical bidirectional model has been developed. The amplifier and the absorber are described using rate equations. For this design the ring is divided into 1500 segments that are equal in optical length. Every 25fs the photon densities (CW and CCW) and carrier densities are calculated for all segments. Then the photon densities are transferred to the next segments and the carrier density values are saved in active segments for the next step. A digital Bessel filter (14th order) simulates the gain bandwidth limitation. Equation are the same than in Chapter 2 but two photons absorption, spectral hole burning and carrier heating effects are not included. In the other hand small reflections ($2 \cdot 10^{-4}$) at the different active passive butt-joints interfaces Chapter 4 and [39] and at the MMI inputs [40] are included in the modeling.

The absorber is a short SOA that is reversely biased. It is described with the same rate equations as the amplifier without carrier injection. The carrier lifetime of the absorber depends on the reverse bias applied, but the relation has not been implemented in our model. Self-phase modulation effects and coherent effects in the absorber do not need to be included [41].

5.6.4 Experimental and simulation results

First experimental results of the modelocked ring laser showed that small reflections in the cavity have a large influence on the spectrum of the laser. Small reflections are expected at the active-passive interface and at the inputs of the MMI coupler. The spectrum varies significantly with temperature and current in the SOA due the small changes in the optical path length between reflection points. This makes the laser operating in very small operating windows.

Using the numerical model at its earlier stage, we have calculated the performance of the ring laser. A simulation of the self-starting laser is plotted in Figure 5.6.2. The model shows bidirectional operation of the laser like observed from the real device. The simulation starts with relaxation oscillations and modelocking sets in more slowly. The difference in intensity between the Clockwise (CW) and Counter Clockwise (CCW) output is determined by the order of the amplifier, absorber and output coupler in the cavity. A steady modelocked state is reached after 16 ns (450 roundtrips). As depicted in Figure 5.6.3, in our model a modelocked state is easily achieved for a wide range of parameters, as opposed to the experimental observations. However continuous wave (CW), self-pulsating and modelocking operation did show up in the experiments and in the simulations. We attribute this difference to not having included the self-phase modulation in the model and having fixed optical path lengths between reflections.

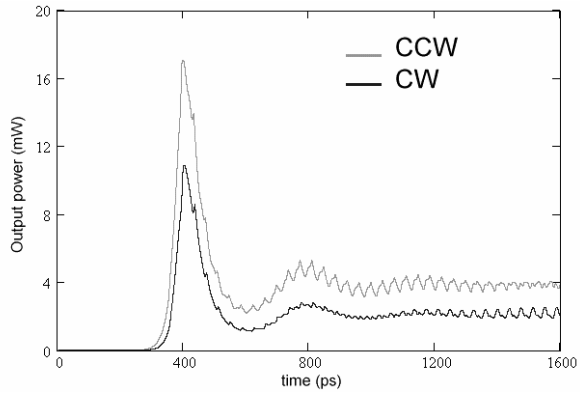

Figure 5.6.2 Simulation result of the self-starting MLL at I_{amp} = 140 mA and τ_{SA} = 20ps

According to the model the laser starts to be modelocked for an absorber carrier lifetime shorter than 30 ps. For a carrier lifetime over 14 ps and amplifier currents between 100 mA and 160 mA the model predicts stable modelocking with a pulse width between 3 ps and 8 ps. When the amplifier currents are above 180 mA the model shows self-pulsation. Below 11 ps absorber carrier lifetime the model predicts pulses shorter than 1 ps. We consider the model not to be valid in this region because of the approximations made.

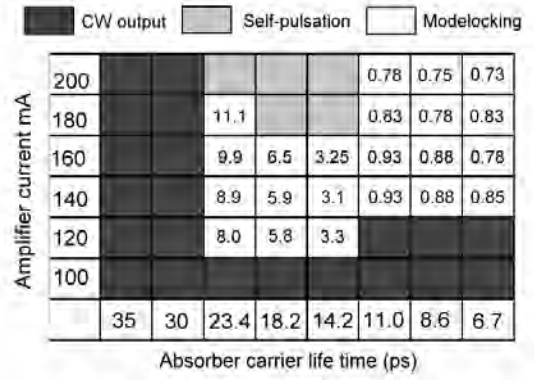

Figure 5.6.3 Simulated regimes of operation of the 27 GHz RMLL

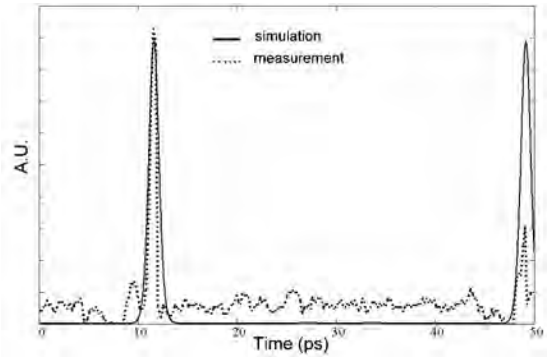

Figure 5.6.4 The simulated autocorrelation trace (I_{amp} = 160mA τ_{SA} = 11 ps), and the measured autocorrelation trace I_{amp} = 169mA V_{SA} = -2.1V

A pulse length close to 1 ps has been observed (Figure 5.6.4) when the laser was in an intermittent modelocked state for periods of one to a few seconds. This operating point was at the maximum current and maximum reverse bias voltage. Looking at Figure 5.6.3, the observation of 1ps at 169 mA agrees with the model for an absorber carrier life time between 14 and 11 ps. The instability is explained by the fact that we are close to the self pulsating regime. In Figure 5.6.4, the second measured pulse is not fully visible due to a limit of the autocorrelator. An operating point that was stable over 5 minutes has been found. We interpret it as a situation where the cavity contains 5 pulses with a 26.6 GHz modulation. The optical output spectrum is plotted in Figure 5.6.5. The RF spectra are in Figure 5.6.6. A strong peak (40 dB over the noise floor) that is narrow (2 MHz at – 20 dB) is observed at 26.6 GHz. This indicates modelocking. The spacing between most of the modes in the optical spectrum is 133 GHz, indicating there are five pulses in the cavity with a 26.6 GHz modulation over it. We attribute the generation of the five pulses to the intra-cavity reflections at the left butt-joint of the amplifier and the upper butt-joint of the absorber. The distance between these two reflections corresponds to one fifth of the cavity roundtrip time. We have attempted to recreate reproduce this regime in our model. A 5 pulses mode was found that was stable for 3 ns (80 roundtrips), but then one of the pulses became dominant and suppressed the other pulses.

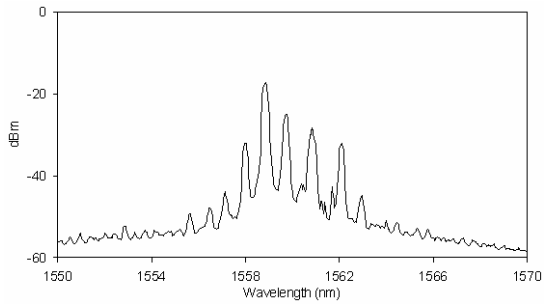

Figure 5.6.5 Optical output spectrum of the laser at I_{amp} = 167.5mA V_{SA}= - 2.0V.

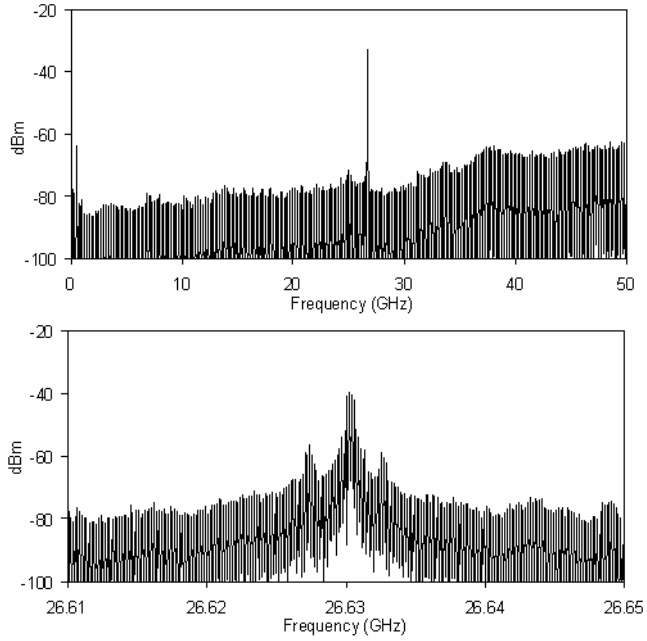

Figure 5.6.6 Measured RF-spectrum I_{amp} = 167.5 mA V_{SA} = - 2.0V (a) 3 MHz resolution and (b) 2 kHz resolution

Experimental results show that internal reflections are the major factor affecting operation stability of this device. In the following chapter a new design of an active-passive modelocked ring laser is presented. Special attention has been given to avoiding internal reflections using the experience gained with the all-active modelocked ring lasers and the extended cavity linear modelocked lasers.

5.7 List of references

1 M. Shirane, Y. Hashimoto, H. Yamada and H. Yokoyama, "A Compact Optical Sampling Measurement system Using Mode-Locked Laser-Diode Modules" IEEE Photonic Technology Letters, Vol. 12, Issue 11, pp. 1537-1539. (2000)

2 Y. Han, B. Jalali, "Photonic time-stretched analog-to-digital converter: fundamental concepts and practical considerations" Journal of Lightwave Technology, Vol. 21, Issue 12, pp. 3085-3103. (2003)

3 G.A. Keeler, B.F. Nelson, D. Agarval, C. Debaes, N.C. Helman, A. Bhatnagar, D.A.B. Miller, "The benefits of ultrashort optical pulses in optically interconnected systems", IEEE Journal of Selected Topics in Quantum Electronics, Vol. 9, Issue 2, pp. 477-485. (2003).

4 Kobrinsky, M.; Block, B.; Zheng, J-F.; Barnett, B; Mohammed, E.; Reshotko, M.; Robertson, F.; List, S.; Young, I.; Cadien, K. "On-Chip Optical Interconnects." Intel Technology Journal, Vol. 8, Issue 2, ISSN 1535-864X (May 2004).

5 T. Juhasz, F.H. Loesel, R.M. Kurtz, C. Horvath, J.F. Bille, G. Mourou, "Corneal refractive surgery with femtosecond lasers" IEEE Journal of Selected Topics in Quantum Electronics, Vol. 5, Issue 4, pp. 902-910, (1999)

6 J. Bewersdorf, S.W. Hell, "Picosecond Pulsed Two-Photon Imaging With Repetition Rates of 200 and 400 MHz", Journal of microscopy, Vol. 191, Issue 1, pp. 28-38, (1998)

7 W. Drexler "Ultrahigh-resolution optical coherence tomography" Journal of Biomedical Optics, Vol. 9, Issue 1, pp. 47-74 (2004)

8 A.J.C Vieira, P.R. Herczfeld, A. Rosen, M. Ermold, E.E. Funk, W.D. Jemison, K.I Williams, "A mode-locked microchip laser optical transmitter for fiber radio" IEEE transactions on Microwave Theory and Techniques, Vol. 49, Issue 10-2, pp. 1882-1887, (2001)

9 S. Arahira, Y. Ogawa, "Retiming and reshaping function of all-optical clock extraction at 160 Gb/s in monolithic mode-locked laser diode" IEEE Journal of Quantum Electronics, Vol. 41, Issue 7, pp. 937- 944, (2005)

10 M.J.R. Heck, E.A.J.M Bente, Y. Barbarin, D. Lenstra and M.K. Smit "Simulation and Design of Integrated Femtosecond Passively Mode-locked Semiconductor Ring Lasers Including Integrated Passive Pulse Shaping Components" IEEE Journal of Selected Topics in Quantum Electronics, Vol. 12, Issue 2, pp 265-276, (2006)

11 Y. Barbarin, E.A.J.M. Bente, M.J.R. Heck, Y.S. Oei, R. Nötzel and M.K. Smit "Passively Modelocked 20 and 40GHz Bulk InGaAsP Lasers" in Proceeding ECOC'05, Glasgow, Scotland, (2005).

12 Y. Barbarin, E.A.J.M Bente, M.J.R. Heck, Y.S. Oei, R. Nötzel and M.K. Smit "Characterization of a 15 GHz Integrated Bulk InGaAsP Passively Modelocked Ring Laser at 1.53μm" Optics Express, Vol. 14, Issue 21, pp. 9716-9727, (2006)

13 C. Ji, R. G. Broeke, Y. Du, Jing Cao, N. Chubun, P. Bjeletich, F. Olsson, S. Lourdudoss, R. Welty, C. Reinhardt, P. L. Stephan, and S. J. B. Yoo "Monolithically integrated InP-

based photonic chip development for O-CDMA systems" IEEE Journal of Selected Topics in Quantum Electronics, Vol. 11, Issue 1, pp. 66-77 (2005).

14 Y. Barbarin, E.A.J.M Bente, M.J.R. Heck, J.H. den Besten, G. Guidi, Y.S. Oei, J.J.M. Binsma, M.K. Smit, " Realization and Modeling of a 27-GHz Integrated Passively Mode-Locked Ring Laser", IEEE PTL, Vol. 17, Issue 11, pp. 2277-2279, (2005)

15 E.A.J.M Bente and M.K. Smit, "Ultrafast InP optical integrated circuits", Proc. Photonics West 2006, Integrated Optoelectronic Devices, 21-26, San Jose, California, vol. 6124. (2006)

16 Edward Ott, "Chaos in dynamical systems" Cambridge Univ. Press, ISBN: 0521811961, (1993)

17 U. Bandelow, M. Radziunas, A. Vladimirov, B. Hüttl and R. Kaiser. "40GHz modelocked semiconductor lasers: Theory, simulations and experiments" Optical and Quantum Electronics, Vol. 38, pp. 495-512, (2006)

18 M. Yousefi, Y. Barbarin, S. Beri, E. A. Bente, M. K. Smit, R. Nötzel and D. Lenstra, "New role for nonlinear dynamics and chaos in integrated semiconductor laser technology" Physical Review Letters. accepted for publication

19 J.P. Hobimer, G.A. Vawter, "Passive mode locking of monolithic semiconductor ring laser at 86 GHz" Applied Physics Letters, Vol. 63, Issue 12, pp. 1598-1600, (1993)

20 S. Yu, T.F. Krauss, P.J.R. Laybourn, "Modelocking in large monolithic semiconductor ring lasers" Optical Engineering, Vol. 37, Issue 4, pp. 1164-1168, (1998)

21 E.A. Avrutin, J.H. Marsh, J.M. Arnold, T.F. Krauss, H. Pottinger, R.M. De la Rue, "Analysis of harmonic (sub) THz passive mode-locking in monolithic compound cavity Fabry-Perot and ring laser diodes" IEE Proc. Optoelectronics, Vol 146, Issue 1, pp. 55-61, (1999)

22 T. Ohno, H. Ishii, S. Matsuo, H. Okamoto, Y. Kawaguchi, Y. Kondo, I. Furuta, H. Ito, Yoshikuni, Y. "Hybrid modelocking of semiconductor ring lasers incorporating passive deep-ridge waveguides" IEE Electronic Letters, Vol. 38, Issue 16, pp. 884-885, (2002)

23 Z. Jiang, D.S. Seo, S.D. Yang, D.E. Leaird, R.V. Roussev, C. Langrock, M.M. Fejer, A.M. Weiner, "Four-user, 2.5-Gb/s, spectrally coded OCDMA system demonstration using low-power nonlinear processing" Journal of Lightwave Technology, Vol. 23, Issue 1, pp. 143- 158 (2005)

24 E.C.M. Pennings, R. van Roijen, M.J.N. van Stralen, P.J. de Waard, R.G.M.P. Koumans and B.H. Verbeek "Reflection Properties of Multimode Interference Devices" IEEE Photonic Technology Letters, Vol. 6, Issue 6, pp. 715-718, (1994)

25 M. Sorel, G. Giuliani, A. Scire, R. Miglierina, S. Donati, P.J.R. Laybourn, "Operating regimes of GaAs-AlGaAs semiconductor ring lasers: experiment and model" IEEE Journal of Quantum Electronics, Vol 39, Issue 10, pp. 1187- 1195, (2003)

26 S. Gee, G.A. Alphonse, J.C. Connolly, C. Barty, P.J. Delfyett, "Ultrashort pulse generation by intracavity spectral shaping and phase compensation of external-cavity modelocked semiconductor lasers" IEEE Journal of Quantum Electronics, Vol 36, Issue 9, pp. 1035-1040, (2000)

27 S. Arahira, Y. Ogawa, "Repetition-frequency tuning of monolithic passively mode-locked semiconductor lasers with integrated extended cavities" IEEE Journal of Quantum Electronics, Vol 33, Issue 2, pp. 255-257, (1997)

28 J.D. Derickson, R.J. Helkey, A Mar, J.R. Karin, J.G. Wasserbauer and J.E. Bowers, "Short Pulse Generation Using Multisegment Mode-Locked Semiconductor Lasers" IEEE Journal of Quantum Electronics, Vol 28, Issue 10, pp. 2186-2202, (1992)

29 A.G. Weber, M. Schell, G. Fischbeck, D. Bimberg, "Generation of single femtosecond pulses by hybrid mode-locking of a semiconductor laser" IEEE Journal of Quantum Electronics, Vol. 28, Issue 10, pp. 2220-2229, (1992)

30 H. Yokoyama, T. Shimizu, T. Ono, Y. Yano "Synchronous Injection Locking Operation of Monolithic Mode-Locked Diode Lasers" Optical review, Vol. 2, Issue 2, pp. 85-88, (1995)

31 X. Wang, H. Yokoyama, T. Shimizu, "Synchronized harmonic frequency mode-locking with laser diodes through optical pulse train injection" IEEE Photonics Technology Letters, Vol. 8, Issue 5, pp. 617-619, (1996)

32 F. Camacho, E.A. Avrutin, P. Cusumano, A. Saher Helmy, A.C. Bryce, J.H. Marsh, "Improvements in mode-locked semiconductor diode lasers using monolithically integrated passive waveguides made by quantum-well intermixing" IEEE Photonics Technology Letters, Vol. 9, Issue 9, pp. 1208-1210, (1997)

33 C. Ji, N. Chubun, R.G. Broeke, J. Cao, Y. Du, S.J.B Yoo, K.Y. Liou, J.R. Lothian, S. Vatanapradit, S.N.G. Chu, B. Patel, W.S. Hobson, W.T. Tsang, "Synchronized Transform-Limited Operation of 10-GHz Colliding Pulse Mode-Locked Laser" IEEE Photonics Technology Letters, Vol. 18, Issue 4, pp. 625-627, (2006)

34 L.A. Jiang, M.E. Grein, H.A. Haus, E.P. Ippen, "Noise of mode-locked semiconductor lasers" IEEE Journal of Selected Topics in Quantum Electronics, Vol. 7, Issue 2, pp. 159-167, (2001)

35 Agilent Application note 1303 "5966-4008E Spectrum Analyzer Measurements and Noise"

36 Y. Barbarin, E.A.J.M Bente, T. de Vries, J.H. den Besten, P.J. van Veldhoven, M.J.H. Sander-Jochem, E.J. Smalbrugge, F.W.M.v. Otten, E.J. Geluk, M.J.R. Heck, X.J.M. Leijtens, J.G.M. van der Tol, F. Karouta, Y.S. Oei, R. Nötzel and M.K. Smit "Butt-Joint Interfaces in InP/InGaAsP waveguides with Very Low Reflectivity and Low Loss" IEEE LEOS Benelux 2005 Mons, Belgium

37 R.G. Broeke "A wavelength converter integrated with a discretely tunable laser for wavelength division multiplexing networks" Ph.D Thesis Delft Univ. of Tech. (2002) p.63

38 J. Leuthold, R. Hess, J. Eckner, P. A. Besse, and H. Melchior "Spatial mode filters realized with multimode interference couplers", Optics Letters, Vol. 21, pp 836-838, (1996)

39 Y. Barbarin, E.A.J.M. Bente, C. Marquet, E.J.S Leclère, J.J.M. Binsma and M.K. Smit. "Measurement of Reflectivity of Butt-Joint Active-Passive Interfaces in Integrated

Extended Cavity Lasers" IEEE Photonics Technology Letters, Vol. 17, issue 11, pp. 2265-2267, (2005)

40 D. Erasme, L.H. Spiekman, C.G.P. Herben, M.K. Smit, and F.H. Groen, "Experimental assessment of the reflection of passive multimode interference couplers" IEEE Photonic Technology Letters, Vol. 9, Issue 12, pp. 1604-1606, (1997)

41 D.J. Derickson, R.J. Helkey, A. Mar, J.R. Karin, J.G. Wasserbauer, and J.E. Bowers, "Short Pulse Generation Using Multisegment Mode-Locked Semiconductor Lasers" IEEE Journal of Quantum Electronics, Vol. 28, Issue 10, (1992)

Chapter 6
Modelocked lasers for all optical clock recovery

6.1 Introduction

High speed Optical Clock Recovery (OCR) is one of the key technologies for the realization of Optical Time Division Multiplexing [1,2] networks. Since more than a decade many techniques have been developed and nowadays very good clock signals, also at subharmonic frequencies, can be recovered from OTDM signals. The main requirement on the extracted clock signal is the timing jitter. For a 160 Gb/s clock the jitter value should 0.44 ps [2,3] or less. The techniques used can be divided in to two main categories. The first is based on Phase Locked Loops (PLLs) techniques [4] and uses opto-electronic conversion techniques and generally requires expensive high frequency electronics. The second category contains all-optical techniques. These techniques require less complexity and in principle no high speed electronics, and thus have the potential to reduce the cost significantly. To place the development of the all-optical techniques and work that will be presented here into context short overviews are given of the PPL and All-Optical Clock Recovery (AOCR) techniques.

A Phase-Locked Loop is a closed-loop feedback control system that generates and outputs a signal in relation to the frequency and phase of a reference input signal. A phase-locked loop circuit responds on the input signal by automatically raising or lowering the frequency of a controlled oscillator until it is matched to the reference. For optical clock recovery, the frequency of an electronic oscillator that controls the recovered optical clock, is itself controlled using an electronic signal derived from a phase sensitive comparison of the optical clock output and the optical input signal using an opto-electronic device. One of the first OCR experiments in a PLL scheme was using the Four Wave Mixing (FWM) mechanism in a traveling wave laser diode optical amplifier for the signal comparison by Kamatani et al. [5]. A 6.3 GHz has been

successfully recovered from a 400 Gb/s signal with a timing jitter value of 1.3 ps. The results were promising even if the timing jitter value of the recovered clock was too high to be used in applications. Better results have been obtained using an SOA in a loop mirror by Yamamoto et al. [6]. The Semiconductor Laser Amplifier Loop Mirror (SLALOM) is used as a phase comparator and 160 Gb/s OCR and demultiplexing down to 10 GHz has been presented with a timing jitter value of 0.27 ps. A more flexible concept, using a PLL by Tsuchida and Suzuki, was using an injected-locked optoelectronic oscillator on a 40 Gb/s signal [7]. An advantage of this system is its wide locking range. In literature, the largest number of reported PLL schemes utilised an Electro Absorption Modulator (EAM) [8,9,10,11]. Results obtained on recovery of up to 160Gb/s show low timing jitter values down to 0.20 ps, the locking range however is <10MHz. At a lower speed of 40 Gb/s down to 10 GHz, error free performance with no power penalty has been achieved by Lasri et al. [12].

For All Optical Clock Recovery (AOCR) there are a few concepts based on optical resonator of which the roundtrip time is used to define the clock frequency. A first AOCR scheme at 32.48 GHz has been reported by Yingmin Yang et al. using a single Fabry-Pérot (FP) laser cavity [13]. The data signal was injected into the FP laser. Its frequency needs to be close to the free spectral range of the FP laser. The injected power to the device is required to be > -5 dBm, however the locking range can be larger than 900 MHz. The timing jitter achieved is suitable (0.38 ps). In a similar concept from Contestabile et al. and Kehayas et al. [14,15], a Fabry-Pérot filter is followed by an SOA that is close to saturation by its optical input to filter out amplitude fluctuations. More recently a FP laser was used by Attygalle and Yang Jing Wen with an electronic feedback to achieve demultiplexing from 40 GHz to 10 GHz [16]. This also reduced the timing jitter down to 0.25 ps. The last scheme presented here to realize an AOCR, is also the most intuitive. The concept is to lock an optical pulse source to the incoming data signal through injection of the optical signal into the source. As a pulse source a Self Pulsating Distributed Feedback (SP-DFB) laser can be used. This device consists of at least an optical amplifier with a DFB tunable mirror at both ends. Such a device creates a sine modulated output from the beating of two of their longitudinal mode frequencies. The modulation frequency can be easily tuned changing the biasing conditions of the two DFB reflectors. Then the locking range can be very large (tens of GHz) by tuning the SP-DBR actively. Their performance has regularly improved over time, with an increase in the speed of the recovered clock up to 180 GHz [17,18,19,20,21]. In all cases, timing jitter values obtained so far are slightly below 0.5 ps, which is a bit to high for 160 Gb/s applications [2,3]. Finally AOCR can be achieved locking the signal to a modelocked laser [22,23,24,25,26,27]. It is this schema that we concentrate on in the work presented here. This configuration requires low input power for the locking and short (picosecond) pulses are produced that can be used directly in all-optical processing. The locking range is typically in the order of a few tens of MHz. The quality of the recovered clock depends on the MLL used itself. Latest results from Shin Arahira et al. at 160 Gb/s [26] regenerate a 160 GHz clock source with a timing jitter better than the input data signal, which is < 0.1 ps.

Comparing the PLL and AOCR techniques, it can be noted that currently very good clock recovery performance can be achieved either with an EAM in a PLL scheme or in an AOCR scheme using a single MLL. The second option is clearly easier as it requires only the MLL and two isolators. Furthermore it is an all optical solution. On the other hand, PLL schemes are more suitable for OCR and clock frequency division at the same time. This has been reported upon for PLL schemes with an EAM [10] and with a MLL [27].

In this chapter, we present initial test experiments on a 20 GHz Fabry-Pérot MLL for AOCR and clock frequency division. The performance of the laser used made that the very good results mentioned above could not be achieved, however many characteristics for AOCR could be quantified. The quality of the recovered clock as a function of the input power signal is shown analyzing RF spectra, Single Side Band (SSB) curves and oscilloscope traces. The locking range of the FPMLL to the input signal has been found to be as well in the order of few tens of MHz. The robustness of the locking of the laser to the input data signal has been tested varying the number of zeros in a row in the input signal. 2^{31}-1 Pseudo Random Binary Sequence (PRBS) data signal can be retrieved easily.

In the last section, the design of a 40 GHz MLL laser is presented in a ring configuration for an active-passive wafer. The design takes into account all the minimizations of small intra-cavity reflections. For AOCR application a novel way to couple the optical input signal into the MLL via a separate waveguide has been designed. The timing jitter of the clock recovered from this laser should be sufficiently low to comply with the telecom requirements at 40 GHz [2,3]. Firstly, as seen in Section 5.4, the timing jitter of an unseeded passively modelocked RMLL is improved thanks to the CPM mechanism. Secondly, having an integrated extended cavity limits the self pulsation dynamics (see Section 5.5), the active-passive RMLL with its extended cavity should then be more stable than the all-active device presented in Section 5.4. Passively modelocked, the timing jitter of the 40GHz MLL is expected to be close to the 3.6 ps reported by Ji et al. in a Fabry-Pérot integrated EC-MLL in a CPM configuration [28]. Finally, as shown in the following section, the timing jitter value of a recovered clock is much smaller than the timing jitter of the passively modelocked laser. A recovered clock at 40 GHz with a timing jitter value below 0.4 ps is expected to be feasible using a RMLL with the design presented in this last section.

6.2 Optical clock recovery using a 20 GHz Fabry-Pérot modelocked laser

6.2.1 Introduction

All Optical Clock Recovery (AOCR) experiments using 20 and 40 Gb/s signals have been performed by injecting these signals directly into a 20 GHz Fabry-Pérot ModeLocked Laser (FPMLL). The FPMLL used in this experiment is of the same design as the laser described in Chapter 5.2, but operating around 1558nm. The physical length of the cavity is 2000 μm and the length of the Saturable Absorber is 12μm (SA). The performance of this passively modelocked laser is not as good as the laser reported upon in Chapter 5.2. The laser is modelocked over a continuous range of amplifier current values between 110 and 125 mA and a range of reverse voltages on the SA between - 1.8 and - 2.6 V. However pulses produced are highly chirped and approximately 8 ps in width. The lasing wavelength of the FPMLL is 1558 nm and the injected data signal wavelength is 1550 nm. The injected signal at this lower wavelength can modulate the SA and can be filtered out from the output signals of the FPMLL. After a short description of the experimental setup, results of our first demonstration of AOCR close to the fundamental frequency of the FPMLL are discussed. Presented are the studies of the RF spectra (Section 6.2.3), the phase noise traces (Section 6.2.4) and sampling oscilloscope traces (Section 6.2.5), all versus the input power. It will be shown that the FPMLL is locked even a low input power. An important parameter for OCR is the locking range of FPMLL on the input signal; this has been studied for two input power levels in Section 6.2.6. Different RZ modulation patterns have been applied to the input signal for locking; the FPMLL appeared locked for all standard PRBS pattern lengths. In Section 6.2.7, the robustness of the locking has been investigating further by increasing the series of zeros in the input signal. AOCR and clock frequency division of a 40 Gb/s signal to 20GHz have been investigated and demonstrated in Section 6.2.8. It is shown that the FPMLL is modelocked at its fundamental frequency but with a train of 2 pulses of different intensities. In that configuration the locking range is much smaller.

6.2.2 Experimental setup

The testing of AOCR requires the following experimental setup. Firstly, an optical data signal needs to be generated at different frequencies around 20 Gb/s and 40 Gb/s. The optical data signal is then injected into the FPMLL and the clock is recovered at the wavelength of the free running FPMLL. The recovered signal is then analyzed by a number of instruments. The details of the experimental setup are plotted in Figure 6.2.1. The optical data signal was generated from an active modelocked laser source (Pritel) driven by an external RF source. Pulses of 2 ps at a repetition rate around 10 GHz were generated. A data signal was then created using a pattern generator and a modulator. This data signal was then multiplexed to 20 Gb/s or 40 Gb/s (Pritel optical clock multiplier). The signal was then amplified and filtered (3 nm bandwidth filter). The signal is then sent through 100 m of SMF to another lab

where the input power to the FPMLL was controlled using an optical attenuator. The FPMLL chip is mounted as described in Section 5.2. The light was injected at the SA side of the FPMLL and coupled out at the other side using lensed fibers. A photograph of the chip under test is presented in Figure 6.2.2. Optical isolators are used before and after the chip. The optical spectra have been recorded with a high resolution OSA (APEX AP2041A) with a resolution of 0.8 pm. The signal was re-amplified in an EDFA and filtered using a 2 nm bandwidth filter in order to have sufficient intensity to measure RF spectra and oscilloscope traces. The filter also removes most of the data signal sent into the FPMLL. RF spectra were recorded using a 12 ps IR photodetector (New Focus model 1024) and a 50 GHz Agilent PSA E4448A spectrum analyzer. The Single Side Band (SSB) phase noise spectra have been measured directly on the spectrum analyzer using the phase noise measurements utility. The extracted clock signal can be sent back to the first lab via the two circulators at each side of the 100 m SMF, and is recorded on an Agilent Terascope (bandwidth of 750 GHz). A Tektronix scope with a bandwidth of 30 GHz has also been used to test the robustness of the locking against long series of zeros in the input signal at 20 Gb/s (Section 6.2.7).

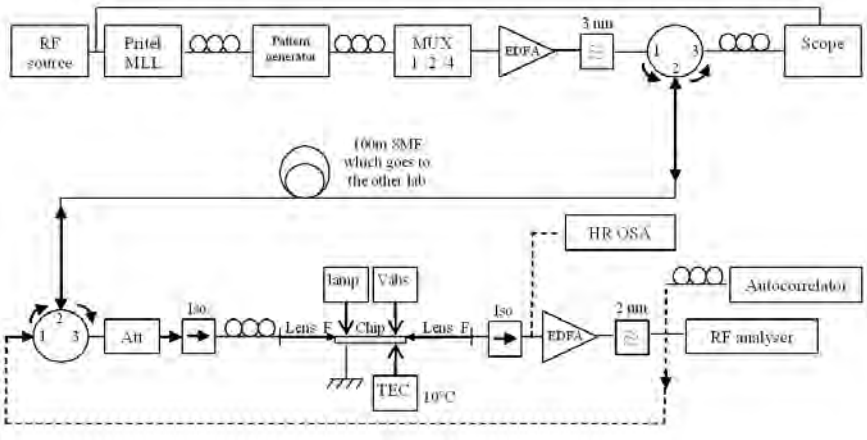

Figure 6.2.1 AOCR setup used. The setup is split in two labs and connected by a 100 m long single mode fiber. The clock signal extracted can be sent back via two circulators and recorded on the scope.

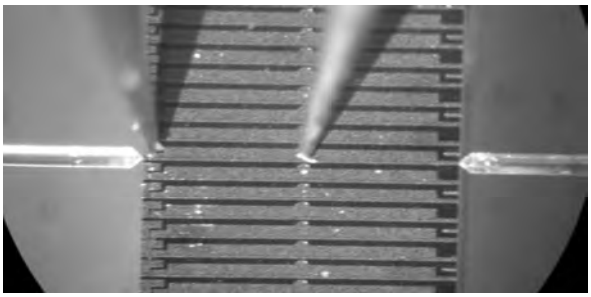

Figure 6.2.2 Picture of the chip under test. The SA is on the left where the data signal is injected by a lensed fiber. The output of the laser is collected by a second lensed fiber.

6.2.3 20 Gb/s optical clock recovery

AOCR has been demonstrated at a repetition rate of 19.721 Gb/s which was 3 MHz above the free running repetition rate of the FPMLL. The wavelength of the injected signal was 8 nm below the lasing peak wavelength of the FPMLL. An optical spectrum of the output of the FPMLL under injection is plotted in Figure 6.2.3, the components from the input data signal are visible at 1550 nm. The input signal is filtered out at the output of the FPMLL using a 2 nm bandpass filter. The locking is analyzed on the RF spectrum analyzer. In Figure 6.2.4, at an input power into the chip of - 26 dBm, one can see than the FPMLL is not locked. The wide peak in the RF spectrum corresponds to the FPML free running regime. But at two times higher input power (- 23 dBm) the FPMLL is locked. The thin peak in the RF spectrum has increased by 10 dB and the wide peak is now centered on the input signal data frequency. The average output power of the laser is ~2 dBm at one facet. Comparing this number to the injected power into the laser, an input signal power that is 25 dB lower, is already sufficient to lock the FPMLL. At low input power the RF spectrum is wide, which means the timing jitter is dominated by the passively modelocked laser itself. Increasing the input power up to - 11 dBm, the RF spectrum improves. This is confirmed by timing jitter measurements (Section 6.2.4). Sending higher power levels into the FPMLL disturbs the modelocking of the laser. This is most likely to be due to the fact that amplification of the input signal in the amplifier of the laser starts to affect the amplification of the laser modes.

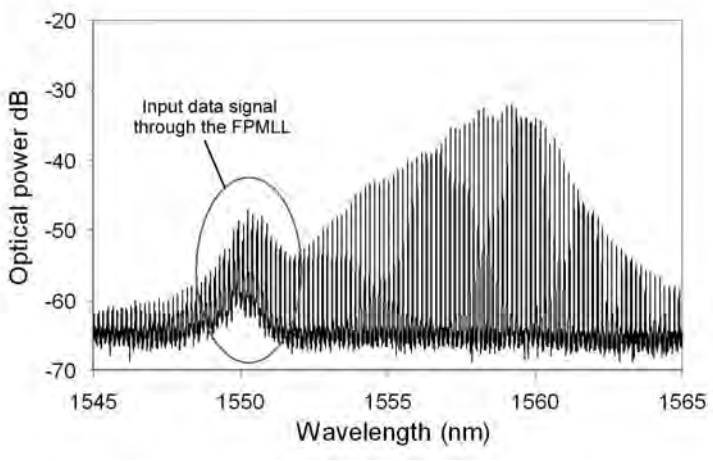

Figure 6.2.3 Optical spectrum of the FPMLL output with optical signal injection at - 11 dBm input power. This signal is then filtered with a 2 nm bandpass filter centered at 1558 nm. (I_{amp} = 120 mA, V_{SA} = - 2.2 V)

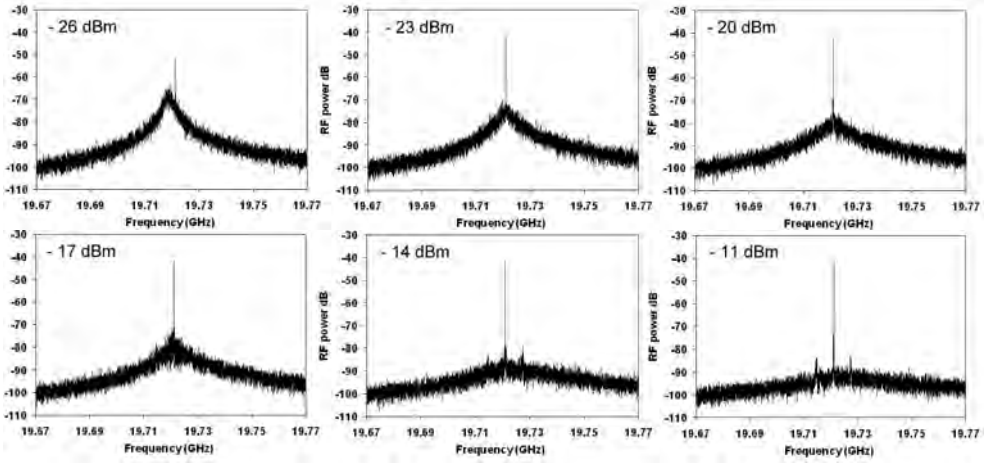

Figure 6.2.4 RF spectra of the FPMLL output with optical signal injection at different input power. The FPMLL is locked to the input signal at input power levels over - 23 dBm. (I_{amp} = 120 mA, V_{SA} = - 2.2 V, P_{FPMLL} = 2 dBm)

6.2.4 Timing jitter measurements of the 20 GHz recovered clock

Timing jitter values have been determined from the Single Side Band (SSB) phase noise curves measured using the phase noise measurements utility of a 50 GHz Agilent PSA E4448A spectrum analyzer. Phase noise traces are plotted for two different optical input power levels into the FPMLL in Figure 6.2.5. A clear reduction

of the SSB level is observed by increasing the power of the input data from -22 dBm to -11 dBm [29]. The Displayed Average Noise level (DANL) is also plotted. The DANL corresponds to RMS averaging of a frequency noise spectrum where no input is connected to the equipment. Phase noise curves are corrected with the DANL. The timing jitter can then be calculated by integrating the curve on the frequency ranges of interest (10 kHz – 80 MHz and 80 MHz – 10 GHz). The timing jitter of the FPMLL without injected data could not be measured since it was too large; the SSB curve measurement requires a source with a timing jitter value below ~14 ps. Results of the measured timing jitter for different data input power levels [29] are summarized in Table 6.2.1. The timing jitter has been reduced by at least a factor 5 but the value is still high knowing that the timing jitter from the input signal was 200 fs (10 kHz – 80 MHz range of integration). The requirements on timing jitter values becomes more stringent with increasing bit rates, i.e. a 160 Gb/s signal requires timing jitter values of the clock below 0.44 ps [2,3]. As a conclusion, a passively modelocked laser with better noise properties is required. For 160 Gb/s we expect that the free running timing jitter value of a passively ML needs to be below 4 ps in order to obtain a recovered clock signal with a sufficiently low timing jitter value for use in OTDM systems. Integrated modelocked lasers have a very low jitter at the highest frequency range, when active harmonic modelocked external-cavity laser can suffer from supermode noise [30].

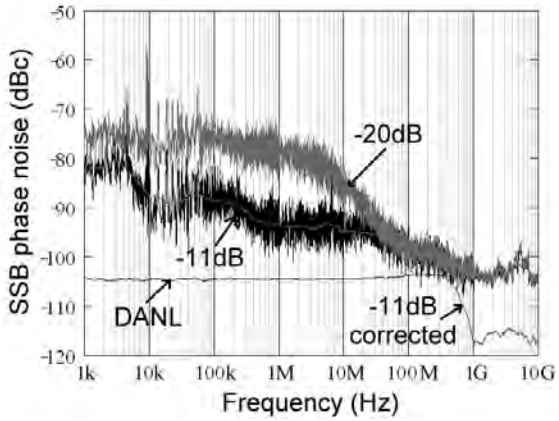

Figure 6.2.5 SSB phase noise curves of the FPMLL output for - 11 dB and - 20 dB injected signal levels. For - 11 dB input power, the SSB phase noise is also corrected using the Displayed Average Noise level (DANL). (I_{amp} = 120 mA, V_{SA} = - 2.2 V, P_{FPMLL} = 2 dBm)

Table 6.2.1: Measured timing jitter values for different data input power levels

Input power	Timing jitter (10 kHz – 80 MHz)	Timing jitter (80 MHz – 10 GHz)
- 11 dBm	2.13 ps	3.40 ps
- 17 dBm	3.88 ps	3.41 ps
- 20 dBm	5.15 ps	4.03 ps
- 24 dBm	8.28 ps	6.48 ps

6.2.5 Sampling oscilloscope traces of 20 GHz recovered clock

As mentioned in the description of the setup, the recovered clock signal can be sent back to the first lab and be recorded on the terahertz oscilloscope (see Figure 6.2.1). In Figure 6.2.6 oscilloscope traces are presented for a number of data signal input power levels to the FPMLL. The sampling oscilloscope was synchronized to the 10 GHz RF clock of the data source. If the clock was not recovered, no pulses were visible on the oscilloscope. The clarity of the pulses on the oscilloscope corresponds to the timing jitter measured in the section above. Similar traces are shown by Lasri et al. in [12]. The timing jitter measured was still significant: 2.1 ps (10 kHz – 80 MHz range) in the best case. At - 11 dBm, the pulses are clearly visible but not really open due to the 2.1 ps timing jitter. Decreasing the input power injection down to – 20 dBm, the quality of the pulses does not clearly change, although the measured timing jitter value increases. However, at – 23 dBm it is clearly visible the input power is close to the locking limit: the pulses are difficult to distinguish. At – 26 dBm, the trace confirms what is observed from the RF spectrum (Figure 6.2.4) that the FPMLL is not locked to the input signal. The oscilloscope trace at – 14 dBm input power averaged 16 times is plotted in Figure 6.2.7, the pulses are clearly visible.

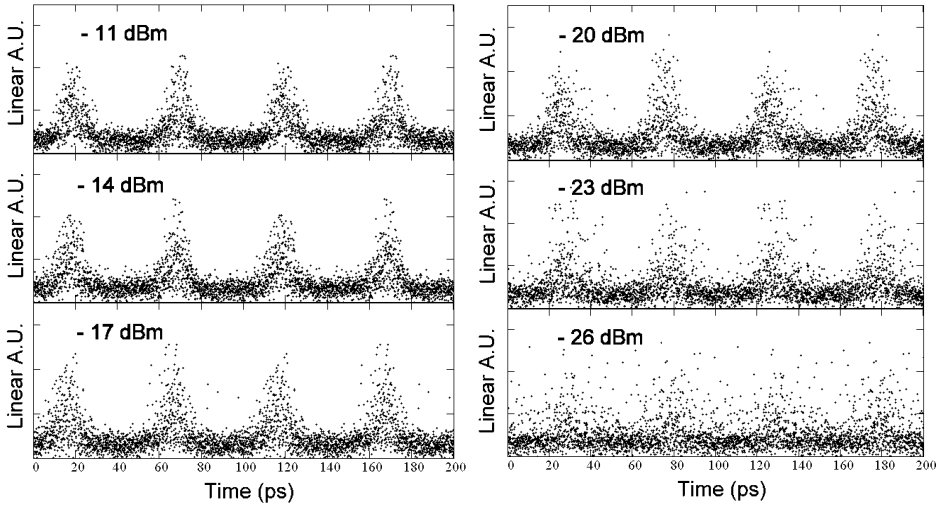

Figure 6.2.6 Sampling oscilloscope traces of the FPMLL output for different data signal input powers. No averaging is used. (I_{amp} = 118 mA, V_{SA} = - 2.2 V, PRBS '31, 19.721 GHz)

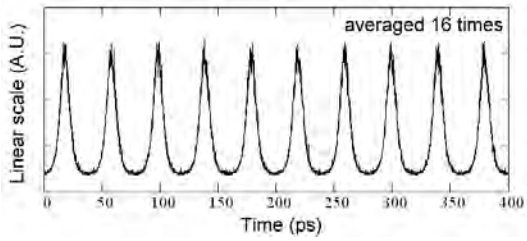

Figure 6.2.7 Sampling oscilloscope trace averaged 16 times of the FPMLL output for a signal input power of -20dBm. (I_{amp} = 118 mA, V_{SA} = - 2.2 V, PRBS '31, 19.721 GHz)

6.2.6 Frequency locking range of the FPMLL

An important parameter for AOCR is the locking range. It is the range in which the input signal clock frequency can vary and can still be recovered. RF spectra of the laser output have been measured for different data clock frequencies and for two input power levels (- 17 dBm and - 11 dBm). Results are plotted in Figure 6.2.8. The locking range depends on the input power injected [31], the measured ranges are ~25 MHz at - 17 dBm input power and ~35 MHz at - 11 dBm. The locking range measured is comfortable for optical clock recovery application [11]. However to fabricate a device within this accuracy to a particular frequency presents a challenge.

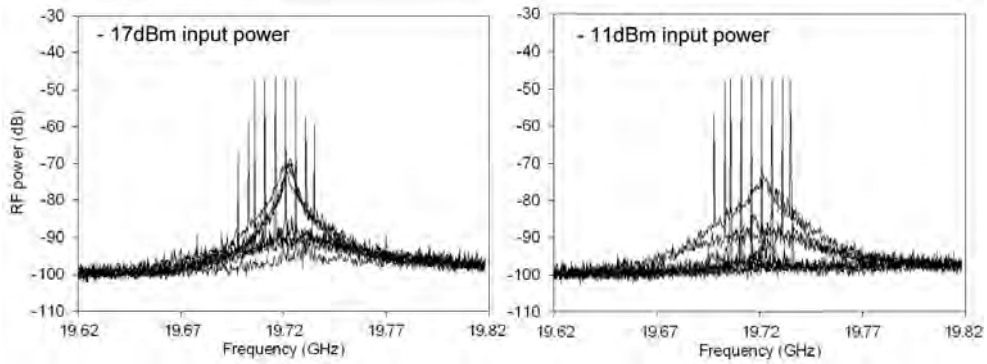

Figure 6.2.8 RF spectra of the FPMLL output with optical signal injection at different repetition rates. The locking range is respectively 25 MHz and 35MHz for - 17 dBm and – 11 dBm. (I_{amp} = 120 mA, V_{SA} = - 2.2 V, P_{FPMLL} = 2 dBm, PRBS'31)

6.2.7 Robustness of the locking at 20 Gb/s

We have investigated the robustness of the locking of the FPMLL to the input data using patterns with a varying number of zeros. It has to be taken into consideration that the 20 Gb/s signal is composed by multiplexing the patterned 10 Gb/s signal. The multiplexer used has a delay of 6.4 ps which corresponds to 64 bits. Thus 128 bits patterns are created from two copies of an arbitrary 64 bit pattern by interleaving. The Pseudo Random Binary Sequence (PRBS) has up to 31 "1" bits in a row. The sequences tested were: 32 "0" - 32 "1", 64 "0" - 64 "1", 96 "0" - 32 "1" and 112 "0" - 16 "1". The power level was kept at -11 dBm. We have analyzed the results recording RF spectra and time series (30 GHz Tektronix scope). The RF spectra for the longest and the shortest series of "0"s are plotted in Figure 6.2.9. The rate of the signal was at 19.737 GHz which is 10 MHz off the free running FPMLL frequency. In both cases the FPMLL is locked to the optical data steam, but the change in background level shows different qualities of locking. These results can be compared to the RF spectra in Figure 6.2.4 at -17 dBm and -11 dBm. This observation is confirmed by the recorded time series. The time series for a 32 "1" – 32 "0" signal is plotted in Figure 6.2.10. The "1" bits can be located in the oscilloscope trace, as indicated in the figure. A variation of less than 15% in the peak output power can be observed due to the transition in the input "1" and "0" series. When the number of zeros in a row is increased to 64, 96 and 112, the contrast in the oscilloscope degrades. The trace for 64 zeros in a row is acceptable, but the traces for 96 and 112 zeros in a row reveal a background level, meaning the signal is not exactly synchronized to the input data [7]. The FPMLL that we used stays synchronised to 64 zeros in a row, which is twice the PRBS requirement.

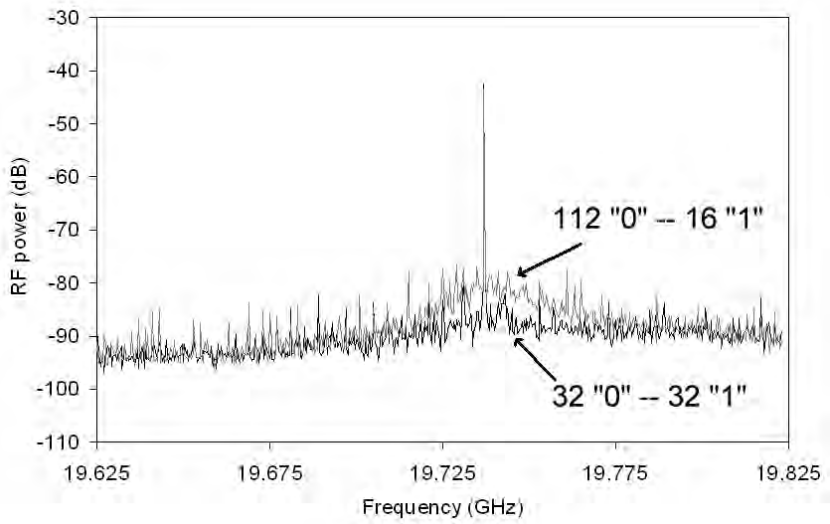

Figure 6.2.9 RF spectra of the FPMLL output with two different patterns in the injected signal. (I_{amp} = 128 mA, V_{SA} = - 2.4 V, $P_{injected}$ = - 11 dBm at 19.737 GHz)

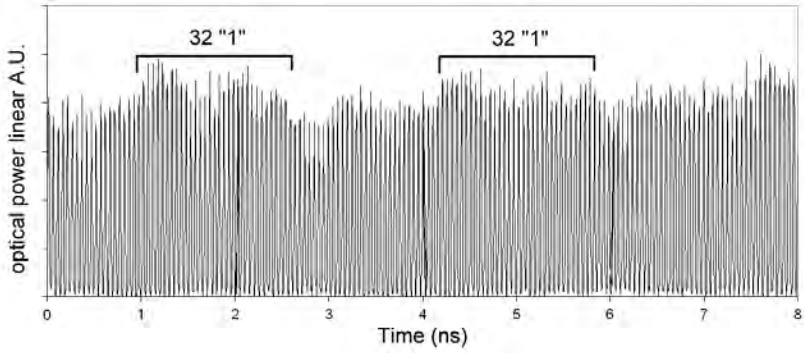

Figure 6.2.10 Trace of the FPMLL output with optical signal injection (32 "1" – 32 "0") recording on a 30 GHz sampling oscilloscope. (I_{amp} = 128 mA, V_{SA} = - 2.4 V, $P_{injected}$ = - 11 dBm at 19.737 GHz)

6.2.8 40 Gb/s clock recovery

We have investigated the possibility to use the same FPMLL as a clock extractor and divider of a 40 Gb/s signal to a 20 GHz frequency. First experiments at exactly twice the free running repetition rate of the FPMLL (39.442 Gb/s) were poor. Better results have been obtained at 39.474 Gb/s. The roundtrip time of the FPMLL cavity is changed by the optical injection. For certain, differences were observed between injecting one or two pulses per cavity roundtrip time for the same power level. The wavelength of the input signal is still 8 nm below the lasing peak of the

FPMLL. Locking is achieved but only with a small locking range. In fact, for each input power and reverse voltage on the SA, the current of the amplifier needed to be finely tuned. Two RF spectra are plotted in Figure 6.2.1 for two input power levels. At - 11 dBm input power signal, the RF peak at the fundamental frequency is 140 kHz wide at - 10 dB below the peak. The width increases up to 380 kHz at - 10 dB with a -14 dBm input power. In both cases, this is much larger than the RF peak widths measured at 20 Gb/s injection. Besides this aspect, more power is needed to lock the FPMLL to the clock than at 20 GHz. The FPMLL is not locked below -17 dBm input power injection. Important information is obtained from the sampling oscilloscope. Averaging the trace 16 times (Figure 6.2.12), reveals a train of two pulses with different intensities; the clock at 19.737 GHz is not perfect. To improve the results, a solution would be to feedback part of the output of the laser FPMLL and to add it to the input data signal. This however requires an adjustable delay line [25,27]. Another solution would be to cascade a second FPMLL laser [23], but in this configuration the timing jitter of the clock at the output of the second FPMLL will not be sufficiently low for optical signal processing applications.

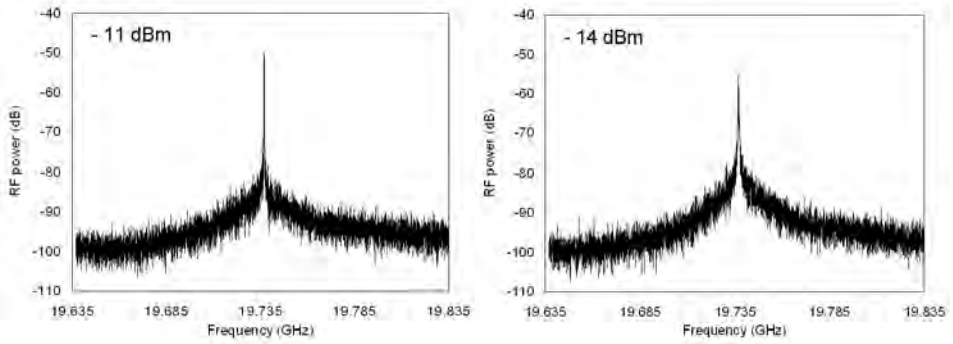

Figure 6.2.11 RF spectra of the FPMLL output with 39.474Gb/s optical signal injection at two different input power levels. The FPMLL is locked to the input signal at its fundamental frequency.
(I_{amp} = 119.9 mA, V_{SA} = - 2.4 V and I_{amp} = 128 mA, V_{SA} = - 2.6 V)

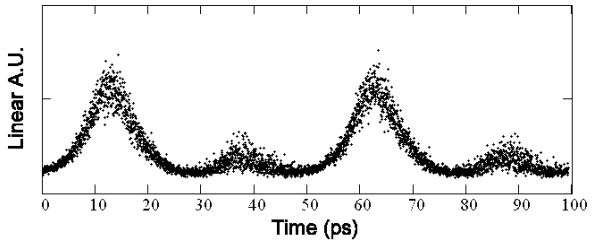

Figure 6.2.12 Sampling oscilloscope trace of the FPMLL output 39.474Gb/s optical signal injection at -11 dBm input power. Averaging the signal 16 times, a train of two pulses with different intensity is visible. (I_{amp} = 118.8 mA, V_{SA} = - 2.2 V, PRBS'31)

6.3 Designs for an integrated AOCR device

6.3.1 Introduction

We present in this section the design of an integrated 40 GHz Ring Modelocked Laser (RMLL) which exploits the possibility of monolithically combing active and passive components to obtain a much improved device for AOCR. It has a specific input waveguide for AOCR which is explained in details in the following section with the frequency division issue.

6.3.2 Design of the RMLL

We present in this section the design of an integrated 40 GHz Ring Modelocked Laser (RMLL) which has an integrated extended cavity to be realized in active-passive integration. The layout is plotted in Figure 6.3.1. The device is symmetric; two counter propagating pulses will experience the same optical path, but in opposite direction. According to the simulations of Section 2.3 the modelocking range is larger in such a configuration. The total length of the ring laser is approximately 2 mm. The length of the active block region (visible below the amplifier contact) is 500 μm. A SA is positioned in the center of the active region. In the designs on the mask the SA length varies from 10 to 30 μm which covers the optimum length. The SA is isolated by two 15 μm long isolation waveguide sections (see Section 3.2). It has been previously shown, in Section 5.5, that the modelocking mechanism of a MLL is strongly disturbed by internal reflections. In this design all the possible internal reflections have been minimized. First, the small butt-joint reflections, characterized in Section 3.3 and in [32], are minimized. The reflection value should be lower than 10^{-5} by crossing the interface with a waveguide under a 14° angle.

To achieve the 2 mm cavity length, deeply etched waveguides are used for small (60 μm) bending radii; shallowly etched waveguides with low propagation loss and amplifiers. The transition between deep and shallow waveguides used for this design is different from the transition used in the 27 GHz RMLL (Section 5.5) as described in [33,34]. In the initial fabrication scheme, the masking of the deep areas was realized with a photoresist layer. Since this resist layer is partly etched during the processing, the design required to be tolerant to this aspect. The use of a Ti mask with thin photoresist for lift-off is better. The masking does not change with the etching process, thus small features can be realized with a proper alignment. The deep-shallow transition used is an adiabatic design as shown in Figure 6.3.2, a similar design has been used in [35]. The transition is done smoothly using a double taper, a taper for the top of the waveguides and a second taper the core of the film. This second taper is realized with the Ti mask. No reflection has been observed from the initial deep-shallow transition design. But, in case the layerstack is different than requested or if the etching of the shallow waveguide is not as designed, the initial design can give rise to small undesirable reflections. The design shown in Figure 6.3.2 automatically matches the two types of waveguides, thus no reflections are created in any case.

The two 180° bends in the cavity are high contrast waveguides (deeply etched). For each curve, adiabatic bends are used [36], in order to avoid offsets [37]. The light from the ring is coupled out using a multimode interferometer (MMI). MMI can create internal reflections as well [38] in case the layerstack or the fabrication deviates from the simulated design. The RMLL presented here uses an optimized MMI as described in [39]. Back reflection at the input waveguides of the MMI can be reduced by at least 10 dB. Looking at Figure 6.3.3, one can see that the spaces next to the input/output waveguides have very low field strengths. Those areas can be removed by having sections of the walls of the MMI at a 45º angle, without affecting the operation of the MMI. Furthermore, when the fabricated device deviates from its design, the back reflections inside the MMI are not coupled back into the input waveguides. From the 2 outputs of the MMI the light is guided to the edge of the chip using tilted waveguides which are 7° with respect to the facet's normal. The output waveguides contain mode filters [40] in order to reduce facet reflectivity (not visible in the Figure 6.2.1). In addition, the facets of the chip need to be AR coated.

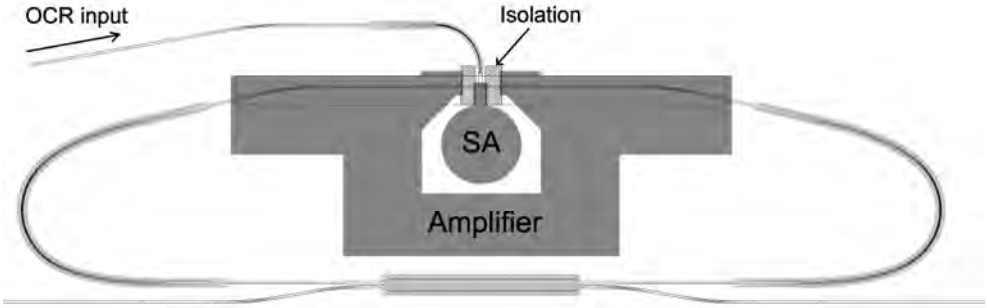

Figure 6.3.1 Mask layout of a 40GHz All Optical Clock Recovery Ring ModeLocked Laser (AOCR-RMLL). The light grey background indicates the deeply etched areas.

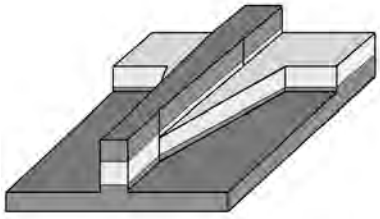

Figure 6.3.2 Schematic depiction of the deep-shallow transition used. The shallow waveguide is 2.0 μm wide and the deeply etched waveguide is 1.7 μm wide. The transition is done smoothly using two tapers, a taper for the waveguide and one for the film.

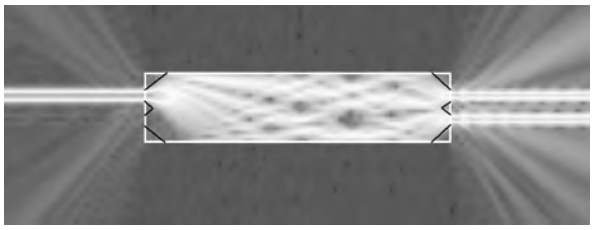

Figure 6.3.3 Top view of the simulated light field in a MMI. The back reflections are suppressed in the MMI coupler by having sections of the walls of the MMI on which reflections may occur, at a 45º angle.

6.3.3 Concept and design of a separate AOCR input

As shown in Section 6.2, All Optical Clock Recovery (AOCR) can be realized by injecting part of a data signal into a modelocked laser. In a Fabry-Pérot MLL light can be directed to the facet where the SA is. The absorption of the SA is modulated by the input signal and the FPMLL locks to it. The fraction of the input signal that is not absorbed also passes through the laser cavity and need to be filtered out later. We have observed that at high input power of the signal into the cavity, the amplifier becomes saturated by the input signal and the modelocking mechanism is affected detrimentally. In the case of a ring MLL, if light is injected at one input, it will disrupt the symmetry in the laser, which will therefore not fully operate optimally. It was seen in the laser simulations that a symmetric regime was preferable for the largest stability region. In any case, ring lasers are preferred for their easy connectivity with other components on a chip and the CPM configuration.

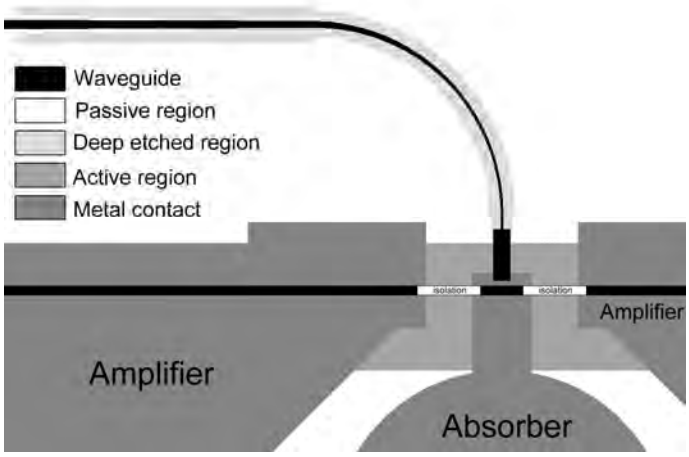

Figure 6.3.4 Mask layout in the region of the OCR input. The OCR input is a short wide waveguide ridge spreading the input light over a section of the SA.

The new concept presented in this section can be first named All-Optical Active Modelocking (AOA-ML). The idea is to modulate only the SA with an optical input clock signal in a way that is similar to electronic modulation of the SA in standard active or hybrid modelocking [41]. If the input clock signal is replaced by a data signal, the same device recovers the clock signal of the data: we have an All Optical Clock Recovery Ring ModeLocked Laser (AOCR-RMLL). There is a similarity with an optically driven EAM as presented by Demir et al. [42], but without optical-electrical-optical conversion. The optically pumped SA solution can be realized in active passive integration. A passive input waveguide guides the data signal to the side of the SA to modulate its absorption. A proposed design as an addition to a 40 GHz RMLL is presented in Figure 6.3.1. An enlarged view of the OCR input is given in Figure 6.2.1. The input waveguide leads to a deeply etched curved waveguide. This waveguide is tapered down to 0.8 μm which is connected at the end to a shallowly etched 6 μm wide waveguide that is 10 μm long. The narrow launch in the wide waveguide makes the light spread along a large part of the SA. The wide shallow waveguide stops 1.5 μm from the SA in order to avoid an abrupt change in index in the cavity waveguide which would lead to internal reflections in the ring cavity. The area is shallowly etched, so the input light reaches the SA though the film (see Section 3.2). The short wide waveguide is partly in an unpumped active region. The input light will have to pass through this waveguide and sufficient power has end up at the SA in order to modulate it sufficiently. This will take some extra input power which can be compensated if necessary using an input amplifier. Moreover the device is rather independent to the input wavelength, especially at wavelengths lower than the lasing wavelength where the absorption is higher [43]. The device should operate better for TE polarization, nevertheless the absorption of the bulk material for TM polarization is reasonable as well, therefore above a certain power level the AOCR device is polarization independent [44].

The last issue is the AOCR and clock division. We have seen in Section 6.2.8, that the combination of AOCR and frequency division was not working well. Tsuchida recently proposed a scheme [27] for a hybridly modelocked laser diode. In his scheme part of the MLL output is directed via a tunable delay line to a photodiode, where it is mixed with the optical input data signal. The signal from the photodiode is amplified in order to drive the modulation of the SA in the MLL. This pushes the laser to operate only at its fundamental frequency. An all-optical realization of this concept can in principle be fully integrated on chip using our technology. This is presented schematically in Figure 6.3.5. The difficulty in this design would be the synchronization of the input data signal with part of the re-injected AOCR-RMLL signal. Considering a 40 GHz RMLL, a 20 MHz tuning range would start to be acceptable. 20 MHz at 40 GHz can be set using a 8 mm long phase shifter in our technology [45]. This phase shifter is part of the feedback arm which has to match in optical pass length a multiple of the repetition rate of the RMLL under injection.

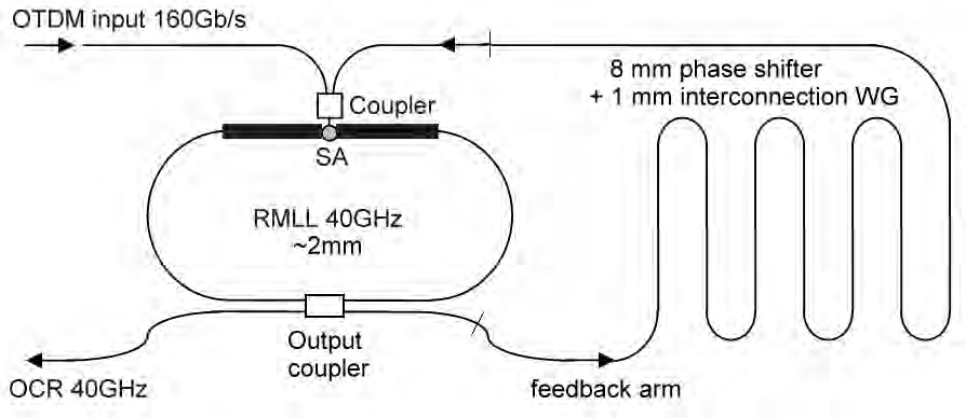

Figure 6.3.5 Scheme of a 40 GHz all optical clock recovery ring modelocked laser (AOCR-RMLL) with a feedback arm for optical clock division.

6.4 List of references

1 E. J. M. Verdurmen, A. M. J. Koonen, and H. de Waardt "Time domain add-drop multiplexing for RZ-DPSK OTDM signals" Optics Express, Vol. 14, Issue 12, pp. 5114-5120, (2006)

2 E. J. M. Verdurmen, "Optical Time domain add-drop multiplexing employing fiber nonlinearities" PhD Thesis, Eindhoven University of technology, ISBN-13: 978-90-386-1923-1, (2006)

3 Kresten Yvind, "Semiconductor modelocked lasers for optical communication systems" PhD thesis, ISBN: 87-90974-46-8, (2003)

4 J. Klapper and J.T. Frankle, "Phase-Locked and Frequency-Feedback Systems", Academic Press, (1972)

5 O. Kamatani, S.; Kawanishi, "Prescaled timing extraction from 400 Gb/s optical signal using a phase lock loop based on four-wave-mixing in a laser diode amplifier" IEEE Photonics Technology Letters, Vol. 8, Issue 8, pp. 1094-1096, (1996)

6 T. Yamamoto, L.K. Oxenlowe, C. Schmidt, C. Schubert, E. Hilliger, U. Feiste, J. Berger, R. Ludwig, H.G. Weber, "Clock recovery from 160 Gbit/s data signals using phase-locked loop with interferometric optical switch based on semiconductor optical amplifier" Electronics Letters, Vol. 37, Issue 8, pp. 509-510, (2001)

7 H. Tsuchida, M. Suzuki, "40-Gb/s optical clock recovery using an injection-locked optoelectronic oscillator" IEEE Photonics Technology Letters, Vol. 17, Issue 1, pp. 211-213, (2005)

8 I.D. Phillips, A.D. Ellis, T. Widdowson, D. Nesset, A.E. Kelly and D. Trommer "100 Gbit/s optical clock recovery using electrical phaselocked loop consisting of commercially available components" Electronics Letters Vol. 36, Issue 7, pp. 650-652, (2000)

9 D.T.K. Tong, K.L. Deng, B. Mikkelsen, G. Raybon, K.F. Dreyer, J.E. Johnson, "160 Gbit/s clock recovery using electroabsorption modulator-based phase-locked loop" Electronics Letters, Vol. 36, Issue 23, pp. 1951-1952, (2000)

10 E.S. Awad, P.S. Cho, N. Moulton and J. Goldhar "Subharmonic Optical Clock Recovery From 160 Gb/s using Time-Dependent Loss Saturation Inside a Single Electroabsorption Modulator" IEEE Photonics Technology Letters, Vol. 15, Issue 12, pp. 1764-1766, (2003)

11 J. P. Turkiewicz, E. Tangdiongga, G. D. Khoe and H. de Waardt "Clock Recovery and Demultiplexing Performance of 160-Gb/s OTDM Field Experiments" IEEE Photonics Technology Letters, Vol. 16, Issue 6, pp. 1555-1557, (2004).

12 J. Lasri, P. Devgan, R. Tang, and P. Kumar, "Ultralow Timing Jitter 40-Gb/s Clock Recovery Using a Self-Starting Optoelectronic Oscillator" IEEE Photonics Technology Letters, Vol. 16, No. 1, pp. 263-265, (2004)

13 Yingmin Yang, Yang Jing Wen, A Nirmalathas, Hai Feng Liu,D. Novak, "Optical clock recovery at line rates via injection locking of a long cavity Fabry-Pérot laser diode" IEEE Photonics Technology Letters, Vol. 16, Issue 6, pp. 1561- 1563 (2004)

14 G. Contestabile, A. D'Errico, M. Presi, and E. Ciaramella "40-GHz All-Optical Clock Extraction Using a Semiconductor-Assisted Fabry–Pérot Filter" IEEE Photonics Technology Letters, Vol. 16, Issue 11, pp2523-2525, (2004)

15 E. Kehayas, L. Stampoulidis, H. Avramopoulos, Y. Liu, E. Tangdiongga and H.J.S. Dorren "40 Gb/s all-optical packet clock recovery with ultrafast lock-in time and low inter-packet guardbands" Optics Express, Vol. 13, Issue 2 pp. 475-480 (2005)

16 M. Attygalle and Yang Jing Wen, "Injection-Locked Fabry–Pérot Laser With Electronic Feedback for Clock Recovery From High-Speed OTDM Signals" IEEE Photonics Technology Letters, Vol. 18, Issue 3, pp. 478-480, (2006)

17 C. Bornholdt, B. Sartorius, S. Schelbase, M. Mohrle, S. Bauer, "Self-pulsating DFB laser for all-optical clock recovery at 40Gbit/s" Electronics Letters, Vol. 36, Issue 4, pp. 327-328, (2000)

18 C. Bornholdt, S. Bauer, M. Mohrle, H-P. Nolting, B. Sartorius, "All optical clock recovery at 80 GHz and beyond" 27th European Conference on Optical Communication, ECOC '01, Vol. 4, pp. 502- 503, (2001)

19 B. Sartorius, C. Bornholdt, S. Bauer, M. Mohrle, "40 GHz optical clock recovery for application in asynchronous networks" 27th European Conference on Optical Communication, ECOC '01, Vol. 3, pp. 442-443, (2001)

20 Yuhua Li, Cheolhwan Kim, Guifang Li, Y. Kaneko, R.L. Jungerman, O. Buccafusca, "Wavelength and polarization insensitive all-optical clock recovery from 96-Gb/s data by using a two-section gain-coupled DFB laser" IEEE Photonics Technology Letters, Vol. 15, Issue 4, pp. 590- 592 (2003)

21 Inwoong Kim, Cheolhwan Kim, Guifang Li, Patrick LiKamWa, and Jin Hong, "180-GHz Clock Recovery Using a Multisection Gain-Coupled Distributed Feedback Laser" IEEE Photonics Technology Letters, Vol. 17, Issue 6, pp. 1295-1297, (2005)

22 H. Kurita, I. Ogura, H. Yokoyama, "Ultrafast All-Optical Signal Processing with Mode-Locked Semiconductor Lasers" IEICE Transactions on Electronics Vol.E81-C Issue 2 pp. 129-139, (1998)

23 H. Yokoyama, Y. Hashimoto, H. Kurita, I. Ogura, "Two-stage all-optical subharmonic clock recovery using modelocked semiconductor lasers" Electronics Letters Vol. 36, Issue 18, pp. 1577-1578, (2000)

24 R Schreieck, M Kwakernaak, H Jäckel, "All-Optical Clock Extraction at 160 Gbit/s wth Monolithic Mode-Locked Laser Diodes" IEICE Transactions on Electronics Vol.E84-C, Issue 6, pp.841-844, (2001)

25 T Ohno, K Sato, T Shimizu, T Furuta, H Ito "Recovery of 40 GHz optical clock from 160 Gbit/s data using regeneratively modelocked semiconductor laser" Electronics Letters Vol. 39, Issue 5, pp. 453-455, (2003)

26 S. Arahira, S. Sasaki, K. Tachibana, Y. Ogawa, "All-optical 160-gb/s clock extraction with a mode-locked laser diode module" IEEE Photonics Technology Letters, Vol. 16, Issue 6, pp. 1558- 1560 (2004)

27 H. Tsuchida, "160-gb/s optical clock recovery using a regeneratively mode-locked laser diode" IEEE Photonics Technology Letters, Vol. 18, Issue 16, pp. 1687- 1689, (2006)

28 C. Ji, N. Chubun, R.G. Broeke, J. Cao, Y. Du, S.J.B Yoo, K.Y. Liou, J.R. Lothian, S. Vatanapradit, S.N.G. Chu, B. Patel, W.S. Hobson, W.T. Tsang, "Synchronized Transform-Limited Operation of 10-GHz Colliding Pulse Mode-Locked Laser" IEEE Photonics Technology Letters, Vol. 18, Issue 4, pp. 625-627, (2006)

29 S. Arahira, S. Kutsuzawa, Y. Ogawa, "Extreme timing jitter reduction of a passively mode-locked laserdiode by optical pulse injection" IEEE Journal of Quantum Electronics, Vol. 35, Issue 12, pp.1805-1811 (1999)

30 C.M. DePriest, T. Yilmaz, P.J. Delfyett, S. Etemad, A. Braun and J. Abeles "Ultralow noise and supermode suppression in an actively mode-locked external-cavity semiconductor diode ring laser" Optics Letters, Vol. 27, Issue 9, pp. 719-721, (2002)

31 J. Lasri, A. Bilenca, G. Eisenstein, and D. Ritter, "Optoelectronic mixing, modulation and injection locking in millimeter wave self-oscillating InP/InGaAs heterojunction bipolar photo-transistors: Single and dual transistor configurations" IEEE Transactions on Microwave Theory Techniques, Vol. 49, Issue: 10, Part 2, pp. 1934–1939, (2001)

32 Y. Barbarin, E.A.J.M Bente, T. de Vries, J.H. den Besten, P.J. van Veldhoven, M.J.H. Sander-Jochem, E.J. Smalbrugge, F.W.M.v. Otten, E.J. Geluk, M.J.R. Heck, X.J.M. Leijtens, J.G.M. van der Tol, F. Karouta, Y.S. Oei, R. Nötzel and M.K. Smit "Butt-Joint Interfaces in InP/InGaAsP waveguides with Very Low Reflectivity and Low Loss" In Proc. IEEE LEOS Benelux Mons, (2005)

33 J.H. den Besten, R.G. Broeke, M. van Geemert, J.J.M. Binsma, F. Heinrichsdorff, T. van Dongen, E.A.J.M. Bente, X.J.M. Leijtens, and M.K. Smit, ``Compact digitally tunable seven-channel ring laser," IEEE Photonics Technology Letters, Vol. 14, Issue 6, pp. 753-755, (2002).

34 C.G.P. Herben, "Compact integrated cross connects for wavelength-division multiplexing networks", PhD Thesis, Delft University of technology, ISBN 90-9014303-3, (2000)

35 P. Dumon, W. Bogaerts, D. Van Thourhout, D. Taillaert, R. Baets, J. Wouters, S. Beckx, and P. Jaenen "Compact wavelength router based on a Silicon-on-insulator arrayed waveguide grating pigtailed to a fiber array" Optics Express, Vol. 14, Issue 2, pp. 664-669, (2006).

36 Michel E. Marhic "Mode-coupling analysis of bending losses in IR metallic waveguides", Applied Optics, Vol. 20, Issue 19, pp. 3436-3441, (1981)

37 M.K. Smit, E.C.M. Pennings, H. Blok "A normalized approach to the design of low-loss optical waveguide bends" Journal of Lightwave Technology, Vol. 11, Issue 11, pp. 1737-1742, (1993).

38 E.C.M. Pennings, R. Van Roijen, M.J.N. van Stralen, P.J de Waard, R.G.M.P. Koumans and B.H. Verbeek "Reflection Properties of Multimode Interference Devices" IEEE Photonic Technology Letters, Vol. 6, Issue 6, pp. 715-718, (1994)

39 R. Hanfoug, L.M. Augustin, Y. Barbarin, J.J.G.M. van der Tol, E.A.J.M. Bente, F. Karouta, D. Rogers, S. Cole, Y.S. Oei, X.J.M. Leijtens, and M.K. Smit "Reduced reflections from multimode interference couplers" Electronics Letters Vol. 42, Issue 8, pp. 465-466, (2006)

40 J. Leuthold, R. Hess, J. Eckner, P. A. Besse, and H. Melchior "Spatial mode filters realized with multimode interference couplers", Optics Letters, Vol. 21, pp 836-838, (1996)

41 K. Yvind, D. Larsson, L.J. Christiansen, C. Angelo, L.K. Oxenlwe, J Mørk, D. Birkedal, J.M. Hvam, J. Hanberg, "Low-jitter and high-power 40-GHz all-active mode-locked lasers" IEEE Photonics Technology Letters, Vol. 16, Issue 4, pp. 975- 977, (2004)

42 Hilmi Demir, Vijit Sabnis, Onur Fidaner, James Harris, Jr., David Miller, and Jun-Fei Zheng "Dual-diode quantum-well modulator for C-band wavelength conversion and broadcasting" Optics Express, Vol. 12, Issue 2, pp. 310-316, (2004)

43 M. Nikoufard, J.H. den Besten, X.J.M. Leijtens, M.K. Smit, "Design and measurement of a reversely biased SOA as high-speed photodetector". In proc. 9th Annual Symp. IEEE/LEOS Benelux Chapter, pp. 71-74, (2004)

44 Mahmoud Nikoufard, "Integrated Wavelength Division Multiplexing receivers" PhD thesis, Eindhoven University of Technology, (2007).

45 Peter Maat, "InP-based Integrated MZI switches for optical communication", PhD thesis, Deft University of Technology, ISBN 90-9014700-4, (2001)

List of acronyms

AAF	Array acceptance factor
ADM	Add-drop multiplexer
AOCR	All optical clock recovery
AOCR-RMLL	All-optical clock recovery ring modelocked laser
AR	Anti reflection
ASE	Amplified spontaneous emission
AWG	Arrayed waveguide grating
CCW	Counter clock wise
CH	Carrier heating
CPM	Colliding pulse modelocked
CW	Clock wise / Continuous Wave
DANL	Displayed average noise level
DQW	Double quantum well
EAM	Electro absorption modulator
ECL	Extended cavity lasers
EC-MLL	Extended cavity modelocked laser
EC-FPMLL	Extended cavity Fabry-Pérot modelocked laser
EDFA	Erbium doped fiber amplifier
FP	Fabry-Pérot
FPMLL	Fabry-Pérot modelocked laser
FPR	Free propagation region
FSR	Free spectral range
FT	Fourier transform
FWHM	Full-width half-maximum
FWM	Four wave mixing
HR	High reflection
HROSA	High resolution optical spectrum analyzer
IR	Infrared
ITU	International telecommunication union
MLL	Modelocked laser
MMI	Multimode interferometer
MOVPE	Metal-organic vapor phase epitaxy
MQW	Multi quantum well
MWL	Multi-wavelength laser

NOLM	Nonlinear optical loop mirror
OCDMA	Optical code division multiple access
OCR	Optical clock recovery
OSA	Optical spectrum analyzer
OTDM	Optical time domain multiplexed
OXC	Optical crossconnect
PD	Photodiode
PECVD	Plasma enhanced chemical vapor deposition
PIC	Photonic integrated circuits
PRBS	Pseudo random binary sequence
QD	Quantum dot
QW	Quantum well
QWI	Quantum well intermixing
RF	Radio frequency
RIE	Reactive ion etching
RMLL	Ring modelocked laser
SA	Saturable absorber
SAG	Selective area growth
SCPM	Self colliding pulse modelocked
SEM	Scanning electron microscopy
SMF	Single mode fiber
SNR	Signal to noise ratio
SOA	Semiconductor amplifier
SPM	Self phase modulation
SSB	Single side band
TE	Transverse electric
TEC	Thermo electric controller
TEM	Transmission electron microscope
TM	Transverse magnetic
TPA	Two photon absorption
UNR	Ultrafast nonlinear refraction
WDM	Wavelength division demultiplexing

Summary

This thesis presents research on, and the realization of compact InP/InGaAsP integrated passively modelocked lasers (MLL) operating in the 1.55 μm wavelength range. The goal of this work was to obtain modelocked laser designs at a repetition rate of several tens of GHz that can be integrated with other devices on a single semiconductor wafer. These modelocked lasers should be usable as optical pulse sources in an all-optical clock recovery application in optical time domain multiplexing (OTDM) systems. The integration of the modelocked laser on a single chip is achieved using the *active-passive integration* technique. This technique allows one to integrate active components such as optical amplifiers and saturable absorbers, with passive components such as waveguides and optical power splitters. The modelocking mechanism of the integrated lasers is passive modelocking using a slow saturable absorber. The saturable absorber is a short optical amplifier section that is reversely biased. The work was largely concentrated on ring laser type cavities. Such a configuration has many advantages. Firstly it allows one to fix the repetition rate of the laser by photolithography. It also provides better performance thanks to the two counter-propagating pulses which collide in the saturable absorber. Finally the output of the laser can be directly interconnected on the same wafer with other devices such as an all-optical switch or a pulse compressor.

From the first realization of integrated ring modelocked lasers (RMLLs) using active-passive integration and a demonstration of a device at 27 GHz, many issues came up and have been addressed in this thesis. First, the understanding of the modelocking mechanism and other dynamics needed to be better understood. To address this issue, a simulation tool of RMLL was developed. Simulation results showed that symmetrical cavities show a much wider operating range for stable modelocking. The transitions from a modelocked state of the laser to another operating regime have been explored with the model. The simulation tool requires parameters describing the gain properties of the material. These have been accurately measured using a new type of high resolution spectrum analyzer.

Another important issue which came out from the first RMLL realization was the necessity to reduce all the reflections inside the modelocked laser cavity and in particular the reflections at the active-passive interfaces. Special efforts have therefore been made to characterize the optical losses and reflections at those interfaces and to minimize them to a sufficiently low value of less than -50 dB.

To validate techniques of fabrication and materials required to achieve high repetition rate RMLL designs, the realization of more compact devices through the use of deep etching has been investigated in this thesis. Results are presented on, at that time, the world's most compact AWG using a double-etch technique, and the world's first InAs/InP quantum dot (QD) lasers employing narrow deeply etched ridge active waveguides in the 1.55 μm wavelength region.

Before realizing a final RMLL design on an active-passive wafer, a series of all-active devices has been designed, fabricated and characterized. These all-active chips provided material for the gain measurements and allowed to look further into short pulse laser characterization techniques and to test designs for reducing reflections from other intra-cavity components. The results of the all-active MLLs have been obtained in different configurations. Firstly, 20 GHz and 40 GHz linear all active Fabry-Pérot MLL (FPMLL) lasers have been successfully fabricated. Modelocking has been achieved with these lasers in the colliding pulse modelocked (CPM) and self CPM configurations. Pulse lengths down to 1.6 ps (at 20 GHz) have been observed. A 40 GHz repetition rate was demonstrated in a CPM laser with a Saturable Absorber (SA) positioned in the center of the FP cavity. All-active 15 GHz RMLLs have also been successfully fabricated. These lasers show a relatively good timing stability due to the ring configuration. Measured output pulses are highly chirped and an FWHM bandwidth of up to 4.5 nm was obtained. Such lasers with high bandwidth pulses and compatible with active-passive integration are of great interest for optical code division multiple access applications, where information is coded in the spectrum. Finally, first results from MLLs realized on an active-passive wafer are presented. Passive modelocking has been demonstrated in these integrated Extended Cavity FPMLLs with minimized intra-cavity reflections. Pulses of 2.1 ps duration and with a small pedestal have been observed. The pulses are close to transform-limited. The longer timescale dynamics of the EC-FPMLLs are reduced compared to the all-active FPMLLs, which is understood to be due to the short amplifier section.

The use of a MLL at 20 GHz for the all optical clock recovery (AOCR) application and a special RMLL design for AOCR at 40 GHz are presented in the last chapter of this thesis. Many characteristics of the AOCR at 20 GHz could be quantified. The design of the 40 GHz RMLL laser is for an active-passive wafer. The design utilizes all the minimizations of small intra-cavity reflections. For the AOCR application a novel way to couple the optical input signal into the MLL via a separate waveguide is presented. Based on the accumulated results presented in this thesis the timing jitter of the clock recovered from this laser is expected to be sufficiently low to comply with the telecom requirements at 40 GHz.

List of publications

Journals

1. Y. Barbarin, X.J.M. Leijtens, E.A.J.M. Bente, C.M. Louzao, J. Kooiman, M.K. Smit. "Extremely small AWG demultiplexer fabricated on InP by using a double-etch process" IEEE Photonics Technology Letters, Vol. 16, issue 11, pp. 2478-2480, (2004)
2. Y. Barbarin, E.A.J.M Bente, M.J.R. Heck, J.H. den Besten, G. Guidi, Y.S Oei, J.J.M. Binsma and M.K. Smit "Realization and Modeling of a 27 GHz Integrated Passively Modelocked Ring Laser" IEEE Photonics Technology Letters. Vol 17, issue 11, pp. 2277-2279, (2005)
3. Y. Barbarin, E.A.J.M. Bente, C. Marquet, E.J.S Leclère, J.J.M. Binsma and M.K. Smit. "Measurement of Reflectivity of Butt-Joint Active-Passive Interfaces in Integrated Extended Cavity Lasers" IEEE Photonics Technology Letters. pp. 2265-2267, Vol. 17, issue 11, (2005)
4. Y. Barbarin, E.A.J.M Bente, L. Mussard, G. Servanton, Y.S. Oei, R. Nötzel and M.K. Smit "Gain Measurements of Fabry-Pérot InP/InGaAsP Lasers using an Ultra High Resolution Spectrometer" Applied Optics, Vol. 45, Issue 35, pp. 9007-9012, (2006)
5. Y. Barbarin, E.A.J.M Bente, M.J.R. Heck, Y.S. Oei, R. Nötzel and M.K. Smit "Characterization of a 15 GHz Integrated Bulk InGaAsP Passively Modelocked Ring Laser at 1.53μm" Optics Express, Vol. 14, Issue 21, pp. 9716-9727, (2006)
6. Y. Barbarin, S. Anantathanasarn, E.A.J.M. Bente, Y.S. Oei, M.K. Smit and R. Nötzel "1.55 μm Range InAs/InP Quantum Dot Fabry-Pérot and Ring Lasers using Narrow Deeply Etched Ridge Waveguides" IEEE Photonics Technology Letters, Vol. 18, Issue 24, pp. 2644-2646, (2006)

International Conferences

7. Y. Barbarin, E.A.J.M. Bente, M.J.R. Heck, Y.S. Oei, R. Nötzel and M.K. Smit "Passively Modelocked 20 and 40GHz Bulk InGaAsP Lasers" 31st European

Conference on Optical Communication, Glasgow, Scotland, Vol. 3, pp. 673-674, (2005)
8. Y. Barbarin, X.J.M. Leijtens, E.A.J.M. Bente, C.M. Louzao, J. Kooiman, M.K. Smit. "Extremely small AWG demultiplexer fabricated on InP by using a double-etch process" In proceedings IPR 2004, 30 June - 4 July 2004, San Francisco, USA, IThG4, (2004)
9. Y. Barbarin, E.A.J.M Bente, M.J.R. Heck, J.H. den Besten, G. Guidi, J.J.M. Binsma and M.K. Smit "Integrated passively modelocked InGaAsP ringlasers with active-passive integration" In proceedings IPR 2004, San Francisco, USA, IWC2. (2004).
10. Y. Barbarin, J.J.M. Binsma, E.A.J.M. Bente, C. Marquet, E.Leclere, T. De Vries, P.J. van Veldhoven, Y.S. Oei, R. Nötzel, M.K. Smit, "Butt-joint reflectivity and loss in InGaAsP/InP waveguides" In proceedings ECIO '05, 6-8 April 2005, Grenoble, France, pp. 406-409, (2005)
11. Y. Barbarin, E.A.J.M Bente, M.J.R. Heck, Y.S. Oei, R. Nötzel, D. Lenstra, M.K. Smit, "Detailed Characterization of a 15GHz Integrated Bulk InGaAsP Passively Modelocked Ring Laser" In Proc. EOS Topical Meeting on Extreme Optics, Paris, France, pp. 75-76, (2006)

Co-author in journals and international conferences

12. M. Yousefi, Y. Barbarin, S. Beri, E. A. Bente, M. K. Smit, R. Nötzel and D. Lenstra, "New role for nonlinear dynamics and chaos in integrated semiconductor laser technology" Physical Review Letters, Vol.98, 044101, (2007)
13. E.A.J.M Bente, Y. Barbarin, J.H. den Besten; S.K. Smit, J.J.M. Binsma "Wavelength selection in an integrated multi-wavelengh ring laser." IEEE Journal of Quantum Electronics, 40, issue 9, pp. 1208-1216, (2004)
14. M.J.R. Heck, E.A.J.M Bente, Y. Barbarin, D. Lenstra and M.K. Smit "Simulation and Design of Integrated Femtosecond Passively Mode-locked Semiconductor Ring Lasers Including Integrated Passive Pulse Shaping Components" IEEE Journal of Selected Topics in Quantum Electronics, Vol. 12, No. 2, pp 265-276, (2006)
15. E.A.J.M. Bente, Y. Barbarin, J.H. den Besten, M.K. Smit, "Characterisation and modelling of a compact multiwavelength ringlaser" Proc. ECIO'03. ISBN 80-01-02729-5, Prague, Czech Republic, pp. 155-158. (2003)
16. S. Anantathanasarn, R. Nötzel, P.J. van Veldhoven, F.W.M. van Otten, Y. Barbarin, G. Servanton, T. de Vries, E. Smalbrugge, E.J. Geluk, T.J. Eijkemans, E.A.J.M. Bente, Y.S. Oei, M.K. Smit and J.H. Wolter, "Lasing of wavelength-tunable (1.55-μm region) InAs/InGaAsP/InP (100) quantum dots grown by metalorganic vapor phase epitaxy", Applied Physics Letters, 89, 073115 (2006)
17. R. Hanfoug, L.M. Augustin, Y. Barbarin, J.J.G.M. van der Tol, E.A.J.M. Bente, F. Karouta, D. Rogers, S. Cole, Y.S. Oei, X.J.M. Leijtens, and M.K. Smit "Reduced reflections from multimode interference couplers" Electronics Letters Volume 42, Issue 8, p. 465-466, (2006)

18. L. Babaud, M.K. Smit, F.H. Groen, X.J.M. Leijtens, M. Bertogna, J.H. den Besten, Y. Barbarin, Y.S. Oei, F. Karouta, J.J.M. Binsma, "First integrated continuously tunable AWG-based laser using electro-optical phase shifters" In proceedings ECIO '05, 6-8 April, (2005)
19. P. Munoz, M. Heck, E.A.J.M. Bente, Y. Barbarin, M.K. Smit, D. Pastor, J. Capmany, "Design of short pulse compressors based on arrayed waveguide gratings and phase modulators." In proceedings Optoel '05, 13-15 July 2005, Elche, Alicante, Spain, pp. 253-258, (2005)
20. S. Anantathanasarn, R. Nötzel, P.J. van Veldhoven, F.W.M. van Otten, Y. Barbarin, G. Servanton, T. de Vries, E. Smalbrugge, E.J. Geluk, T.J. Eijkemans, E.A.J.M. Bente, Y.S. Oei, M.K. Smit, J.H. Wolter "Wavelength Controlled InAs/InP Quantum Dots for Telecom Laser Applications" In proceedings 6th ESPS-NIS, Nottingham UK, (2006)
21. M. Yousefi, Y. Barbarin, S. Beri, E. Bente, D. Lenstra, M. K. Smit, "Observation of nonlinear dynamics and chaos in InGaAsP/InP based integrated semiconductor lasers" In proceedings SPIE Photonics Europe 2006, Strasbourg France. (2006)

LEOS Benelux and ESWL

22. Y. Barbarin, E.A.J.M Bente, T. de Vries, J.H. den Besten, P.J. van Veldhoven, M.J.H. Sander-Jochem, E.J. Smalbrugge, F.W.M.v. Otten, E.J. Geluk, M.J.R. Heck, X.J.M. Leijtens, J.G.M. van der Tol, F. Karouta, Y.S. Oei, R. Nötzel and M.K. Smit "Butt-Joint Interfaces in InP/InGaAsP waveguides with Very Low Reflectivity and Low Loss" proc. IEEE/LEOS Benelux Chapter, ISBN 2-960022645, Mons, Belgium, pp. 249-252. (2005)
23. Y. Barbarin, X.J.M Leijtens, E.A.J.M. Bente, J. Kooiman, M.K. Smit "Extremely small AWG demultiplexer fabricated on InP by using a double-etch process." Proc. IEEE/LEOS Benelux Annual Symposium, Enschede, pp. 61-64, (2003)
24. Y. Barbarin, E.A.J.M. Bente, M. Heck, D. Lenstra, M.K. Smit, "Simulation of injection seeding of an integrated passively modelocked ring laser" proc. IEEE/LEOS Benelux Annual Symposium, Enschede, pp. 101-104., (2003)
25. Y. Barbarin, E.A.J.M. Bente, M. Heck, D. Lenstra, M.K. Smit "Modelling of an integrated passively modelocked ring laser for clock recovery" proc. European Semiconductor Laser Workshop, Turino, Italy, 19-20 September, (2003)
26. Y. Barbarin, E.A.J.M. Bente, C. Marquet, E.J.S Leclère, J.J.M. Binsma and M.K. Smit. "Measurements of reflectivities on butt-joint active-passive interfaces in extended cavity Fabry Perot lasers" IEEE/LEOS Benelux Chapter, 2-3 December 2004; IEEE, Ghent, pp. 119-122, (2004)
27. Y. Barbarin, E.A.J.M Bente, M.J.R. Heck, D. Lenstra, J.H. den Besten, J.J.M. Binsma and M.K. Smit Modelling and experimental results of a 26Ghx integrated passively modelocked ring laser. "IEEE/LEOS Benelux Chapter, IEEE, Ghent, pp. 13-16, (2004)
28. Y. Barbarin, E.A.J.M Bente, L. Mussard, G. Servanton, Y.S. Oei, R. Nötzel and M.K. Smit "Gain measurements of Fabry-Perot InP/InGaAsP lasers using an

ultra high resolution spectrometer." proc. IEEE/LEOS Benelux Chapter, ISBN 2-960022645, Mons, Belgium, pp. 253-256, (2005), (2005)
29. Y. Barbarin, E.A.J.M Bente, M.J.R. Heck, Y.S. Oei, R. Nötzel and M.K. Smit "Passively modelocked 15, 20 and 40 Ghz bulk InGaAsP lasers" proc. IEEE/LEOS Benelux Chapter, ISBN 2-960022645, Mons, Belgium, pp. 249-252, (2005)
30. Y. Barbarin, S. Anantathanasarn, E.A.J.M. Bente, Y.S. Oei, M.K. Smit and R. Nötzel "1.55 μm Range InAs/InP Quantum Dot Fabry-Pérot and Ring Lasers using Narrow Deeply Etched Ridge Waveguides" proc. IEEE/LEOS Benelux Chapter, ISBN , Eindhoven, Netherlands, pp. 249-252, (2006)

Acknowledgements

Writing this section is a real pleasure, it means that a lot has been accomplished and I would like to thank everyone who has contributed to this small book directly and indirectly.

First of all, I am very grateful to my direct supervisor Erwin Bente. Dear Erwin, we did it! I knew after my project of end of study that starting a PhD with you will be great. I must say that I have not been disappointed. Working with you has been very easy and very valuable. I think that we have few approaches which are similar and if not, they are somehow complementary. During these four years, I couldn't always catch your little jokes, as much as you couldn't always understand my French way of talking English but we managed well. To summarize: Merci pour tout !

Then, I would like to thank Meint Smit who offered me the opportunity to come in his group for my project of end of study and later on to start a PhD. Meint, thanks you very much for the famous small PHASAR, you gave me the chance to fabricate it. I would also like also to thank you for your constructive comments during my PhD and particularly in the writing of papers. I am just a bit sorry to be your second PhD leaving Eindhoven (or Delft) without speaking properly Dutch.

I'm also very grateful to Jan Hendrik den Besten and Martijn Heck for sharing more than an office during my PhD. Jan Hendrik, you were finishing your PhD when I started mine and I could benefit of your experience. Thanks a lot ! I wish the great dancer of the *Orangerie* a great career in business and administration. Martijn, we started almost at the same time. We are quite different in general (not only from a music point of view :-) but our differences allowed us to exchange a lot of ideas and advices for each others projects and I am very pleased by the results. I wish you a lot of success with the end of your busy PhD and even more after it !

This thesis is about laser chips which have been realized in the COBRA cleanroom. If you read at least Chapter 3, you will see that it is a long story which has been possible thanks to a very large number of people. I would like first to thank Tjibbe and Soufian who have trained me the first 6 months. I guess you did well your job, because that year, I've fabricated two working chips! For the second chip, I would like to thank Hans Binsma for the precious active-passive wafer and for keeping open JDSU facilities as long

as possible. Then, I have to thank all the technicians working in the cleanroom, because without you, simply no chips… Tjibbe, your relax behavior in a cleanroom is remarkable (thanks also for the visit of Den Bosch at night). Erik Jan, I didn't learn the SEM, sorry that you had to make most of the pictures. Kitty, I'm still wondering if the primer oven has started, are you sure? Ben, I don't remember the installation of all the cleanroom equipments, but I do remember that we should go every month to a place called Walhalla. Beste Barry, I am still sorry that I have always asked you to cleave my quarters in more than 10 pieces with so high accuracy :-) Good luck with the next hundred text songs ! New processes… active passive integration, self aligned metallization, deep-shallow etching, etc… Not easy, but with some determination it works ! Thanks a lot to Siang and Fouad. Fouad, bonne chance pour la suite, j'ai beaucoup apprécié de pouvoir communiquer dans ma langue maternelle même si dans la confusion, il t'arrivait de me parler en néerlandais… Processing was one thing, but it starts with wafers! I would like to thank very much Richard Nötzel, René van Veldhoven and Sanguan Anantathanasarn for the wafers grown in our cleanroom. Furthermore, I am glad that we could obtain nice results with the deep Quantum Dots. Good luck for the next chips!

Open your mind to chaos. That's what I've learned from Mirvais Yousefi. Mirvais, if you didn't have a look at some of my data, we will have missed a very nice PRL paper. You know that "dynamic" is now part of my vocabulary ! Thanks also for the great time we had at few conferences. Mentioning this work, I would like of course to thank Daan Lenstra and Stefano Beri who have largely contributed to these results. Daan, thanks a lot as well for your inputs at the initial development of the RMLL model.

My project was linked with the one of Erwin Verdurmen at ECO. I am very happy that we could obtain the results described in Chapter 6. I would like to thank, Erwin V (good luck with your career!), his coach Huug de Waardt and all the members of ECO that I met during measurements at the 12th floor and during ECOC evenings. I would like to thank also the members of the user committee for their interesting feedbacks on the project.

Outside the TU Eindhoven, I would like to thank Kresten Yvind from COM (Denmark) for his useful discussion and advices at the beginning of my PhD. I'm also very grateful to José Pozo and Judy Rorison from Bristol University for the realization of SA using their FIB. Muchas Gracias José por el bueno tiempo a Bristol y a Heraklion.

For this paragraph, I can switch to French. Indeed most of the graduation students I had were French. Their work is included in this thesis and I would like to thank them very much for their inputs. Edith et Christel, inséparables, merci beaucoup pour votre travail sur les réflexions internes des cavités lasers. Laurène 2ème du prénom, chapeau ! En seulement trois mois, tu as fait ce programme Matlab pour le gain. Germain dit petit scarabée, seul mec de la série, merci beaucoup pour ton travail sur le gain. Bonne continuation avec ton *master* à Grenoble. Carmen, la Galicienne de Saint-Jacques de Compostelle, très francophile, non ? Désolé pour les aspects que tu qualifiais de « complicado » et merci beaucoup pour ton travail sur les AWGs. I would like to thank as well Giacomo Guidi and Jeroen Kooiman for the masks set that they have designed during their master thesis and that I have used.

More generally I would like to thank all the other members of the OED group who have somehow contributed to this works. Xaveer, thanks you very much for your good

advices during the conception of the masks, the work on the small AWG, and of course for Park Pop, Muse and "*it is not because you are*". Hans, like Tjibbe in front of a broken chip in the cleanroom, you're perfectly relax when a Microsoft machine crashes. Thanks a lot for taking care of all those small important details. Els, Susan, I think that we forgot you too often. Thanks you very much for taking care of the *secretariaat* and a bit more. Els, you really took care that I "land" softly in the Netherlands. Génia and Michiel, I would like to thank you for your friendship and your kind hospitality during the first month of my PhD. Jos, I'm glad you could find other chess players during those four years. In the wrong order, I would like to thank, Antia, Francesca, Luc, Homar, Uzma, Ling, Mahmoud, Fabiola, Pascual, Boudewijn, Ronald, Christophe, Dario, Cosimo, Mark & Bart, Roger, Reig, Raquel, Jorge, Aert, Milan, Bauke, Geri, Martin, Youcai, Hugo, Fokke, Thieu for their friendship at work and outside the university. Els, Rabah and Francisco, 3500 Km in 5 days through California, Nevada and Arizona, that was something ! I'll complete the list with the extended "Little Italy" of the 10th floor. I'd like to thank Pietro, Stefano, Guido, Roberto, Maria, Alessandro, Zermain, Antonio, Materazzi, Analisa, Marco, Johan, Olivier, the Poorman and Tanya for the huge number of pasta diner that we had with wine tasting.

When you live abroad, you have the tendency to work quite a lot, especially to get a PhD title. Therefore, you have to counter-balance your working life with other events. People often talk of *Yin and Yang* and I must say that I have followed this precept. For that reason, I have to thank all the persons who have contributed to my equilibrium. In a chronological order, I would like to thank my *Santiago de Cuba girlfriends*: Paola, Talia and Iciar, perdone si no bailo salsa. At the same time I met: Issam et ses supers tajines, Petr from Plzen who becomes Petra at Karnaval, Bertrand le camerounais d'adoption and Alberto who speak Québécois with hands and a strong Italian accent. I'd like to thank the *international Philips birthday party team* and especially Erik-Jan, Igor and Julian. Let's makes party better ! I'd like to thank my two housemates: el Chico, who loves Saint-Néctaire and who is the king of the chili con carne, y por supuesto Anabel who claims that the real paella (originally from V*B*alencia be careful!) does not contain seafood. Anabel we prefer it with seafood ! The list of acknowledgements continues with the *diner + DVD night members* : Olavio, Vincent, Elodie, Andres, Marie, Gokan, Séverinne, Martin, met Ton, Jean Guy, Ana, Daniel and Carmencita. An advice: next times, don't visit a fort before the movie! Of course, I cannot forget the Sint Antoniusstraat family : Tamy responsible of it, dr. Srdjan with memory problems, Francesca, Przemek, la Natalia and the Martin, Laurène 1ère du prénom, Fabiola, Alberto, Anka, Hugo, Amandine, Fabien, Paolo and Vesna. So good parties, none of us will ever forget the different X-mas diners ! I have to mention that sport was also part of my equilibrium, thus I would like to thank my squash partners: Olavio, Hector, Carlos Mex, Carlos PT, Oujardin, Ivo (very sorry for your nose) and Marie-Claire who was the most difficult to beat. Je voudrais enfin saluer les vieux amis de la famille qui sont venus me rendre visite à Eindhoven même en plein hiver avec 30 cm de neige sur la route : Gaëtan, Manu, Nico, Cédric T, Pauline, Gwen, gd Manu, Séb, Leod&Claire, Christophe et Yann.

Maman, papa, votre fils devient toubib ! Notre famille équilibrée est vraiment une chance et une force. Sans vos valeurs justes, que vous nous avez inculquées naturellement à Gaëtan, Mickaël, moi, et les autres, nos destins auraient sûrement étés bien différents. Merci !

Curriculum vitae

Yohan Barbarin was born in Clermont-Ferrand, France, in 1978. He received in 2002 the M.Sc. degree from the Marseille National Higher School in Physics and Engineering (ENSPM), nowadays integrated in the "Ecole Centrale de Marseille" (France). During his master degree, he has been working during internships for ST microlelectronics (Rousset, France) and for the Laser MegaJoule (LMJ) project at Sagem SA (France). His final project has been carried out at the COBRA Research Institute at Eindhoven University of Technology, (The Netherlands). At the same institute, from 2002 to 2006, Yohan Barbarin has been working toward the Ph.D. degree, with research concerning the development of integrated mode-locked semiconductor laser sources for 160–640 Gbit/s optical time-domain multiplexed (OTDM) applications. He is currently working as a researcher at the Eidgenössische Technische Hochschule (ETH) in Zürich, Switzerland on electrically pumped modelocked vertical extended cavity semiconductor lasers (VECSELs).